ELECTROMAGNETIC FLOW CONTROL: A REVIEW AND EXPERIMENTAL DEVELOPMENT AND TESTING OF A COMPACT ACTUATOR

by

ERIC M. BRAUN

Presented to the Faculty of the Graduate School of
The University of Texas at Arlington in Partial Fulfillment
of the Requirements
for the Degree of

MASTER OF SCIENCE IN AEROSPACE ENGINEERING

THE UNIVERSITY OF TEXAS AT ARLINGTON
November 2008

In memory of my mother.

ACKNOWLEDGEMENTS

First and foremost, I would like to thank my mother, Marcia Lee, for all of her support of my education. Unfortunately, she passed away suddenly while recovering from inflammatory breast cancer (IBC) treatment shortly before I was able to complete this thesis. Finances were always difficult as she raised me and my sister, Lisa, but she sacrificed a great deal and somehow managed to assist in paying for our education including graduate school.

I wanted to attend graduate school at a university that would give me the ability to pursue various research interests and projects. In light of that statement, I am very grateful to the three professors I have worked for while at the UT Arlington Aerodynamics Research Center. Dr. Frank Lu and Dr. Don Wilson have been tremendously supportive since the day I arrived. I believe their research advice and graduate level courses have instilled just as much knowledge in me as I could receive at any highly ranked university. Dr. Craig Dutton, despite moving on to the University of Illinois at Urbana-Champaign in 2007, has continued to assist me with my research project. I am also thankful to Dr. Kamesh Subbarao for serving as a committee member for this thesis. I additionally wish to thank Dr. Ramakanth Munipalli of HyPerComp, Inc., for providing a computational MHD code that has been used for the EMFC electric field calculations presented in this paper. This work was partially supported by the Texas Advanced Research Program, Project No. 003656-0013-2006.

Since 2006, I am glad to have worked with fellow researchers Richard Mitchell, Adam Pierce, and Akihiro Nozawa as well as Rod Duke, our scientific apparatus engineering technician, on rebuilding the low-speed and supersonic wind tunnels at

the ARC. Between these large efforts and many smaller ones, I think we have been able to considerably improve the ARC for future research efforts. Additionally, they have all assisted me at some point with the research presented in this thesis. I have enjoyed working on a collaborative research project with Professor Yung-Hwan Byun and Hui Jeong from Konkuk University. I have also had the privilege of a great working environment at the ARC with an ever-increasing amount of people, notably including Rafaela Bellini, Albert Ortiz, Dr. Philip Panicker, and Prashaanth Ravindran, all of whom I have known for over two years now along with those mentioned in the beginning of this paragraph.

November 25, 2008

ABSTRACT

ELECTROMAGNETIC FLOW CONTROL: A REVIEW AND EXPERIMENTAL DEVELOPMENT AND TESTING OF A COMPACT ACTUATOR

ERIC M. BRAUN, M.S.

The University of Texas at Arlington, 2008

Co-Supervising Professors: Frank K. Lu and Donald R. Wilson

This thesis is divided into two sections which both relate to the field of magnetohydrodynamics and particularly electromagnetic flow control (EMFC). The first section contains a review of recent research in EMFC. The second section presents the experimental results of a compact EMFC actuator designed for use at low speeds where the flow conductivity is raised by conductive seed particle injection.

Fifty years ago, publications began to discuss the possibilities of using EMFC to improve aerodynamic performance. This led to an era of research that focused on coupling the fundamentals of magnetohydrodynamics (MHD) with propulsion, control, and power generation systems. Unfortunately, very few designs made it past an experimental phase as, among other issues, power consumption was unreasonably high. Recent proposed advancements in technology like the MARIAH hypersonic wind tunnel and the AJAX scramjet engine have led to a new phase of MHD research in the aerospace industry, with many interdisciplinary applications. Aside from propulsion systems and channel flow accelerators, electromagnetic flow control concepts applied to control surface aerodynamics have not seen the same level of advancement that may eventually produce a device that can be integrated with an aircraft or missile. Therefore, the purpose of this thesis is to review the overall feasibility of the different electric and electromagnetic flow control concepts. Emphasis is placed on EMFC and experimental work.

The second section describes the development and testing of a facility for electromagnetic boundary layer flow control employing conductive particle seeding. It was designed and constructed to perform basic research in EMFC and address some of the issues discussed in the review. The facility consists of three integrated components: a conductive particle seeding system, an ionization actuator, and a Lorentz force actuator. The Lorentz force actuator was designed in particular to be compact, employing a row of flush-mounted surface electrodes alternated with embedded Nd-FeB magnets perpendicular to the flow direction. Experiments were performed in a low-speed wind tunnel with atmospheric pressure. Low ionization energy potassium carbonate particles were meant to be seeded into the airflow to then be ionized by a high voltage field before passing over the active EMFC actuator. Although a high voltage field can ionize air and create a glow discharge, the potassium carbonate seed is largely unaffected. It appears that the potassium carbonate seed must be broken down thermally or with a high voltage, high current pulse that contains energy at the level needed to vaporize the potassium carbonate molecules. Different forms of seeding were attempted but were largely unsuccessful. A glow discharge was established over the EMFC actuator, but PIV imaging indicates that the boundary layer effects produced in this case were largely a result of Joule heating and not the Lorentz force. In the conclusion, several recommendations are laid forth pertaining to the future of EMFC experimentation with compact actuators and conductive particle seeding.

TABLE OF CONTENTS

Chapter

Appendix

LIST OF FIGURES

LIST OF TABLES

NOMENCLATURE

b	induced magnetic field, T
B	magnetic field, T
c_f	skin friction coefficient
DBD	dielectric barrier discharge
E	electric field, V/m
e	electron charge, -1.602×10^{-19} C
EFC	electric flow control
$EMFC$	electromagnetic flow control
F	force, N
F_L	Lorentz force, N (single particle), N/m^3 (ionized particles per unit volume)
h	enthalpy, kJ/(kg·K)
I	current, A
I_{BL}	$\sigma B^2 L/\rho u (c_f/2)^{1/2}$, boundary layer magnetic interaction parameter
I_{EM}	$BE\sigma L/\rho u^2$, electromagnetic interaction parameter
I_M	$\sigma B^2 L/\rho u$, magnetic interaction parameter
J	current field, A/m^2
$\widetilde{J}$	drift current density, A/m^2
L	characteristic length, m
$\widetilde{M}$	magnetization, A/m
MHD	magnetohydrodynamics
n	number density, 1/m^3
p	static pressure, Pa

$\hat{p}$	stress tensor
$\widetilde{P}$	polarization vector
q	electric charge, C
Re	$\rho u L/\mu$, Reynolds number
Re_M	$\mu_0 \sigma u L$, magnetic Reynolds number
r	distance, m
S	cross sectional area, m^2
t	time, s
T	temperature, K
u	flow speed, m/s
$\widetilde{U}$	drift velocity, m/s
V	voltage, V
WIG	weakly ionized gas
x	Cartesian coordinate along streamwise length
y	Cartesian coordinate along spanwise width
z	Cartesian coordinate along transverse height
Z	net charge on a given particle, C
β	Hall parameter
δ	boundary layer thickness
ϵ	energy, J/kg
ε_0	permittivity of vacuum constant, 8.854×10^{-12} F/m
κ	thermal conductivity, W/m·K
μ	viscosity, kg/m·s
μ_0	permeability of vacuum constant, 1.257×10^{-6} $\mathrm{N/A^2}$
ρ	density, $\mathrm{kg/m^3}$

ρ_e	charge density, C/m^3
σ	conductivity, ℧/m
ψ	viscous force vector
ω	circular frequency
$D[\ ]/Dt$	total derivative
∇	grad

Subscripts

BL	boundary layer
i, j, k	orthogonal unit vectors
p	particle
S	species
∞	free stream

CHAPTER 1

INTRODUCTION

1.1 Introduction

The term *magnetohydrodynamics* (MHD) stands for a field of study concerned with applying the principles of electromagnetism to fluid mechanics. The fluid, which this term implies to be water, is extended to all liquids and gases. Additionally, the fluid must be electrically conductive in order for there to be any interaction with electromagnetic fields. Magnetohydrodynamics was originally developed to describe several phenomena surrounding the behavior of plasma around the Earth and in space (e.g., aurora borealis, interstellar medium dynamics). Eventually, research into plasmas and electromagnetic fields grew and formed a variety of multidisciplinary engineering applications. Plasma has been used in an increasing number of industrial applications, with the most notable new product being plasma displays for flat panel televisions. The knowledge of magnetohydrodynamics has produced advances in utilizing plasma, alternative power generation, weaponry, and propulsion.

Liquid metals, because of their high conductivity (although it does drop with an increase in temperature), have a variety of MHD applications including the cooling of nuclear reactors. Fluids and gases, unless at very low pressures or high temperatures, do not have high conductivity which leads to few feasible engineering applications. The conductivity of gases is often so low that they are better defined as insulators. In order for pure gases to conduct, they must be heated until ionization occurs, releasing electrons which are no longer associated with an atom or molecule. This is essentially the definition of plasma—an ionized, yet electrically neutral gas-like state of matter composed of free electrons and radicals that make the matter conductive and therefore responsive to electromagnetic fields. The vast majority of the universe exists in the plasma state of matter.

Turning specifically to the concept of MHD propulsion, which has existed for over half a century, there are three major engine designs which have developed. First are electrostatic engines, of which a minuscule amount of thrust is obtained mainly through utilizing the Coulomb force. These engines operate with low power and provide a match with radioisotope thermoelectric generators currently used in space. Although the thrust is small, years of continuous operation is feasible for obtaining the high speed needed for flight throughout the solar system. The second concept, electrothermal engines (or arcjet rockets), uses electromagnetic actuators to generate and heat a plasma propellant before exhausting it through a nozzle. These hybrid engines are small and can actuate quickly, making them ideal for rapid orbital corrections. The last concept consists of purely electromagnetic engines, which upgrade from the Coulomb force to the Lorentz force and accelerate plasma through an applied electromagnetic field. Engines that use the Lorentz force are theoretically capable of generating a high specific impulse and thrust comparable to current air-breathing and rocket engines.

Most of the early electromagnetic engine concepts relied on supplying plasma to the engine core where it was accelerated by the Lorentz body force generated with a series of segmented electrodes and magnets. Research in these engines was a popular field in the 1960's because of the high specific impulse compared to chemical rocket propulsion, which was already a mature technology at the time. While the specific impulse of a chemical rocket reaches about 450 seconds, the specific impulse of an electromagnetic engine can reach over 10,000 seconds. Unfortunately, pure electromagnetic propulsion is plagued by extreme power requirements. The thrust from one of these engines is insufficient for reaching orbital velocity considering the large mass and volume of the required on-board power supply.

Another potential aerodynamic application of MHD that has recently become popular is electromagnetic flow control (EMFC). The concept of EMFC also uses the Lorentz force, but EMFC systems may be used instead for conventional control surface replacement. EMFC actuators on a supersonic or hypersonic aircraft may be advantageous when compared to traditional control surfaces. Their benefits include rapid actuation and minimal obstruction to the flow. Among the drawbacks is again the need for a conductive flow and the possibility that the power requirement is still not practical. To minimize the power requirement, thermal ionization methods have been replaced by so-called low-temperature plasma generation systems. Ionization by applying a high voltage electric field has been extensively researched, along with other methods including laser beam, microwave, and radiation sources.

1.2 Fundamental MHD Theory for Aerodynamics

The fundamental equations of magnetohydrodynamics combine electromagnetic relations with the equations of fluid dynamics. This combination results in rather complex derivations and equations. Sutton and Sherman [12] provide a theory that begins with a continuum control volume analysis that splits up surface and body forces, summarized below while considering the characteristics of EMFC. The conservation of mass equation remains typical for fluid mechanics as electromagnetic fields do not add mass into a system, namely,

$$\frac{\partial \rho}{\partial t} + \nabla \cdot \rho \mathbf{u} = 0. \tag{1.1}$$

The conservation of momentum equation is shown next where $p_{i,j}$ is the stress tensor that is then split into normal and shear components.

$$\rho \frac{Du_i}{Dt} = -\sum_j \frac{\partial \hat{p_{i,j}}}{\partial x_j} + F_i \tag{1.2}$$

The conservation of energy relationship can be written as

$$\frac{1}{2}\rho\frac{Du^2}{Dt} - \rho\frac{D\epsilon}{Dt} = \mathbf{E}\cdot\mathbf{J} + \nabla\cdot(\kappa\nabla T) - \sum_S \nabla\cdot\left(\widetilde{\mathbf{U}}_S\rho_S h_S\right) - \sum_{i,j}\frac{\partial}{\partial x_j}\left(u_i\hat{p_{i,j}}\right) \tag{1.3}$$

Here, the LHS represents the increase in energy. On the RHS, the first term stands for the rate at which electromagnetic energy enters into or leaves the control volume. The next two terms account for the energy entering the control volume through conduction and diffusion. The subscript S stands for each particular species. The last term accounts for the work done by surface forces.

The above equations are then combined with Maxwell's equations, which as a set are very difficult to solve. These equations are as follows:

$$\nabla\times\mathbf{E} = -\frac{\partial\mathbf{B}}{\partial t} \tag{1.4a}$$

$$\nabla\cdot\mathbf{B} = 0 \tag{1.4b}$$

$$\nabla\cdot\mathbf{E} = \frac{\rho_e}{\varepsilon_0} \tag{1.4c}$$

$$\nabla\times\mathbf{B} = \mu_0\mathbf{J} \tag{1.4d}$$

Equation (1.4a), the Maxwell–Faraday equation, states that the electromotive force is equal to the change in magnetic flux in a closed circuit. Equation (1.4b), Gauss' law for magnetism, shows that the divergence of a magnetic field is zero. Gauss' law, which relates charge distribution to the electric field created, is shown in Eq. (1.4c). Finally, Ampere's law in Eq. (1.4d) relates the magnetic field and electric current in a closed loop. For EMFC with a weakly ionized gas ($\sigma \leq 100$ ℧/m), approximations can be made so that the MHD equations appear more straightforward. The first approximation involves the displacement current in Ampere's law, which appears below as the last term on the LHS:

$$\nabla \times \mathbf{B} = \mu_0 \left(\widetilde{\mathbf{J}} + \frac{\partial \widetilde{\mathbf{P}}}{\partial t} + \nabla \times \widetilde{\mathbf{M}} + \varepsilon_0 \frac{\partial \mathbf{E}}{\partial t} \right) \tag{1.5}$$

This term can be compared with the conduction current

$$\mathbf{J} = \sigma \mathbf{E} \tag{1.6}$$

using a ratio of amplitudes and a permittivity constant on the order of 10^{-11} F/m (approximating a vacuum),

$$\left\| \frac{\varepsilon_0 \left(\partial \mathbf{E} / \partial t \right)_{MAX}}{\left(\sigma \mathbf{E} \right)_{MAX}} \right\| = \frac{\varepsilon_0 \omega}{\sigma} \approx 10^{-13} \omega, \tag{1.7}$$

where ω is the circular frequency that can describe a periodically fluctuating electric field in rad/s. The above relationship shows that the displacement current is negligible for weakly ionized gas EMFC applications unless the electric field is pulsed at very high frequencies. Some high voltage ionization methods indeed use high pulse frequencies, but MHz frequencies still do not let the term reach unity. Even if the frequency is increased further, the duty cycle of the pulse is often low enough in these systems that the time in which the displacement current may be appreciable is itself negligible.

The current due to the transport of excess charge is also negligible. A comparison of the excess charge $\rho_e \mathbf{u}$ with the conduction current can be written as

$$\left\| \frac{\rho_e \mathbf{u}}{\sigma \mathbf{E}} \right\| \approx \frac{\left(\varepsilon_0 E / L \right) u}{\sigma E} = \frac{\varepsilon_0 u}{\sigma L} \tag{1.8}$$

Choosing $\varepsilon_0 = 10^{-11}$ F/m, $\sigma = 100$ ℧/m, a freestream velocity $u = 10^4$ m/s and $L = 0.1$ m to simulate weakly ionized gas flow still results in a value of the above ratio of only 10^{-2}. This value decreases with a reduction in velocity, keeping the excess charge negligible for boundary-layer flow. Additionally, the freestream speed and conductivity will likely be lower for EMFC than these intentionally high values used here.

The force acting on an ionized gas due to the presence of an electromagnetic field can be defined as

$$\mathbf{F} = \rho_e \mathbf{E} + \mathbf{J} \times \mathbf{B}, \tag{1.9}$$

where

$$\|\rho_e \mathbf{E}\| \approx \frac{\varepsilon_0 E^2}{L}. \tag{1.10}$$

Neglecting the Hall effect, which may significantly affect EMFC actuator performance (but not an order of magnitude comparison), the cross product of $\mathbf{J}$ and $\mathbf{B}$ can be approximated as

$$\|\mathbf{J} \times \mathbf{B}\| \approx \sigma B \left(E + uB\right). \tag{1.11}$$

Next, the ratio of $\rho_e \mathbf{E}$ to $\mathbf{J} \times \mathbf{B}$ may be compared accordingly.

$$\left\| \frac{\rho_e \mathbf{E}}{\mathbf{J} \times \mathbf{B}} \right\| = \frac{\varepsilon_0 E^2}{L \sigma B \left(E + uB\right)} \tag{1.12}$$

Again, consider a weakly ionized gas with $L = 0.1$ m, $\sigma = 100$ ℧/m, $B = 1$ T, $u = 10^4$ m/s, $\varepsilon_0 = 10^{-11}$ F/m, and $E = 10^6$ V/m, which simulates flow over an electrode where the electric field is concentrated. The result is still a negligible value on the order of 10^{-2}. This quantity shows that the electrostatic force can be neglected for EMFC even with very high electric fields. Again neglecting the Hall effect, the Lorentz body force can be approximated as

$$\|\mathbf{F}_L\| \approx \sigma \left(E + uB\right) B \tag{1.13}$$

With these approximations made, a system of four simplified magnetohydrodynamic equations can be derived:

$$\frac{\partial p}{\partial t} + \nabla \cdot (\rho \mathbf{u}) = 0 \tag{1.14a}$$

$$\rho \frac{D\mathbf{u}}{Dt} = -\nabla \mathbf{p} + \psi + \frac{(\nabla \times \mathbf{B}) \times \mathbf{B}}{\mu_0} \tag{1.14b}$$

$$\begin{aligned} \rho \frac{\mathrm{D}\epsilon}{\mathrm{Dt}} = -p \nabla \cdot \mathbf{u} - \left[\frac{2}{3} \mu \left(\nabla \cdot \mathbf{u} \right)^2 - \mu \left[\nabla^2 \left(u_j^2 \right) - \left(\nabla \times \mathbf{u} \right)^2 - 2\mathbf{u} \cdot \nabla^2 \mathbf{u} \right] \right] \\ + \nabla \cdot (\kappa \nabla T) + \frac{\left(\nabla \times \mathbf{B} \right)^2}{\mu_0^2 \sigma} \end{aligned} \tag{1.14c}$$

$$\frac{\partial \mathbf{B}}{\partial t} = \nabla \times (\mathbf{u} \times \mathbf{B}) - \frac{1}{\mu_0} \nabla \times \frac{\nabla \times \mathbf{B}}{\sigma} - \nabla \times \left[\frac{\beta}{\mu_0} (\nabla \times \mathbf{B}) \times \mathbf{B} \right] \tag{1.14d}$$

The first three are the conservation of mass, equation of motion, and conservation of energy equations, respectively. Equation (1.14d) is known as the induction equation, where a change in the local magnetic field is related to separate diffusion and convection terms.

CHAPTER 2

MHD INTERACTION

2.1 Overview

Fifty years ago, an article was written describing the prospects for "Magneto-Aerodynamics" [13]. In it, Resler and Sears stated that an electromagnetic field could be coupled with an ionized gas flow to accelerate or decelerate it, delay boundary layer separation, or to control skin friction and heat transfer. With several additions since that time, these goals remain the same. The authors also discussed several advancements critical to the progress of electromagnetic flow control. Among them was the ability to solve the complex magnetohydrodynamic equations, which has eased tremendously stemming from the development of powerful computing hardware and numerical methodologies. Next, Resler and Sears mentioned that powerful magnets would be needed for ionized fluid flow control. This requirement of high strength magnets has been achieved to some extent. Electromagnets can produce fields of several tesla, and superconducting magnets can reach tens of tesla. However, the size of these magnets makes their integration into an aerospace vehicle problematic. Also, the magnets are dependent upon large power supplies. Similarly, research into rare-earth materials has progressed considerably since 1958, with inexpensive neodymium-based magnets currently available with maximum surface fields in the 0.5–1.0 T range. However, their use for aerodynamic control is limited since their magnetic fields are reduced as temperature is increased, making their incorporation into applications like scramjet inlets difficult if not impractical.

In addition to the strength of the magnetic field, EMFC is also dependent upon the conductivity of the ionized airflow. Resler and Sears believed that artificial seeding of the airflow to create higher plasma conductivities would need development. At the time, plasma jet sources were capable of creating high values of conductivity for ground testing. As an example, consider a linear Lorentz force accelerator developed in the 1960's [14]. The accelerator had a square cross-section of 2.54 cm sides at the inlet that diverged to about 2.54 × 5 cm at the exit with an overall length of 76 cm. The 60 electrode pairs in the accelerator were powered by a warehouse of 1700, 12 V automotive batteries. The current draw of the accelerator electromagnets reached up to 900 A at 80 V. Finally, the plasma generator operated with a 10 MW power supply, and could create a flow with a conductivity of up to 500 ℧/m (with seeding). In order to reduce the power requirement, seeding the plasma jet with low ionization energy potassium and cesium compounds was explored, which resulted in a tremendous increase in conductivity relative to the unseeded gas. For instance, a hypersonic vehicle flying at an altitude of 30 km at Mach 16 would ionize the air after a bow shock to $\sigma \approx 0.05$ ℧/m. Adding 0.1 percent potassium by weight could boost the conductivity to roughly 1 ℧/m [15, 16], a twenty-fold increase. However, the vehicle-scaled power requirement of an air-breathing engine incorporating thermal ionization and thrust generation by an electromagnetic accelerator currently may only be met by a system such as an on-board nuclear reactor. Research in this field waned by 1970.

For control surface aerodynamics, thermal ionization, whether augmented by seeding or not, may not be feasible or even desirable. Its benefits and drawbacks have been discussed for concepts like the MARIAH hypersonic wind tunnel facility [17] and the AJAX scramjet power generator [18]–[20]. In particular, seeding may contaminate the flow of the MARIAH wind tunnel. At speeds below that which result in significant shock-induced ionization, EMFC may have serious limitations compared to its overall benefits since a separate non-thermal ionization system must be utilized. A few situations do exist in which ionization is currently experienced by an aerospace vehicle. For instance, the Space Shuttle interacts with ionized particles while in low Earth orbit [21] and during re-entry, where the re-entry environment has resulted in numerous studies (e.g., Refs. [22, 23]) of how to improve current vehicle designs with the addition of electromagnetic fields. However, with the Space Shuttle's impending retirement and no new prospects for the incorporation of actuators into full-scale space vehicles (assuming the Orion design is nearly finalized), less grandiose platforms like hypersonic missiles may currently be the best near-term candidate for EMFC systems. With that in mind, the flight Mach number may be limited to below about 15, for which artificial creation of an adequate amount of flow conductivity is necessary. Recently, generation of a conductive gas, also known as a weakly ionized gas (WIG), has been accomplished using high voltage fields, laser beams, or perhaps directed microwaves [24, 25]. However, these ionization methods produce a far lower level of conductivity when compared with results from fifty years ago. Experimentally, the maximum realized values of σ in air are currently in the 0.1–1 ℧/m range with high voltage fields. Raising the gas conductivity and minimizing power consumption are obviously priorities if practical aerospace systems are to be realized.

Also of significant note has been the development of flow control systems utilizing only an electric field to create plasma. The design of an EFC device with only a high voltage field is much less complex since the field will ionize the air itself. Electrohydrodynamic flow control techniques can be divided into two categories: glow discharges and dielectric barrier discharges. The physics for the two categories is similar. An air gap exists between the anode and cathode region of a glow discharge, while a much thinner dielectric material barrier is used for DBD systems which limits arcing. Paschen's law states that the electrical breakdown voltage is based on gap distance and pressure. Because the anode and cathode of a DBD are separated by a thin dielectric gap, the operating pressure is higher and additionally the high electric field significantly raises the output Coulomb body force. Because of a larger air gap distance, most glow discharge research has occurred with low pressure and the control mechanism is thought to be more of a thermal effect. Although both systems solve the conductivity generation problem by ionizing the air without a separate system, the value of σ is very low, perhaps 10^{-5}–10^{-7} $\mho$/m. Both systems also operate often using low power requirements that may be met by current on-board generators.

One may assume the magnitude of the force generated by electric or electromagnetic fields is naturally a reflection of the amount of power consumed. Considering the potential use of each in the aerospace industry, there is a tendency to associate electromagnetic fields with systems consuming a large amount of power. Systems based solely on the Coulomb force have been proposed and used for applications with relatively less power (i.e., electrostatic ion thrusters and ion lifters). Therefore, a fundamental issue to address for the future of flow control using these fields is defining how much power is needed for an appreciable control force. Put another way, while an electromagnetic field is generally associated with larger scale aerospace applications and may be more robust, an electric field may be all that is necessary to generate a satisfactory control force. The answer to this question will likely cause one to eventually be far more appropriate for use over the other.

Recent experimental results have not entirely addressed this issue, although some progress has been made. Aerospace research involving electromagnetic fields has focused on hypersonic flows [26], particularly for the augmentation of scramjet propulsion systems. Most work involving MHD and scramjets has been computational, which is clearly understandable due to the cost and complexity of testing.

However, this situation has led to significant differences between experimental and computational work. Experimental values of pressure, conductivity and magnetic field strength are usually below what is assumed analytically or in computational simulations. For example, Bruno et al. assumed a magnetic field between 7–17 T as part of a first-order electromagnetic hypersonic propulsion system [27]. In another design, Park et al. computed values of $B = 11.28$ T, $\sigma = 35.87$ ℧/m (with seeding) and $p = 1.25$ MPa at the entrance to the scramjet's MHD accelerator [28]. Recent experimental environments have been generally limited to 0.5–4.0 T, at most a few ℧/m, and pressures low enough to be appropriately stated in torr. Low pressure testing has been a method to increase I_M understandably as such conditions facilitate ionization. Little discussion has been articulated on the subject matter of selecting appropriate values of these parameters for aerodynamic control surfaces. Interestingly, these experimental values of B, σ and p might be better suited for control surfaces rather than for propulsion systems. Practical values of crucial scaling parameters must be established so as to define what value ranges should be associated with larger, propulsion-associated systems and smaller control surface systems.

Conversely, electrohydrodynamic flow control surfaces have mostly been experimentally demonstrated with low freestream speeds and Reynolds numbers [29]. These demonstrations represent a significant departure from the high-speed flight regime where electric and electromagnetic fields were first considered for use. This situation is especially true for DBDs. High-speed experimentation has appeared with glow discharges, but the studies have historically centered upon bluff bodies more than aerodynamic surfaces. Again, static pressure is often in the range of a few torr to facilitate the creation of a diffuse electrical discharge. Although the high-speed control effect of glow discharges appears to depend more on the reduction of the local speed of sound caused by Joule heating rather than the presence of an electrohydrodynamic force, rapid control actuation is desirable. Increasing the Reynolds number while still providing effective control with these systems is crucial. For flow environments besides very low speeds where DBDs appear best suited, glow discharge and EMFC concepts are competitive for a wide range of control possibilities.

2.2 EMFC Actuator Characterization

2.2.1 Electric and Electromagnetic Force Comparison

The central difference between electrohydrodynamics (EHD) and magnetohydrodynamics (MHD) is the force produced during the interaction of ionized particles with the electric or electromagnetic fields, respectively. For EHD, it is the Coulomb force while for MHD it is the Lorentz force. These interactions are often summed up in one equation written as

$$\mathbf{F} = q\left(\mathbf{E} + \mathbf{u} \times \mathbf{B}\right). \tag{2.1}$$

With research in electric and electromagnetic flow control beginning to focus mainly within the boundary layer where E is high and u is low, there is a tendency to observe Eq. (5.1) and conclude that the presence of a magnetic field has little effect on the magnitude of the body force from a simple order-of-magnitude comparison of the two terms on the right hand side. This conclusion is incorrect since both RHS terms of Eq. (2.1) actually contain an electric field component. Note that the $u \times B$ product is actually an electric field, usually referred to as the internal induced electric field in channel flow applications. The single E term is referred to as the applied or external electric field for accelerators and generators, respectively. Interaction of only an electric field with ionized particles will produce a body force, but its relative magnitude with respect to the force produced by an electromagnetic field cannot easily be determined by Eq. (2.1). A strong current field interacting with ionized particles can create an induced magnetic field, but that field and any body force generated from that interaction is likely negligible for EMFC as will be shown. The concepts above have been well established in the literature [12, 30].

In order to provide insight to MHD interaction and scaling, a derivation of the EHD and MHD forces is useful. Coulomb's law states that two charged particles exert a mutual force in a direction parallel to the line connecting each particle. If one of these particles is held stationary in the reference frame of the other one, it creates an electric field and exerts a force on the other particle, written as

$$\mathbf{F}_2(\mathbf{r}_2) = eZ_2 \left[\frac{eZ_1}{4\pi\varepsilon_0} \frac{(\mathbf{r}_2 - \mathbf{r}_1)}{|\mathbf{r}_2 - \mathbf{r}_1|^3} \right] \tag{2.2}$$

where the bracketed term represent the electric field. Similarly, the magnetic force law states that a force is developed between two current carrying wires which is dependent on distance and, additionally, the orientation of the wires. Over a length of wire **dl** this force is written as

$$\mathbf{dF}\,(\mathbf{r}) = \frac{\mu_0}{4\pi} \frac{I\,I'}{|\mathbf{r} - \mathbf{r}'|^3}\, \mathbf{dl} \times [\mathbf{dl}' \times (\mathbf{r} - \mathbf{r}')]\,, \tag{2.3}$$

where the prime is used to denote the properties of one wire from another. Invoking the Biot-Savart law leads to an expression for the magnetic field at r, namely,

$$\mathbf{B}(\mathbf{r}) = \frac{\mu_0}{4\pi} \int\limits_{l'} \frac{I'(\mathbf{r}')\,\mathbf{dl}' \times (\mathbf{r} - \mathbf{r}')}{|\mathbf{r} - \mathbf{r}'|^3}. \tag{2.4}$$

Next, using Ampere's law, Eq. (2.3) can be simplified to

$$\mathbf{dF}(\mathbf{r}) = I(\mathbf{r})\,\mathbf{dl}(\mathbf{r}) \times \mathbf{B}. \tag{2.5}$$

If S denotes the cross-sectional area of the wire, n denotes the number of particles and the subscript p denotes a particle along the wire, then the force is

$$\mathbf{dF} = n_p e Z_p S\, dl\, \mathbf{u}_p \times \mathbf{B}. \tag{2.6}$$

Furthermore, the force on one particle is

$$\mathbf{F}_p = eZ_p\mathbf{u}_p \times \mathbf{B}. \tag{2.7}$$

Therefore, the combined electric and magnetic forces on a particle are

$$\mathbf{F}_p = eZ_p\left(\mathbf{E} + \mathbf{u}_p \times \mathbf{B}\right). \tag{2.8}$$

Neglecting polarization and magnetization effects, the body force components on an ionized gas or liquid is shown in Eq. (2.9), which also has omitted the Hall effect (which can be significant) and ion slip.

$$\mathbf{F} = \rho_e\mathbf{E} + \mathbf{J} \times \mathbf{B}. \tag{2.9}$$

Next, the order of magnitude of these electric and electromagnetic Lorentz force components can be approximated, allowing for a comparison between the two [12]

$$\rho_e E \approx \frac{\varepsilon_0 E^2}{L} \tag{2.10}$$

$$F_L = |\mathbf{J} \times \mathbf{B}| \approx \sigma\left(E + uB\right)B \tag{2.11}$$

The relative magnitude of the two terms approximating F_L in Eq. (2.11) are critical for EMFC characterization. From Eqs. (2.10) and (2.11), the ratio of the electrohydrodynamic force to the magnetohydrodynamic force is

$$\frac{F_{EHD}}{F_{MHD}} = \frac{\rho_e E}{|\mathbf{J} \times \mathbf{B}|} = \frac{\varepsilon_0 E^2}{\sigma L\left(E + uB\right)B}. \tag{2.12}$$

With the potential difference between electrodes on MHD accelerators and recent EMFC actuators usually on the order of 1000 V or less, it is apparent that the electrohydrodynamic force will be negligible, unless the characteristic length is very small. Aerodynamic control systems will operate in far larger environments.

2.2.2 Scaling Parameters

For EMFC characterization, it appears that much progress is needed to support experimental research. Historically, the magnetic interaction parameter I_M has been used to define the ratio of magnetic body force to the inertia of the fluid.

$$I_M = \frac{\text{EM forces}}{\text{Inertia forces}} = \frac{\sigma B^2 L}{\rho u} \tag{2.13}$$

The prospects of reaching $I_M \approx 1$ was discussed as a performance benchmark in literature decades ago (e.g., Ref. [31]) and has seen use again with many recent EMFC publications. However, these recent EMFC environments usually demonstrate $I_M \ll 1$ and it takes a combination of very high flow speed and low density to reach unity. Despite having a low value, these same experimental results still demonstrate appreciable changes to the flow. As Elsasser remarked, dimensional relations in magnetohydrodynamics are often much larger or much smaller than unity [32]. Perhaps other dimensionless numbers are more suitable for characterizing and scaling the effects of EMFC. With pressure changes often measured to confirm the effect of the Lorentz force, variables to consider include B, E, ρ, p, u, L, and σ. Table 2.1 below shows several resulting dimensionless numbers derived using the Buckingham Pi theorem.

The most common term developed from Table 2.1 is E/Bu, referred to as the MHD loading parameter. It can be seen as a ratio of the total power per unit volume added to the flow to the directed kinetic energy [14]. As such, the parameter should be minimized to raise the conversion efficiency of energy used to accelerate the flow (rather than letting it contribute to Joule heating). From the last combination of variables, E/Bu and I_M are formed. As is common with Buckingham Pi theorem results, two dimensionless numbers can be multiplied to form further dimensionless

Table 2.1. Resulting dimensionless numbers for several EMFC variable combinations

Variable combinations	**Dimensionless numbers**
$B,\ E,\ \sigma,\ u,\ p$	$\frac{E}{Bu}$
$B,\ E,\ \sigma,\ u,\ \rho$	$\frac{E}{Bu}$
$B,\ E,\ \sigma,\ L,\ p$	$\frac{BE\sigma L}{p}$
$B,\ E,\ \sigma,\ L,\ \rho$	$\frac{B^3\sigma L}{E\rho}$
$B,\ E,\ \sigma,\ L,\ p,\ u$	$\frac{E}{Bu};\frac{BE\sigma L}{p}$
$B,\ E,\ \sigma,\ L,\ \rho,\ u$	$\frac{E}{Bu};\frac{\sigma B^2 L}{\rho u} \rightarrow \frac{BE\sigma L}{\rho u^2}$

parameters. Usually only a few will have significance, and one to highlight from that set is distinguished as the electromagnetic interaction parameter.

$$I_{EM} = \frac{BE\sigma L}{\rho u^2} \tag{2.14}$$

This parameter, like I_M, is a ratio of the magnetic body force to the fluid inertia. It is interesting to note their individual similarity to one of the respective Lorentz force components shown in Eq. (2.11). Although $E \approx Bu$ has been assumed in the derivations of many publications (e.g., Refs. [12, 32]), this assumption is not necessarily valid for small-scale environments like boundary-layer EMFC where E is high and u is low. In fact, it appears that I_{EM} and I_M are useful over separate design spaces depending on where $E \gg uB$ or $E \ll uB$, respectively. The term $B^3\sigma L/\rho E$ has not seen use, and is another product of the MHD loading factor and the interaction parameter. The term developed in the third row is interesting since it relates a magnetic force to static pressure, which may prove to be useful with further experimental testing. Another modified interaction parameter that has appeared in the literature is [24],[33]–[35]

$$I_{BL} = \frac{\sigma B^2 L}{\rho u_\infty \sqrt{c_f/2}}. \tag{2.15}$$

This term defines u as the friction velocity, whereby $u^+ = u_\infty \sqrt{c_f/2}$. As research into boundary layer EMFC increases, this term and velocity profiles using the inner-law variables should be useful in comparing effects over different test facilities.

As an example of the importance of these parameters, consider a flat plate, electromagnetic flow control actuator with five surface electrodes each separated by 1.59 cm of dielectric material as shown in Fig. 2.1. The electrodes alternate with embedded magnets. The figure is a computer rendition of an actuator presented further on in this thesis, with the dielectric material shown as transparent. Such actuator geometry may be typical for surface EMFC as the field progresses. Flat plate actuators with alternating magnets and electrodes have been previously demonstrated with salt water environments as can be seen in [34] along with a discussion of related research. The middle and outer electrodes are grounded, while the potential of the other two is 500 V. The length and width of the electrodes are 1.27 and 0.51 cm, respectively. The permanent, NdFeB magnets, 1.27 cm square by 2.54 cm long, are embedded about 1 mm below the surface. The measured magnetic field across the surface of the actuator B is shown in Fig. 2.2. Next, assume this device is operating under a freestream airflow of 1000 m/s. The conductivity of the air is arbitrarily set to be 1 ℧/m, produced by a separate ionization system. The boundary layer thickness has been fixed at 1.0 cm and the velocity profile follows a typical turbulent shape.

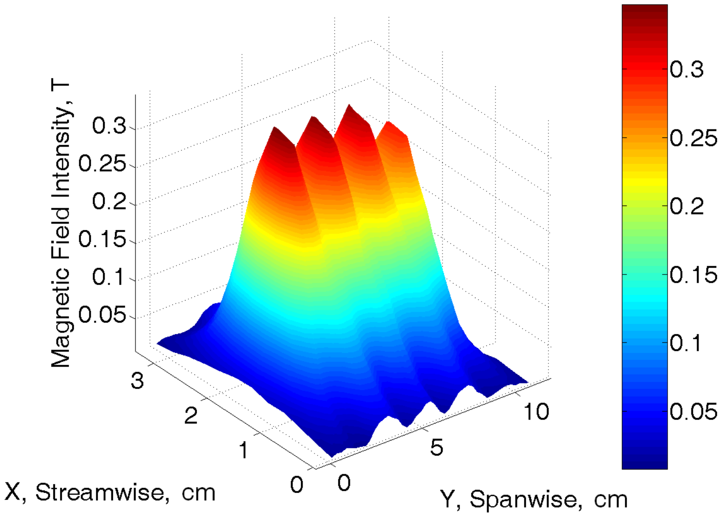

Figure 2.1. Image of the five electrode, four magnet actuator plate with dielectric material shown as transparent.

The boundary layer velocity as a function of height off of the flat plate is denoted as $u_{BL} = u\left(z\right)$.

The magnetic field components (B_x and B_y), actuator geometry, and electrode potentials were used as boundary conditions in a computational MHD code to determine the Lorentz force and interaction parameters [36]. The magnetic field generated showed reasonable agreement with experimental magnetic field measurements that were taken up to $z = 1.27$ cm.

Figure 2.3 shows the common logarithm of the local Lorentz force for a two-dimensional spanwise slice over the actuator at $x = 1.8$ cm. The locations of the magnets and electrodes are labeled at the bottom. The Lorentz force is most heavily concentrated over the electrodes and especially at their edges where electric charge builds. The magnitude of the Lorentz force produced in part with the NdFeB magnets drops significantly with height, but remains viable for boundary layer applications. The Lorentz force is not as high over the outer electrodes because they are grounded.

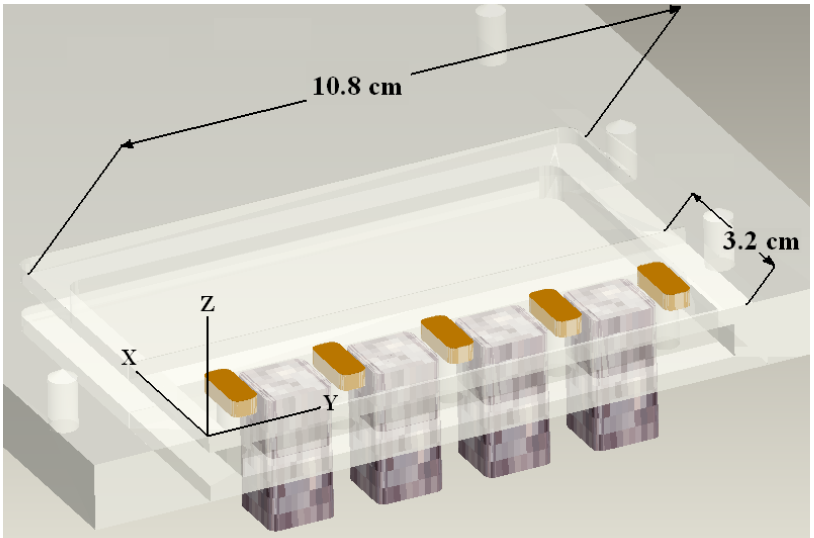

Figure 2.2. Total magnetic field located on the surface of the flat plate over the 10.8 × 3.2 cm area.

In this spanwise arrangement, it is important to keep the outer electrodes grounded to prevent a counteracting body force from developing past the edges of the actuator.

Figures 2.4 and 2.5 show the common logarithm of the local interaction parameters I_M and I_{EM}, respectively. Logarithms are used for two reasons, first, because the localized values range over several orders of magnitude. Second, the similarities and differences between the figures are more important than the actual values. For the calculation of the parameters, ρ was approximated as 1 kg/m^3 throughout the boundary layer. (In actuality it will increase or decrease towards the surface depending on the wall conditions.) Additionally, L was removed from the parameters since it is not meaningful for the two-dimensional slice of interest. Figure 2.4, as would be expected, shows I_M distinctly centered upon the embedded NdFeB magnets. If I_M is truly a good choice as a non-dimensional representation of the Lorentz force for this actuator, then the localized contours of Figs. 2.3 and 2.4 would be similar. An evaluation of the data used for this example indeed shows that $E \gg uB$ across the

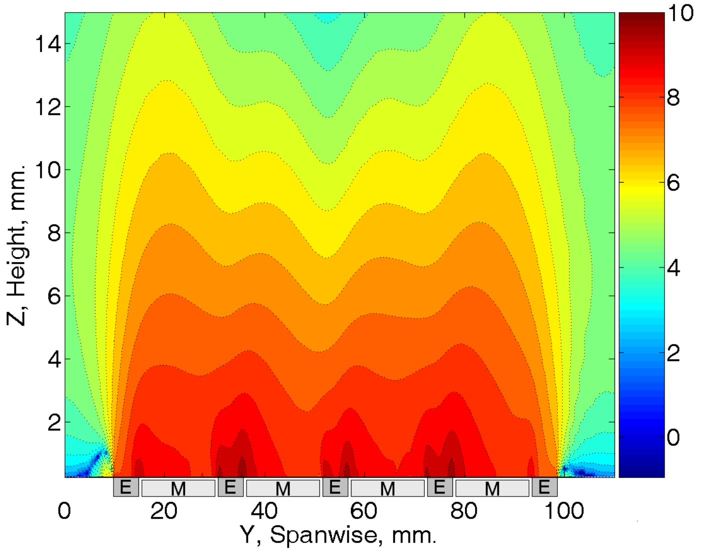

Figure 2.3. The common logarithm of the Lorentz force (N/m^2) across a spanwise slice over the actuator at $x = 1.8$ cm.

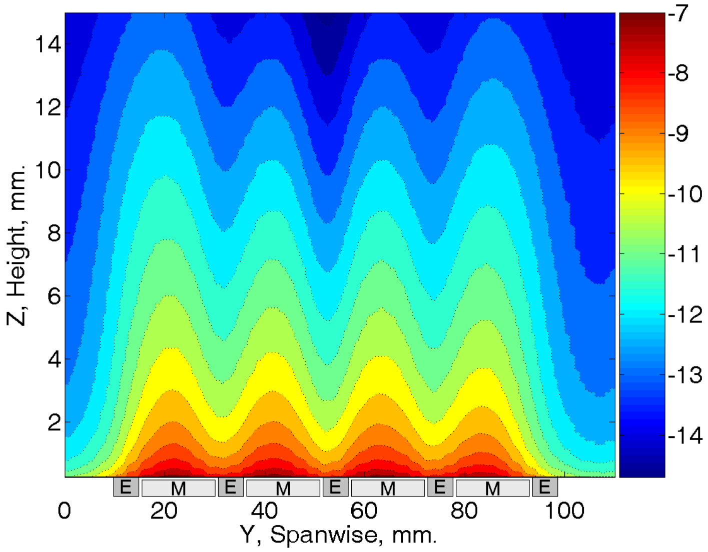

Figure 2.4. The common logarithm of I_M/L across a spanwise slice over the actuator at $x = 1.8$ cm.

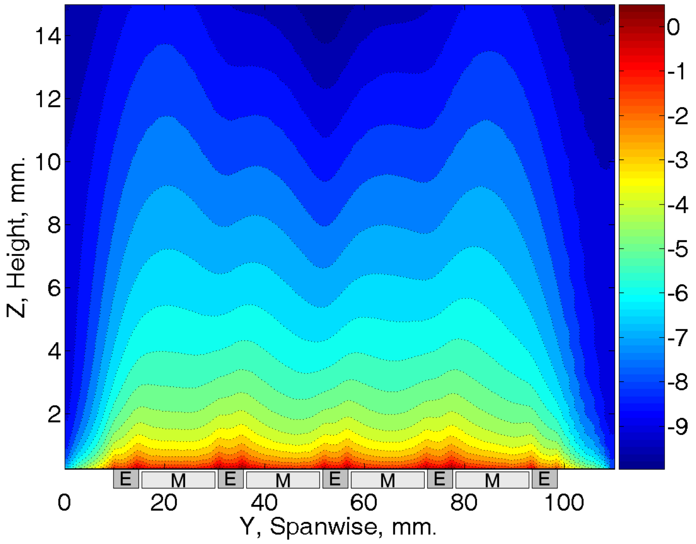

Figure 2.5. The common logarithm of I_{EM}/L across a spanwise slice over the actuator at $x = 1.8$ cm.

boundary layer. Figure 2.5 shows that the Lorentz force more appropriately follows the same contours as I_{EM}. In Fig. 2.5, the maximum values of I_{EM} are centered on the electrodes. The only difference between the figures is I_{EM} is more uniform near to the actuator surface because of the use of u_{BL}^2.

The consequences of selecting the correct interaction parameter for an actuator will have a larger impact than the comparison of these figures. Most important, the performance will scale differently with E, B, and u depending on the value of the MHD loading parameter. On a case-by-case basis, the average of the localized MHD loading parameter in the boundary layer should be known before the actuator and its operating conditions are characterized by I_M or I_{EM}. Although I_M has been more widely used than I_{EM}, the example shows that the design space over which I_{EM} is applicable is significant. Also, where $E \approx Bu$, neither term may be appropriate for correctly scaling the Lorentz force effects.

Going back to Fig. 2.3, the Lorentz force is noticeably non-uniform across the span of the actuator. This may be unavoidable for surface actuators since the electric and magnetic fields have inherently large gradients. The simplest strategy for creating some uniformity is to match the maximum B field points with the minimum E field points and vice versa along the actuator surface. Earlier MHD studies have shown that the geometry of segmented electrodes has a large impact on the distribution of the electric field [37], and that observation certainly applies to this example actuator. As the MHD loading parameter decreases, the maximum Lorentz force locations will gradually shift from over the surface of the electrodes to over the magnetic poles.

Computing these local parameters is only practical in a computational environment, but doing so may be necessary before accurately scaling the performance of the actuator with any particular interaction parameter. Establishing u as the friction velocity in the manner of I_{BL} for comparison purposes across different facilities is recommended.

Continuing on, the magnetic Reynolds number is a measure of the ease with which an ionized gas moves through a magnetic field, and is defined as

$$Re_M = \mu_0 \sigma u L. \tag{2.16}$$

The number can also be seen as a ratio between convection and magnetic diffusion effects, where diffusion (and therefore B) dominates the system for $Re_M \ll 1$ [38]. When $Re_M > 1$, the motion of charged particles in a current field can create an induced magnetic field b, responsible for many astrophysical phenomena. A relationship between the magnetic Reynolds number, the current field, and the induced magnetic field is

$$Re_M \mathbf{J} = \nabla \times \mathbf{b}. \tag{2.17}$$

With the aforementioned ranges of σ, u, and L, the magnetic Reynolds number is far lower than unity within the boundary layer for this example actuator. This result should be true for most if not all EMFC actuators, as the creation of an induced magnetic field for a flight vehicle needs a combination of very high speed and a current field likely too large to be supplied by an on-board generator.

CHAPTER 3

CRITICAL ISSUES IN EMFC ACTUATOR DESIGN

For electromagnetic fields to be successfully implemented in a control surface actuator, several issues must be considered. First, while channel flow setups are ideal for understanding the physics of EMFC, open flow experiments must be considered in which the EMFC actuator is contained in a flat plate or airfoil. Power consumption and packaging are important issues to address, with the selection of magnets and the method of ionization being key to success. The selection of EMFC magnets is a significant matter since rare-earth materials would be ideal for placement within a control surface, except for the major problem in which their field strength is relatively low and adversely affected by heat. Finally, unlike EFC, a sufficiently high value of conductivity must be created by an additional means if thermal ionization is unavailable in the flight regime.

3.1 Channel Flow and Open Flow Experimentation

While one of the focal points of EFC has been for control surfaces, the same cannot necessarily be said for EMFC systems thus far. EMFC experiments applied to aerospace systems have typically been for scramjet-like systems and have taken place in a channel flow environment. Analytical approaches have also been well established for MHD channel flows while open flow modeling requires more sophistication. The design highlights and operating conditions of several recent facilities are discussed below. Ionization systems for each facility will be elaborated upon further into the text.

One recent channel flow facility has been developed with the intent to developing an accelerating or retarding Lorentz force on a Mach 3–4 flow of air or another mixture of gases [1, 8, 24, 33],[39]–[46]. The walls of the test section each have electrodes mounted into them. Two electrodes mounted opposite of each other create a WIG in the test section using high voltage, low duty cycle pulsing while the other two are connected to a DC system. That system provides the energy for the Lorentz force so long as the level of conductivity provided by the ionization electrodes is enough for current to cross the electrode gap. The Lorentz force may be applied with or against the flow depending on the electrode and magnet polarity. Experimental data collected has included flow visualization, flow fluctuation measurements, Lorentz force induced pressure changes, and the output of the ionization and Lorentz force systems.

The test section static pressure of this facility ranges from 5–20 torr. The channel itself is small enough to be surrounded with an electromagnet that can reach $B = 2$ T, while a NdFeB magnet configuration ($B \approx 0.4$ T) was also demonstrated in earlier works [24, 41]. A decrease was measured in the pressure fluctuation due to the Lorentz force in [24], but no direct measurements of pressure were taken at the time. The flow conductivity from the ionization system has risen with more recent publications, and is usually on the order of 0.1 ℧/m. Further studies with electromagnets have shown large pressure differences created by the Lorentz force. For instance, Nishihara et al. [40] have shown a static pressure increase of 17–20% for a retarding force and 5–7% for an accelerating force of the same magnitude. Similar data of greater magnitude from [1] is shown in Fig. 3.1. The figure shows the normalized pressure difference for dry air between unaltered flow, flow with a retarding force, and flow with an accelerating force. The retarding force is more effective than the accelerating force because it works with Joule heating to create the rise in pressure, while the accelerating force works against Joule heating. The magnitude of the pressure rise also appears to be dependent upon Lorentz force polarity, where it is suggested that the test section Mach number and pressure are affected by the electromagnetic force interaction.

Another channel flow test section has been constructed to explore the effects of a constricted plasma column operating under the presence of a magnetic field [47]. In the test section, two tapered electrodes were placed on the side of one of the tunnel walls. After actuating a high voltage DC circuit, a constricted plasma column forms between the electrodes and propagates downstream due to the tapering. A helium-cooled superconducting ring magnet surrounds the channel and can generate a B field up to 7 T, which increases the velocity at which the plasma column travels [48]. Since EFC systems are based on momentum transfer due to collisions between the ions and a neutral flow, this system can be seen as a novel method to enhance the momentum transfer using magnetic fields. Instead of two separate power supplies for ionization and Lorentz force generation, a single 20 kV, current regulated power supply is used. The electric field generated by the 20 kV potential ionizes the gas to the point of breakdown, and the resulting arc draws up to a specified current limit. Once the current limit is reached, the power supply voltage drops significantly, so the power input into the flow is considerably less than its maximum value of 20 kW. Therefore, the initial 20 kV potential before breakdown acts like an ignition system for the EMFC actuator.

The test section has a Mach number of 2.8 and static pressure of 28 torr. Experimental data collected consisted of static pressure measurements in addition to flow visualization. A wedge was placed inside the test section to study the effects of the system on shock/boundary layer interaction [48]. Results show that the actuator is able to move the separation bubble induced by the shock interaction, and the static pressure across the wedge is affected.

A third facility has been developed with a flat plate secured inside a free jet test section designed for basic research in magnetohydrodynamics [49]. An electromagnet with a maximum field of 3.5 T surrounds the entire channel, and a NdFeB configuration has also been tested. The Mach number in this facility is about 5.0, and the test section static pressure is designed to simulate an altitude between 30 and 50 km (approximately 0.6–7 torr). Besides covering the altitude range mentioned, the low test section pressure has also been designed with consideration to raising the value of I_M, which reaches approximately 1.5 per meter. The flat plate, shown in Fig. 3.8, has two embedded electrodes which use high voltage DC, RF, or a combination of both fields to ionize the air up to 2.5 $\mho$/m. The figure also shows the rarefied air pressure in the test section allows for a relatively low voltage glow discharge to transmit a substantial amount of power to support the Lorentz force.

Before incorporating a flat plate into the facility, tests were conducted with blunt body configurations at Mach 5.8 where experimental results included plasma diagnostics and aerodynamic force measurement [50]. For the flat plate configuration, surface pressure measurements indicated that a Lorentz force directed out of the plate has more of an effect than directing it into the plate, again due to flow coupling and Joule heating issues [51]. Both push the luminous region of the glow discharge onto or off the actuator surface. Although a glow discharge raised lift by up to 18% in one set of experiments, applying a magnetic field can negatively affect the discharge and void the change in lift [4]. A more recent study has moved to testing rectangular and cylindrical inlets supported by computational modeling [7].

EMFC publications have increased in the past few years and other facilities are likely to join those above. The ionization systems and overall electrode design for the generation of a WIG or plasma column and interaction with a magnetic field to produce the Lorentz force appear to be feasible for high-speed, boundary-layer EMFC based on results from these facilities. However, the value of conductivity generated (0.1–2.5 ℧/m) by the high-voltage systems as well as the test section pressure are several orders of magnitude below those that may be necessary for the AJAX engine concept. It would be very interesting to modify the geometry and examine the performance of these facilities under an open flow, flat plate environment with pressures closer to what may be encountered by a wing or fin during high-speed flight. Magnets for such applications should also be embedded in the surface. Control of slender wings and fins, and perhaps the initial stage of an inlet compression system, are likely the best applications for these systems. If changing the geometry and increasing p are not formidable obstacles, perhaps these types of systems could be placed on a high-speed missile for control purposes.

With electromagnetic fields, experimental measurements can be difficult because of signal interference. Typically, one or more transducer ports are placed downstream of the electromagnetic arrangement to capture the change in static pressure resulting from the Lorentz force. These data, along with flow visualization, power input, and plasma diagnostics results provide the means to understand the basic physics of EMFC. The measurement of aerodynamic forces, conducted in a few studies, will need to become more widespread as the actuator designs become more representative of control surfaces. Since most EMFC studies have been primarily focused on boundary layer control, it is desirable to use more refined techniques to analyze changes to the boundary layer profile. The inherent non-uniformity of the Lorentz force field likely adds unusual effects that must be measured as a function of height above the plate as well as in the spanwise direction. Figure 3.2 shows an example of the change in boundary layer profile for a low-speed salt water freestream flow of about 18 mm/s as measured with a particle image velocimetry (PIV) system. Since salt water is naturally conductive (a few ℧/m), flat plate Lorentz force actuators have been much

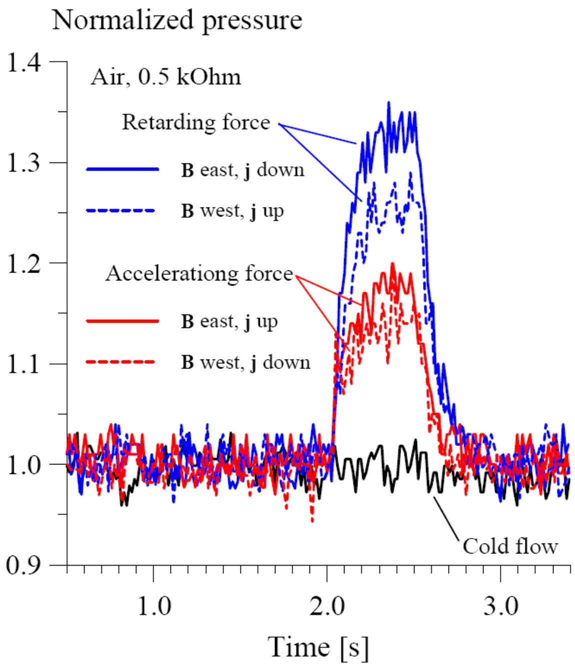

Figure 3.1. Normalized static pressure traces downstream of an EMFC actuator for M = 3 dry air for four electromagnetic arrangements (from [1]).

easier to build, test, and characterize [2, 34]. PIV imaging directly over an EMFC actuator for gas flow may be difficult because of the luminosity of the ionized gas and Lorentz force energy addition.

Although the flow speed in Fig. 3.2 is very low, other research with salt water has been conducted at higher speeds. The concept of electromagnetic flow control and propulsion for naval applications has existed just as long as it has for aircraft [52]. The concept has also been proven with subscale submarines and ships [53, 54]. Studies of MHD propulsion have concluded that it is feasible and desirable because of stealth [55], but effects from bubble formation at the electrodes in salt water and the generation of hydrogen and chlorine gas will need mitigation. MHD propulsion for a full-scale submarine will require significant power and new developments in efficiency for on-board nuclear reactors.

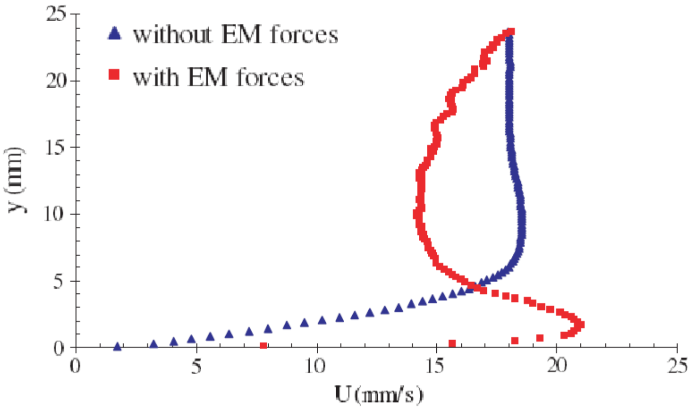

Figure 3.2. Boundary layer velocity profile downstream of a flat plate EMFC actuator for salt water flow (from [2]).

3.2 Power Consumption and Packaging

For EFC systems, power consumption and packaging are relatively simple issues. Glow discharges require high voltage, but they are generally low power phenomena. Dielectric barrier discharges (DBDs) also require high voltage, but the low operating current again leads to low power consumption. Corke and Post report a power level of approximately 6.5 to 130 W per spanwise linear meter for DBD actuators [56]. Figure 3.3 shows the ease at which these DBD actuators can be placed onto a surface as long as the material they are embedded in is dielectric [3]. Since the actuators are thin in the streamwise direction, the power requirement is anywhere between several hundred watts and a few kilowatts per square meter of a hypothetical control surface built from placing them into rows. In the figure, the separation between DBD strips is 1.0 cm, and the RF signal input is 4.5 kV RMS at a frequency of 3.3 kHz. At these conditions, a flow speed of 6 m/s is induced at the edge of the panel. The thrust from these DBD arrangements rises with dissipated power [57]. Assuming the induced flow speed for flight-ready control surface actuators will need to be higher

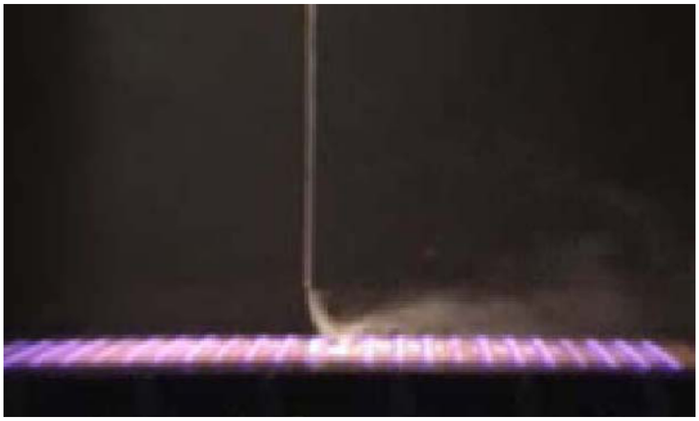

Figure 3.3. Smoke visualization of a DBD control surface composed of rows of actuators creating an electrostatic force that acts from left to right (from [3]).

than a few meters per second, they will eventually have significantly higher power consumption than what was reported in Ref. [56].

Since glow discharge and DBD systems often use these thin sets of electrodes, packaging into control surfaces is also straightforward. The largest components of these systems may indeed be the high voltage circuit elements. As Jayaraman et al. discuss, increased interest in low Reynolds number aerodynamic control for micro air vehicles (MAVs) has brought the use of DBDs into consideration [58]. Although current computational and experimental research appears promising, scaling down to smaller, low-speed vehicles that fit into the useful design space for these actuators may pose a problem due to the mass and volume of high voltage circuit components. Studies on the integration of these components to small scale aircraft appear limited and it is recommended that future research efforts cover this topic.

Concerning EMFC systems, the packaging issue is more complex and dependent not only on the power requirement but the choice of magnets. Figure 3.4 shows a large electromagnet surrounding a hypersonic test section. As used in Ref. [4], it generated a magnetic field of 0.9 T. Although electromagnets used for experimental

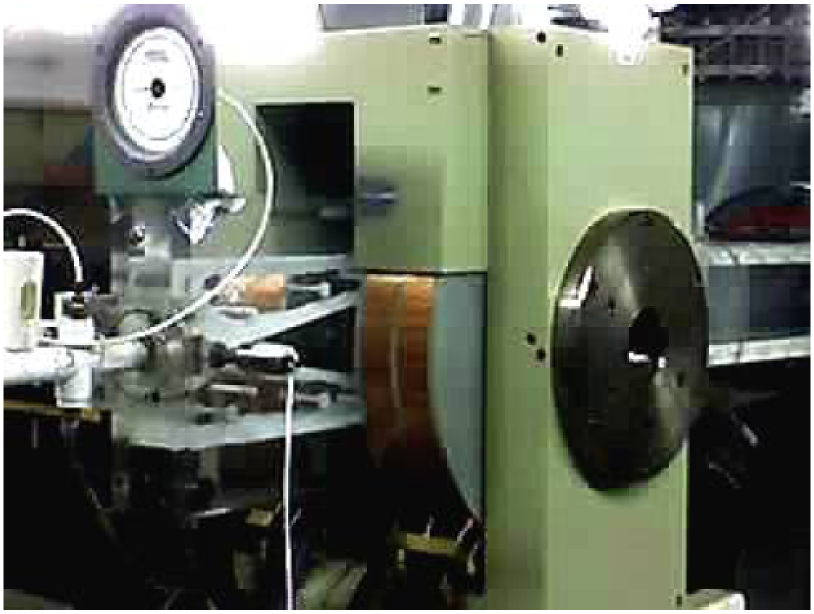

Figure 3.4. A water-cooled electromagnet surrounds an EMFC free jet test section (from [4]).

channel flow EMFC are useful in that they can provide a steady magnetic field inside the test section (whereas a field from NdFeB magnets will vary as shown in Fig. 2.2), their ability to be integrated into flight vehicles is questionable due to their mass and weight. The use of superconducting magnets only exacerbates the problem. The use of rare earth magnets will lead to the most compact EMFC actuator that may be placed on the surface of a wing or at the beginning of an inlet compression system. Clearly, the drawback of efficient packaging with embedded magnets is the relative reduction in magnetic field strength across the control surface. However, going back to the discussion of the interaction parameters, if the actuator performance is not wholly dependent on B, a reduction in B is easier to offset with one of the other variables.

Assuming EMFC surfaces themselves can be made compact enough for flight, there is still a problem with the possibility that the Lorentz force power requirements will exceed the output of a reasonable on-board generator. As discussed, ionization systems may also require a separate power supply. Lorentz force power requirement estimates similar to the one presented above for DBD actuators is still relatively unknown. The pressure increase of 17–20% in Ref. [40] was created with about 2 kW of power where the electrodes enclosed a volume of approximately 40 cm^3. This figure does not appear unreasonably high as many aerospace systems currently require power of that scale. The power supply requirements are also heavily based upon the time of use of the actuator. If the purpose is long-term drag reduction or lift enhancement, an innovative generator is probably required. Perhaps a short duration missile (with EMFC actuators for final, rapid course corrections) can operate based off a thermal battery typical of current technology. The fact that many other potential sources (MEMS microturbine generators, fuel cells, flywheels, capacitors, etc.) of compact on-board power supplies are under development is encouraging [59].

3.3 Selection of EMFC Magnets

Concerning the viability of electromagnetic flow control, an inquiry must be made to understand exactly what range of magnetic surface field values is needed. This inquiry leads back to the reason why magnets are needed for EMFC in the first place, namely, that the cross product of magnetic field and the electric field produces the Lorentz force. The presence of a magnetic field acts as a facilitator for energy addition into the fluid flow from the electrodes. The energy addition is then split into Joule heating and the kinetic energy (rate of work done by the Lorentz force) of the fluid. The selection of appropriate magnets for electromagnetic flow control systems is a current topic of debate. As was mentioned previously, many recent experimental EMFC facilities have used powerful electromagnets capable of surrounding a test section since it is a straightforward way to increase the magnetic interaction parameter. However, some of these electromagnets and superconducting magnets have masses up to hundreds of kilograms (e.g., Ref. [48]) which will make flight applications problematic.

The advancements in several new rare earth magnetic alloys between 1970 and 2000 [60] has made permanent magnets a competitive choice for aerospace applications of magnetohydrodynamics. Preliminary demonstrations of their capabilities have been seen in several publications [2, 24, 34, 41, 49]. Permanent magnets, where possible, should be considered instead of electromagnets since they consume no power and demonstrate much higher values of energy density making their strength-to-weight ratio relatively superior. Unfortunately, one major drawback of using permanent magnets for aerospace applications is the fact that high temperatures drastically weaken their overall surface field strength, which is already low when compared to electromagnets. Permanent magnets lose their magnetic properties at a specified point called the Curie temperature. Prior to that point there is another temperature called the maximum operating point, after which a magnet will experience permanent losses to its original strength [61]. For AJAX-style scramjet engines, it is unlikely that permanent magnets could be used in the high temperature environments even with complex active cooling systems.

Figure 3.5 shows the maximum operational temperatures of samarium-cobalt and neodymium magnets charted along with typical post-shock temperature curves as a function of Mach number for different wedge angles with an incoming stream at 220 K. Neodymium magnets are operationally limited to temperatures just over 400 K, while some samarium-cobalt alloys can be used at temperatures exceeding 800 K. While these temperatures are still far below the requirements of implementation into, for instance, a multi-shock scramjet inlet, these magnets could be used for slender control surfaces to some extent on supersonic and hypersonic vehicles. Moreover, while it would appear that samarium-cobalt alloys are superior to neodymium for high-speed aerodynamic control because of the higher operating point, Fig. 3.6 shows that the high-temperature alloys typically have less overall magnetic field strength [5]. Note that the magnetic flux density is measured using teslas, but the values from Fig. 3.6 are not representative of the maximum magnetic field (also measured in teslas) that will be present on the surface of the magnets. Neodymium and samarium-cobalt magnets are widely available, but they rarely demonstrate maximum surface fields over 0.5 T. Figure 3.7 shows that it is common for permanent magnets to lose the bulk of their surface field before reaching their maximum operational temperatures [6]. Typically, these magnets will see a slight linear decline in surface field for a limited temperature range before reaching a point of rapid decline extending to the maximum service temperature. One of the focal points of current research in magnet development has been to broaden the temperature range in which only a slight linear decline is present, with significant improvements made to samarium-cobalt alloys [62]–[65] and apparently much less work carried out with neodymium alloys. As far as the surface field is concerned, one can conclude that neodymium magnets are the better choice for applications with temperatures ranging up to 350 K. However, the typical decline of the neodymium surface field strength as shown in Fig. 3.7 indicates that samarium-cobalt magnets are more advantageous for higher temperatures. It appears that many, if not all, high-speed aerodynamic control concepts involving permanent magnets will require active cooling. This need for active cooling is not solely associated with the use of rare earth magnets. As exemplified by Fig. 3.4, some electromagnets also require cooling just to operate.

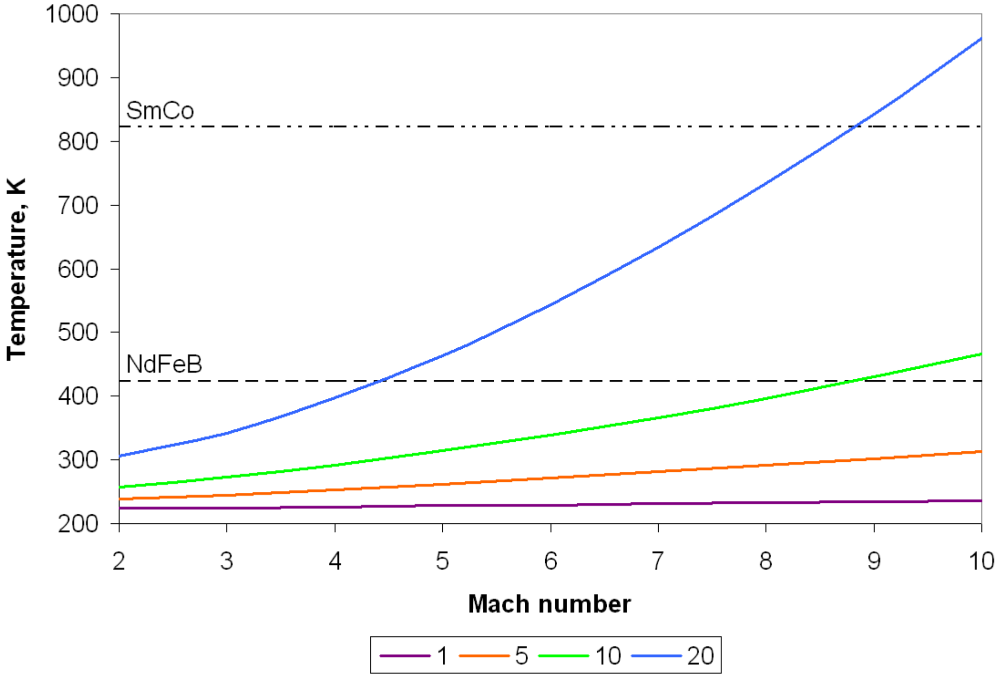

Figure 3.5. Temperature versus Mach number for lines of constant wedge angle (1°, 5°, 10°, 20°) after an oblique shock wave (based on an initial temperature of 220 K) along with Neodymium and Samarium-Cobalt maximum operating temperatures.

3.4 Conductivity

In 1968, Garrison stated that the performance of MHD accelerators depends directly upon the magnitude of the electrical conductivity of the seeded working gas [66]. This statement remains true for aerodynamic control, only with more emphasis placed on improving low-temperature, weakly ionized gases. Before then, the concept of propulsion using electric and magnetic fields had appeared in the literature for several decades. Jahn presented a short review of early literature in electric propulsion [67]. Efforts at experimentation began in the late 1950's beginning with the implementation of plasma jets for propulsion systems [68]. Plasma jets were certainly capable of generating highly conductive gases through thermal ionization, but the temperature and power requirements were too high for viable aerospace applications

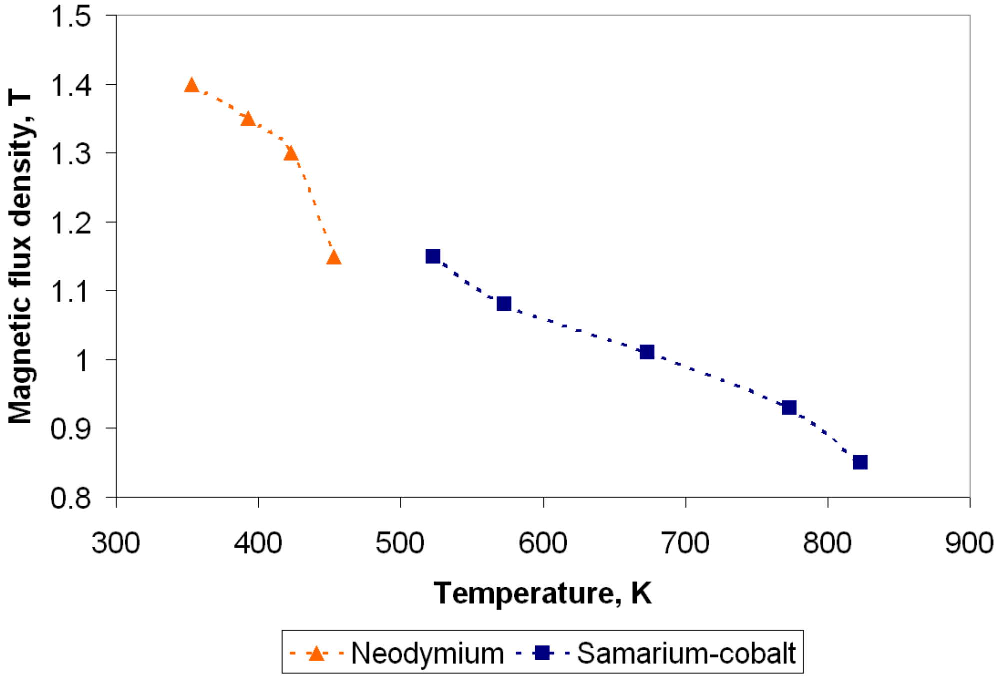

Figure 3.6. Magnetic flux density charted as a function of the maximum operating temperature for several Neodymium and Samarium-Cobalt alloys [5].

at the time. Alkali salt seeding was introduced into the plasma jet in order to achieve the same level of conductivity at a considerably lower temperature [15]. Extensive experimentation with different low ionization energy seed materials (potassium and cesium) with air or noble gases (argon and helium) appeared in the literature through the end of the 1960's [69]–[77]. Generating a bulk flow conductivity on the order of 1000 ℧/m was achievable. The experimental gas pressures reported were usually on the order of one atmosphere. At higher pressures around 10 atmospheres, electron attachment by positive oxygen ions significantly reduces σ [78].

Like many other fields, research in magnetohydrodynamics was affected by the direction of the Apollo program. It appears that engineers may have assumed that megawatts of power produced by an on-board nuclear reactor would be available for future MHD accelerator-based propulsion systems, but the nuclear prospect never

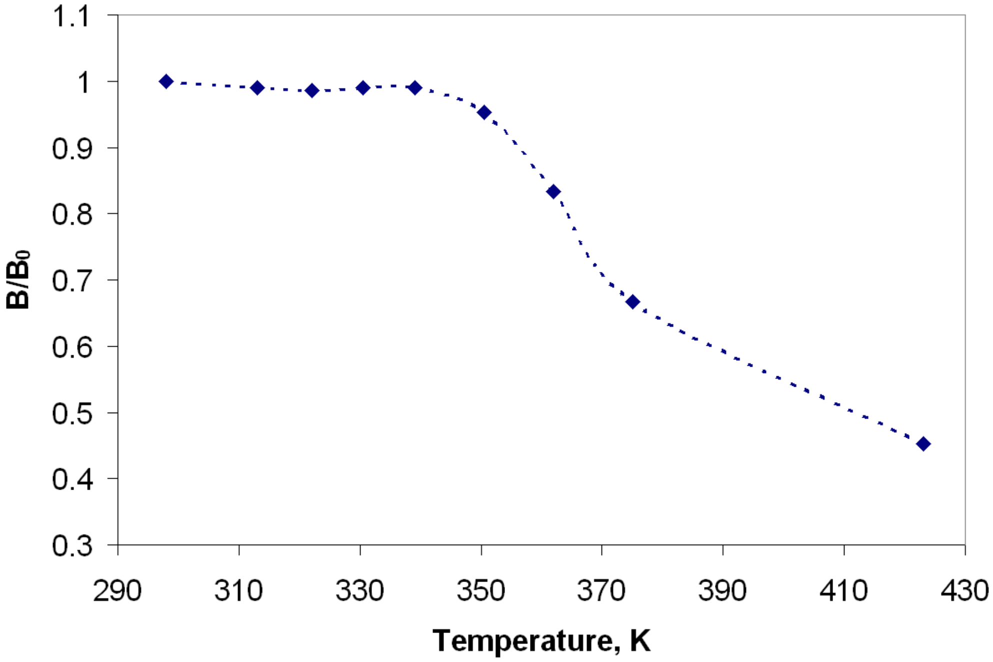

Figure 3.7. A typical plot of the surface field decline versus temperature for a Neodymium magnet with a maximum operating temperature of 423 K [6].

materialized with the exception of the Project Pluto engine testing program [79]. Although nuclear-powered ramjet ground demonstrators were built and successfully tested during Project Pluto, the environmental concerns outweighed their strategic advantage. Additionally, the success of controlled ablation reduced the need for further research into electromagnetic flow control for use on re-entry capsules [80]. Arc jets were then applied to ground testing systems with many integrated into wind tunnels as a source of high enthalpy, high velocity flow [18]. Seeding is still a viable method for increasing the performance of those wind tunnels, but it can lead to undesirable contamination of the flow. Simmons et al. concluded that discrepancies in the air chemistry caused by seeded MHD accelerator concepts for the MARIAH hypersonic wind tunnel made non-MHD options more appealing [81]. The lack of post-Apollo funding and interest in on-board nuclear power effectively halted the prospects of MHD systems for aerospace vehicles. Non-nuclear power generation became the new focus of MHD research [82, 83]. Despite the fact that electric propulsion engines make use of a comparatively weaker force, concepts [84] developed simultaneously with those of MHD propulsion and eventually flourished with help of a low power requirement capable of matching with radioisotope thermoelectric generator technology then emerging [85].

The past decade has certainly seen a reemergence of MHD research applied to aerodynamics. The history above shows that generating and controlling a flow with $\sigma > 100$ ℧/m is difficult because of the power requirements. Creating ionization from a thermal source such as a plasma jet is not desirable, and is not possible for aerodynamic control surfaces. Fortunately, ionization can also be achieved through high voltage fields, laser beams, microwaves, and radiation (any method of transferring energy to cause molecular excitation of the gas). Of the EMFC facilities mentioned thus far, all have at minimum employed high voltage fields. However, a difference exists between each on how the high voltage fields are applied.

The easiest method of creating plasma is to apply an electric field with a large potential difference between two electrodes. Based on factors like separation distance, potential difference, geometry, and the gap medium, plasma will develop between the electrodes. The current is based on the effective resistance of the gap. When plasma fills the gap, the resistance is immediately and significantly lowered. Normally, the end result is an arc discharge where the gap becomes a short circuit and draws maximum power from the potential source. Because of their difficulty to control and destructive nature, arc discharges are most often seen as detrimental for engineering applications. Thus for aerodynamic control, ionization with electric fields has focused on producing discharges of a more diffuse nature, known as glow or corona discharges. However, Zaidi et al. have in fact used a plasma column control concept operating in a constant current, variable voltage mode [47]. The power supply potential was 20 kVDC, and the maximum current was 1.0 A. Fixing the current and activating the power supply causes a high voltage field to be applied until electrical breakdown occurs and a plasma column forms. Once the column forms, the voltage required to maintain the set point current can be very low. When a plasma column forms between the path of least resistance where the tapered electrodes are closest to each other, it travels downstream where the gap between the electrodes gradually increases, visually similar to a Jacob's ladder. The boundary layer control is provided by the momentum transfer from the plasma column propagating downstream.

During the wind tunnel experiments, the plasma column that forms between the electrodes was found to be periodic with a frequency of 1–10 kHz depending on the current and magnetic field strength [86]. While applying a 1.7 kV field at 35 mA with no magnetic field, the plasma column travels downstream at 360 m/s. When a magnetic field of $B = 2.0$ T is applied, the column speed increased to 2000 m/s [87] to generate the control results previously discussed. Thus the electric and magnetic fields combine to allow for greater momentum addition to the flow. It appears that the performance of this facility can be increased simply by raising the set point current. Unfortunately, Joule heating has worked against the plasma column in the case of moving a shock wave induced separation bubble downstream and will begin to suppress results while current is increased beyond a certain point [48]. To conduct further studies with higher plasma column power, an assembly consisting of a sapphire base plate and high temperature arc corrosion-resistant electrodes was constructed [87].

The DC ionization system first presented by Shang et al. in 2002 was part of an EMFC actuator designed to affect the shock wave structure around a blunt body [50]. A diffuse WIG is created instead of a plasma column due to a lower applied potential difference and a lower static pressure. The blunt body study was followed by a flat plate model constructed of a ceramic base and two embedded copper electrodes [51]. Figure 3.8 shows these electrodes, with the upstream cathode experiencing a more intense glow [7]. This diffuse glow discharge begins to constrict and transition to an arc when the current surpasses 100 mA or when B is greater than 0.2 T [51]. In addition to using only a DC discharge, pulsing the discharge with a frequency between 5 Hz and 10 kHz was also used to explore the response of the Mach 5 flow to plasma actuation with a magnetic field present [88]. Volumetric heating of the air by the plasma was found to occur faster than the 3 ms response time of the pitot probe. In another case, RF radiation was added to augment the ionization created by the DC glow discharge, resulting in a reduction in the impedance across the electrode gap [49]. Accounting for all of the ionization methods, the maximum power requirement remained a few kilowatts or less and can result in a conductivity of a few ℧/m in the static pressure environment of 0.6–7 torr.

The research presented in the various publications for this facility certainly shows that a low temperature WIG created by a DC discharge ionization system allows for energy addition in the boundary layer of high-speed air flow. As a result, the energy addition allows for an EMFC actuator to significantly affect the surface pressure distribution. Direct current discharges do not easily remain diffuse as pressure rises [89], but this system should be operational for high-altitude flight conditions.

Research has shown that the degree of ionization produced by an electric field may be higher for pulsed discharges rather than for a steady DC discharge of similar potential difference. Discharges with periodic high voltage pulses simply can withstand a higher applied electric field before a transition to arcing occurs, so long as they are sufficiently short enough to sustain streamers before transitioning to sparks [90]. This property allows more power to be transmitted during the pulse, which will

Figure 3.8. A DC voltage discharge between two electrodes at freestream conditions of M = 5.15 and $p = 0.59$ torr. The applied voltage is 880–920 V at a current of 50 mA. The addition of a magnetic field significantly affects the plasma and creates a virtual hypersonic leading edge strake (from [7]).

increase σ. Very short duration, low duty cycle pulses can maintain a conductive path between electrodes as long as the frequency is additionally high enough to counteract the WIG decay. However, the applied Lorentz force should be continuous and therefore generated with a DC power supply. Palm et al. [24] addressed these issues by creating an EMFC channel flow facility with RF WIG generation and simultaneous DC Lorentz force application using the electrode configuration previously discussed. The facility generated a diffuse WIG for Mach 2–4 flow originally by using a 13.56 MHz, 600 watt RF power supply to create the conductive path for the Lorentz force energy addition [41]. Conductivity (0.1–1 ℧/m) scales with the power draw of the system. Since that time, a more complex ionization system has been constructed to raise the attainable level of conductivity without raising the power draw. Meyer et al. first reported using this system to attain $\sigma \approx 0.1$ ℧/m in a Mach 4 flow by compressing a 500 V, 1 μs pulse into a high frequency (up to 50 kHz), high peak voltage (20 kV), short duration pulse (10–20 ns) [40]. During the peak voltage application, the current may reach 100 amperes, but the short duty cycle results in a reasonable overall power consumption of, for instance, 40–80 watts in Ref. [40]. The ionization power requirement is therefore much less than what is used to apply the Lorentz force. According to Nishihara et al. [45], raising the frequency of the system from 40 kHz to 50 kHz increases the flow conductivity along with lowering the ballast resistance. The frequencies in this range match reasonably well with the WIG decay and provide fairly steady flow conductivity.

The life of the WIG can be observed by measuring the current draw from the DC Lorentz force power supply. Figure 3.9 shows four pulses measured from the ionization system operating at 40 kHz. Figure 3.10 shows two current oscillograms measured from the DC Lorentz force circuit for the same conditions as Fig. 3.9, created with constant electrode potentials of 2 kV (one at each polarity). The current rises at the initiation of each ionization pulse, and then falls with the WIG decay. With slightly different test section conditions, a current oscillogram appears in Ref. [46] for an ionization frequency of 100 kHz, which results in a more constant Lorentz force over time because the WIG decays less. As one can see from Fig. 3.10, the Lorentz force system has an average power consumption of about 2 kW and it is capable of creating the pressure changes shown in Fig. 3.1.

3.5 Overall Feasibility

A few examples of recent EMFC facilities have been presented in this section. These facilities have emphasized the use of electromagnetic forces within the boundary layer and they have shown that EMFC can have a considerable effect at supersonic and hypersonic flow speeds. However, the pressures at which these experiments have been conducted, as well as the magnitudes of σ and B, are far below what may be necessary for a hypothetical AJAX scramjet engine. Consequently, these systems are

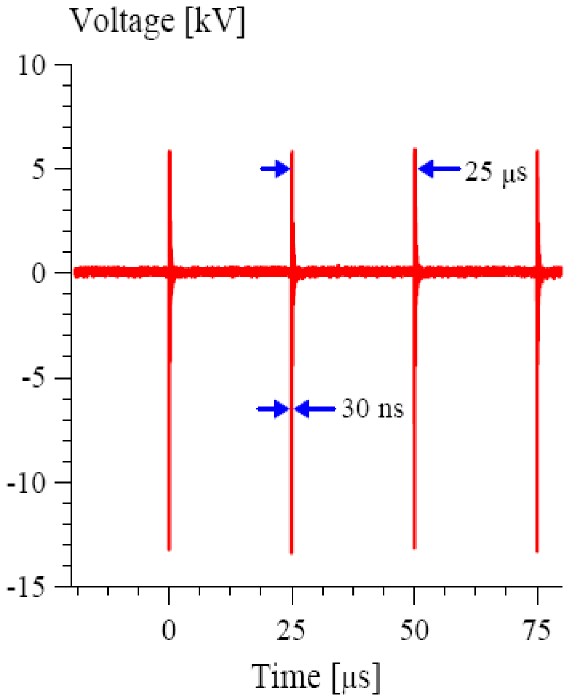

Figure 3.9. Voltage oscillogram for 40 kHz pulsed ionization of a Mach 3 nitrogen flow. The test section pressure is 8.4 torr and $B = 1.5$ T (from [8]).

more applicable for boundary-layer control of an aerodynamic surface or inlet system. Several steps must be taken to transition to a feasible electromagnetic virtual control surface. Experimental facilities have demonstrated success using low pressure core flows often surrounded by large magnets, and it is time to consider more compact configurations that can simulate environments like external flow over a wing or the beginning of an inlet compression system. In these environments, the magnets can be embedded below the surface and between the electrodes. Novel cooling methods must be developed for permanent magnets to survive the high-temperature environment. EMFC actuators may be placed in regions where the surface is actively cooled or is relatively cool. Considering the maximum operating temperature of rare earth magnets, cooling to a temperature as low as 350 K may be necessary. Test section pressures must be increased, not necessarily to atmospheric, but perhaps to simulate

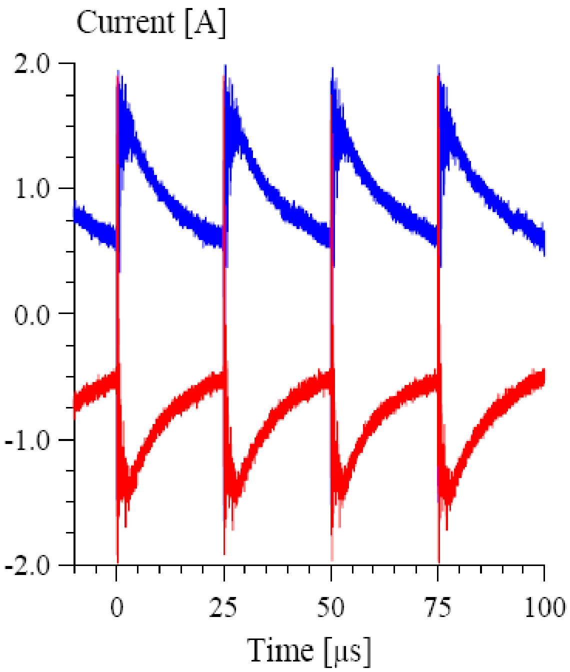

Figure 3.10. Current oscillogram for Lorentz force power supply with the test conditions of Fig. 3.9 and different 2 kV electrode polarities (from [8]).

the pressure after a shock over a thin wedge. The Mach 5 EMFC facility test section pressure reported by Shang et al. is meant to simulate an altitude from 30–50 km (0.6–7 torr) [49], but accounting for a real flight vehicle with a leading shock leads to much higher pressures in that altitude range (i.e., a 10° wedge at that speed would lead to a static pressure of 2–20 torr).

Although it appears challenging, experimental generation of a Lorentz body force is not particularly difficult for EMFC actuators. The key problem is creating non-thermal ionization to supply a conductive working fluid for the actuator [35]. Under rarefied conditions, DC ionization systems are capable of creating a diffuse WIG for which σ can reach a few $\mho$/m at high speeds. As pressure rises, the voltage required to sustain a glow discharge rises. This relationship makes arcing with DC discharges more probable for EMFC as charge builds up on the electrodes. High voltage, high-frequency pulsed ionization sources are another available method for creating the same value of conductivity. These discharges with high energy transfer during low duty cycle pulses can be applied in systems to produce non-thermal ionization, and σ is sustained by using a frequency fast enough to counteract the WIG decay. Ionization sources for EMFC actuators should trend towards using RF or square wave signals, as long as the packaging of the pulsing circuit elements does not lead to size and weight requirements much greater than a DC system. Fridman et al. postulated that voltage pulse durations less than 100 ns/cm of anode and cathode separation can sustain streamers without transformation into arcs [90]. Refining that estimate and determining the plasma decay rate between pulses will allow for the optimization of the ionization source and will minimize fluctuations to the flow conductivity. The constant development of power semiconductors should make high-frequency pulsing systems smaller and more cost effective. Separate ionization and Lorentz force power supplies can be combined over the same flat plate electrodes with the use of rectifiers or diodes. The largest difference in pressure is obtained when the Lorentz force and Joule heating effectively work together. Since Joule heating thickens the boundary layer and decreases the local speed of sound, a Lorentz force applied to retard the freestream flow or direct it off of the surface has the greatest effect.

With these issues properly addressed, EMFC could potentially be used in place of traditional control surfaces at high altitudes. It should not be questioned if the Lorentz force is powerful enough to provide high-speed aerodynamic control. The main issue is the determination of whether or not the ionization and Lorentz force power requirements of an actuator result in a system compact enough to be implemented into a flight vehicle. Table 3.1 provides a summary of literature in this section with experimental environments highlighted.

Table 3.1. EMFC experimental environment summary

Ref.	Mach num.	σ, $\mho$/m	p, torr	B, T	Magnet type	Ionization source	Medium	Configuration
[34]	low-speed	3.2	1300	≈ 0.4	NdFeB	N/A	salt water	flat plate
[50]	5.8	1–2.5	1.2–2	0–2	electromagnet	High voltage DC	air	blunt body
[41]	4	≈ 0.01	6–8	≈ 0.4	NdFeB	High voltage RF	He,N_2	channel
[24]	4	0.05–0.1	2–10	0.45	NdFeB	High voltage RF	He	channel
[43]	3	0.02–0.12	12–15	0–1.5	electromagnet	High voltage RF	N_2	channel
[2]	low-speed	≈ 3	760	≈ 0.4	NdFeB	N/A	salt water	flat plate
[44]	3,4	0.08–0.18	7–20	0–1.75	electromagnet	High voltage RF	N_2,air	channel
[4]	5.1	≈ 1	0.6	0.1–0.2	electromagnet	High voltage DC	air	flat plate
[45]	3,4	0.14–0.23	7–20	0–1.5	electromagnet	High voltage RF	N_2,air	channel
[88]	5.1	≈ 1	0.8	0.2	electromagnet	HV, 10 Hz–RF	air	flat plate
[49]	5	2	0.6–7	0–1	em, NdFeB	HV DC, RF rad.	air	flat plate
[33]	3	≈ 0.1	7–20	0–1.5	electromagnet	High voltage RF	N_2,He	channel
[39]	3	≈ 0.07	7–20	0–1.5	electromagnet	High voltage RF	N_2,He,air	channel
[1]	3	≈ 0.1	7–20	0–1.5	electromagnet	High voltage RF	N_2,air	channel
[47]	2.8	N/A	28	0–2	superconducting	plasma column	air	channel
[8]	3	≈ 0.1	7–20	0–1.5	electromagnet	HV RF,seeding	N_2,air	channel
[51]	5.3	0.06	≈ 0.6	0–1	electromagnet	High voltage DC	air	flat plate
[40]	3	≈ 0.1	7–20	0–1.5	electromagnet	High voltage RF	N_2,air	channel
[86, 87]	2.8	N/A	28	0–4.5	superconducting	plasma column	air	wedge
[46]	4	≈ 0.1	4.8	0–1.63	electromagnet	High voltage RF	N_2	channel
[48]	2.6	N/A	28	0–4.5	superconducting	plasma column	air	wedge
[7]	5.15	≈ 1	0.6	0–0.2	electromagnet	High voltage DC	air	flat pl., inlet

CHAPTER 4

ELECTRIC FIELD CONTROL AND REVIEW CONCLUSIONS

4.1 Flow Control by Glow Discharge

Although much of the previous discussion has been dedicated to flow control by electromagnetic fields, it must be noted that considerable interest for flow control with only plasma or electric fields has developed. Techniques for aerodynamic flow control by electric fields can be categorized into glow discharges and dielectric barrier discharges, covered in the next two sections, respectively. A glow discharge is formed across a gap of air or another gas between two electrodes with a difference in electric potential. The presence of a glow discharge is based on factors such as electrode geometry, ambient pressure, the gap medium, and the voltage. The glow discharge essentially means that the gap is filled with free radicals and electrons traveling between the electrodes. As such, the current increases rapidly after initial formation. Increasing the voltage after the glow discharge is formed eventually leads to electrical breakdown and arcing. A diffuse discharge is desirable since it indicates that the WIG effects will be uniform throughout the glow region. Often, experimentation with this phenomenon has occurred in low pressure environments where it is easier to create a diffuse discharge with a relatively low voltage. High pressure glows are also possible, and applying the potential difference with an increasing frequency has shown that the same current is maintained with a lower voltage [91].

Bletzinger et al. have provided a review of plasmas related to high-speed aerodynamics, containing a short history of the development of experimentation with glow discharges in recent decades [92]. In summary, initial shock tube experiments were conducted by measuring the drag and shock wave structure of objects (often blunt) while recording the differences with and without the actuation of a plasma source. As shown in Fig. 4.1, plasma flow as opposed to typical flow can drastically change the standoff distance of a bow shock around a blunt body [9]. Similar results were demonstrated as early as 1959 by Ziemer [93]. The change in shock wave geometry is important because a change in standoff distance can reduce heating and drag. Furthermore, the properties of a glow discharge may be used to improve the off-design performance of a high-speed inlet compression system by manipulating the shock wave structure. These features of glow discharges are significant for the future development of re-entry vehicles and hypersonic airbreathing propulsion. Although some of the early shock tube literature makes a case for electrohydrodynamic effects as the reason behind some of the shock wave alteration [94]–[96], the general consensus is that most of the effects seen are a product of the heating from the plasma [92]. Computational studies also indicate this result [97].

If the bulk of the glow discharge control effect is from heating, then the next logical step in the process of estimating its feasibility is to determine if there are benefits of plasma as opposed to other heating sources. One benefit of heating by glow discharges when compared to a typical heating element is rapid actuation. This may be a large enough benefit to continue experimentation with surface glow discharges for aerodynamic control. For instance, Shin et al. measured a glow discharge actuation time of less than 220 μs using pin electrodes on a flat plate in a Mach 2.85 flow environment [98]. This flat plate plasma actuator is capable of creating a weak shock wave over the actuator when the plasma is diffuse. A more constricted plasma formation in that environment, although produced with higher power, does not have the same shock wave control effect. The difference between plasma heating and surface

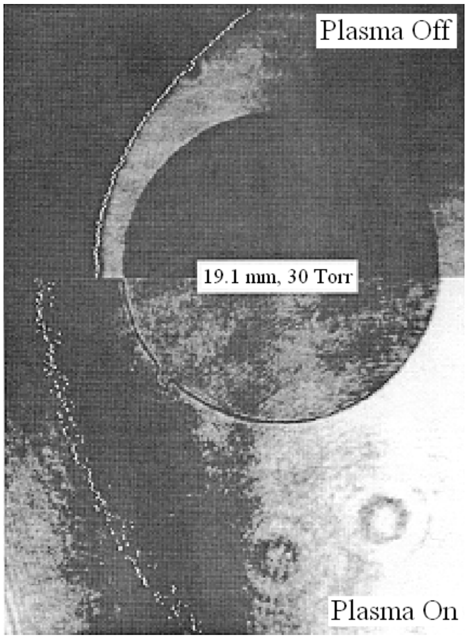

Figure 4.1. Split image of a bow shock around a sphere with and without plasma for a flow velocity on the order of 1600 m/s (from [9]).

resistance heating is noticeable, whereby the plasma has more of a volumetric effect and is not exclusively characterized as typical surface heating [99].

Flat plate experimentation with glow discharge plasma actuators for aerodynamic control has yielded promising results. Experimental results from Ref. [99] show the plasma and surface heater both cause a 50% change in pitot pressure in Mach 5 flow over the cathode, with the glow discharge heater acting an order of magnitude faster. As was previously mentioned, the EMFC actuator in Ref. [4] produced an 18% change in lift while using only a DC glow discharge. Many other studies show similar results. Although efficiency improvements have been made, the performance of these plasma control systems is still uncertain across wide ranges of flight speeds and vehicle configurations [92]. If indeed the plasma effect is thermal and increases the local speed of sound, than it can intuitively be expected that the effect will be lessened as speeds increase and the post-shock air temperature and enthalpy increase. Hence, a flat plate actuator immersed in a low temperature wind tunnel flow is a best case scenario for demonstrating glow discharge control. The power of the plasma source can be raised in order to compensate for a flow of higher enthalpy, but the efficiency of control may be drastically reduced. Experimental studies using plasma discharges with wedges and blunt bodies are discussed next to elaborate on this issue.

Although the presence of plasma can change the structure of a shock wave, it appears that most literature involving inlet compression systems also contains magnetic fields for the full Lorentz force effect. A detailed literature review appears in Ref. [92]. Some research with only plasma has been reported. For a Mach number of two and a flow mixture of nitrogen and helium, a glow discharge yielded a significant change in the oblique shock angle over a wedge [100]. The change in the shock angle indicates a change in the Mach number from 2 to 1.8 due to the plasma heating. The WIG source was located on the walls of the wind tunnel. Since the initial ramps of an inlet compression system are often not surrounded by an outer wall (e.g., X-43A design), it would be beneficial to test if this effect could be duplicated with a WIG source located entirely on the surface of the wedge. Placing a diffuse plasma source on the tip of a wedge and creating an effect on the oblique shock angle is a logical direction to move in to determine if these systems can be placed on a vehicle. Such a design was recently attempted by Gnemmi et al., where plasma discharges on a conical tip of a projectile were used to disturb a shock wave at freestream conditions of Mach 4.57 and 54 kPa static pressure [101]. More research is needed to determine if such systems can produce an appreciable aerodynamic control force, but it appears that ramp and inlet concepts of low to moderate turning angles are just as viable as flat plate concepts. Closely related to that design is the concept of a virtual cowl that can be created by plasma heating [102, 103]. The plasma source is more likely to be high-energy electron beams or microwaves rather than glow discharges. The heat addition specifically can alter the upstream flowfield in order to reduce the inlet spillage. This concept will require a considerable amount of power to operate, but one must consider that any system with plasma heating may be used only during a (presumably short) transition process by acceleration to the design Mach number. Although most of these system designs are analytical models, some preliminary experimental studies have demonstrated the concept [104].

Concerning blunt bodies, many studies focusing on drag reduction have appeared in the literature. One initial study showed that the drag coefficient for a sphere in the presence of a WIG was significantly reduced for subsonic flow [105]. The same experiment for supersonic speeds showed that the drag coefficient was higher using a WIG than with typical airflow, attributed to an increase in the pressure integral on the front of the model at certain conditions. Other plasma sources constructed for drag reduction have proven to be more effective since then. Ganiev et al. reported a reduction in the drag coefficient of about 50 percent from Mach 0.59–4 using a plasma jet placed at the tip of a somewhat blunt body [106]. The reduction in the drag coefficient was found to depend on the stagnation temperature of the counterflow jet. Plasma jets appear to be inefficient for streamlined shapes [107]. At the time of Ref. [106], other publications also described drag reduction with plasma jets and other forms of focused energy addition. A thorough list of these can be found in Ref. [108]. However, the large drag reduction by the plasma jet injection appears to be more directly related to the counterflow jet instead of the thermal effects of the plasma. Fomin et al. experimentally determined that fluid dynamics instead of plasma is the dominant effect using the jet for moderate supersonic Mach numbers [109]. Those experiments were conducted using a truncated cone cylinder at Mach 2, 2.5, and 4. As was discussed, the use of plasma jets was eventually deemed unrealistic for MHD flight applications in the 1960's because of the power requirement.

Many of these current systems have been met with enthusiasm, but again scaling the power requirements to flight vehicles or missiles may pose insurmountable problems with current technology. Although new publications continue to emerge with different plasma sources and test geometries, very little of it is predominantly different from what was carried out at the beginning of this decade.

Concerning the use of plasma flow control systems as part of realizable flight vehicles, some appear more feasible than others. In order to overcome problems including but not limited to power consumption, scaling, and hypersonic interaction at true flight conditions, the next step for plasma control for aerodynamics is a transition into realistic systems. It is understandable that some of the models of full-scale hypersonic systems have not been constructed due to the cost, but plasma control needs to be better proven experimentally as part of more flight-ready systems instead of basic shapes. Manipulating the bow shock wave around blunt bodies with plasma has been experimented with for fifty years, but no concrete applications are yet practical. It appears that ground testing of aerodynamic surfaces and inlet systems is moving forward, with the rapid plasma heating effect showing promise for control applications. The main challenge is producing systems that make use of current technology while maintaining power and packaging considerations.

4.2 Flow Control by Dielectric Barrier Discharge

Considering the physics involved, a dielectric barrier discharge is similar to a glow discharge. Where a glow discharge has an air gap, a DBD contains a gap of dielectric material between the anode and cathode. Typical materials like glass, polymers, and ceramics have a much higher resistivity than air, allowing for the electrodes to be placed closer to one another. Closer placement increases the electric field around the electrodes and ultimately raises the Coulomb force in Eq. (2.10) without the occurrence of electrical breakdown. The dielectric barrier is self-limiting as it prevents charge accumulation over the barrier material to prevent arcing. DBDs have been recognized since the mid-19th century, with the their first application being the production of ozone [110]. Since that time, research has continued to grow and now applications include surface treatment, reduction of pollutants, lasers, and plasma display panels. Systems using glow discharges often use low pressure, but these discharges were stabilized across the barrier at atmospheric pressure beginning in the 1980's [111].

Dielectric barrier discharges constructed specifically for aerodynamic flow control applications appeared in the literature near the end of the 1990's [112, 113]. In the decade since those reports, research into aerodynamic flow control with DBDs has rapidly increased both experimentally and computationally. A number of reviews have been written [56],[114]–[116], which probably indicates a variety of opinions on their applicability. Most conclude the DBD control effect is applicable for low Reynolds number flows below the general aviation range, and improvements to their strength will have to be made for them to be applied to flight aerodynamics. At low speeds, DBD actuators have a significant effect on boundary layer flow. Figure 4.2 shows a notable image by Roth et al. of flow reattachment made possible by an array of DBD actuators [10]. This actuator system works at atmospheric pressure, and has been named the One Atmosphere Uniform Glow Discharge Plasma (OAUGDP$^{\text{TM}}$). The ionization is created with a high voltage RF signal and the barrier material is Kapton. An RF signal is used rather than a DC signal because it creates a cycle of charge exchange between the electrodes that increases the control effect. The waveform shape and frequency along with the dielectric material choice may be optimized to some extent, with many different configurations reported. Several studies with the system in Fig. 4.2 have resulted in successfully increasing or decreasing drag on a flat surface, adding momentum to the boundary layer flow, reducing the boundary layer thickness, and inducing a flow (also known as the ionic wind) of up to 6 m/s [117]. Figure 4.2 raises the immediate question about the ability to apply a dielectric barrier discharge system to high-speed flow where flow reattachment, drag reduction, and turbulence suppression are all major concerns. Although DBD actuators are studied by several institutions, the spanwise electrode geometry is always fairly similar and is depicted in Fig. 4.3 [11]. This linear arrangement also can be modified into an annular jet source (known as a plasma synthetic jet actuator), where pulsed operation can generate vortex rings [118]. The maximum jet velocity for that study was on the order of 1 m/s. The electrodes also may be wrapped around the internal diameter of an axisymmetric jet. Benard et al. demonstrated that this configuration may be used for jet mixing enhancement, where experiments increased mixing in a flow up to 30 m/s on a model with an exhaust diameter of 72.5 mm [119]. No modification was seen at a jet speed of 40 m/s. The self-limiting DBD allowed about 10 watts of power to be transferred into the flow, and it was noted that this value must be increased for the DBD to have more effect on the jet flow.

The relative strength of current systems can be compared by their ability to induce a certain flow speed of air passing over the actuator. The ion wind speed measured in most recent surface DBD actuators is only a few meters per second, and efficient control results are obtained when u_∞ is less than 30 m/s [114]. However, some experiments have been conducted using higher freestream speeds. Opaits et al. [120] investigated DBD control of a NACA 0015 airfoil with freestream speeds of 20 to 75 m/s at atmospheric pressure. The stall angle was raised with the DBD actuators at $u_\infty = 75$ m/s, and a change in pressure distribution was also recorded. Similarly, Roupassov et al. [121] measured changes in the pressure distribution for a NACA 0015 airfoil at speeds up to 110 m/s. In this case, the electrodes were placed parallel

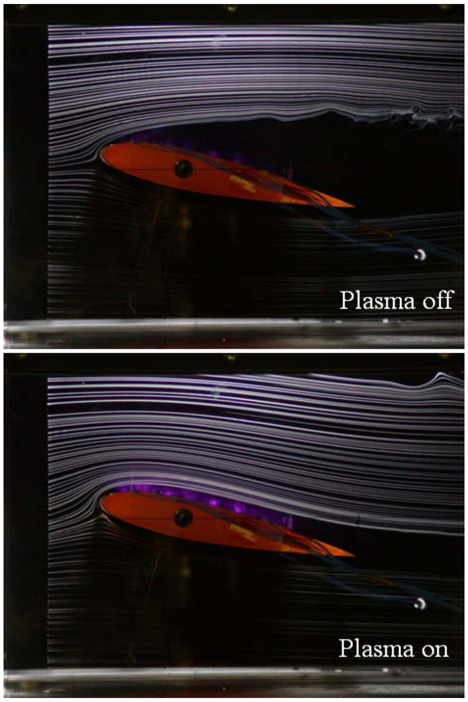

Figure 4.2. Smoke visualization shows flow reattachment on a NACA 0015 airfoil at a 12° angle of attack by an array of EFC actuators. The freestream flow speed is 2.6 m/s (from [10]).

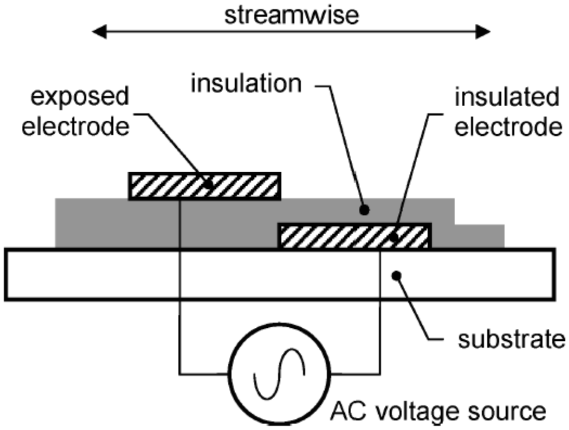

Figure 4.3. Typical spanwise cross section geometry of a dielectric barrier discharge actuator for aerodynamics applications (from [11]).

to the flow, and it appears that the pressure distribution incurs a greater change with the DBD actuator when the airfoil is close it its stall angle. One attempt was made recently to mount a DBD actuator on the leading edge of the wing of a Jantar Standard SZD-48-3 sailplane [122]. It appears that the DBD system was able to affect the separation and lift characteristics of the wing surface, but the data collected was not particularly reliable and refined tests are needed. A study by Corke et al. stated a DBD actuator was able to excite three-dimensional boundary layer instabilities on a sharp cone at Mach 3.5, but no similar results have appeared since [123]. For current DBD actuators, it is clear that a speed of 30 m/s represents the freestream flow limit in which a noticeable control effect is demonstrated. For freestream speeds over 30 m/s, DBD actuators may slightly delay stall, assuming they are placed on the location where the flow will normally begin to separate.

In order to maximize DBD actuator performance for high-speed flow control, one may initially assume that the anode and cathode should have minimal size and be placed as close as possible to each other and separated by a very thin layer of dielectric material. This geometry would maximize the electric field, where the Coulomb force grows with E^2 in Eq. (2.10). However, it has been argued that the force induced from DBD actuators should not be associated simply with E^2 and requires a more detailed analysis [124]. The ion wind is a momentum transfer between neutral particles and heavy ions whose motion is induced by the Coulomb force. Consequently, the electric field is significantly affected from the charge accumulation and particle interaction over the dielectric gap. This interaction dampens the electric field and is known as Debye or electrostatic shielding. Currently, numerical simulations are unable to simulate the observed random microdischarges in time and space that may help to resolve this issue. It does appear that the effectiveness of the exposed electrode is increased when it is thinner [11]. However, the ion wind increases with the width of the insulated electrode until it reaches a limit based on the applied voltage. Perhaps new efforts into geometric optimization or a method of resolving the E field dampening will yield a viable design for freestream flows of higher speeds. An increase in the ion wind speed would no doubt expand the usefulness of DBD actuators for aerodynamics. They may become capable of improving the efficiency of turbine blades as one example [125, 126]. For those studies, DBD actuators were placed on the tip of low speed turbine blades in a linear cascade. The chord Reynolds number was in the range of 10^4–10^5. An actuator placed close to the separation region of the blades was determined to have an effect similar to using tabular vortex generators, where the advantage of the DBD actuators is they are used only when necessary.

The lack of effectiveness of DBD actuators for higher freestream speeds is based more on the low energy input to the air flow rather than a reduction in the output ion wind due to electric field dampening. Going back to the work of Benard et al., axisymmetric jet mixing was achieved with DBD actuators for a Reynolds number limited to about 128,000 [119]. Similarly, axisymmetric jet mixing was obtained with RF frequency plasma actuators acting on a Mach 1.3 flow with a Reynolds number of approximately 1.1 million [127]. The RF frequency plasma actuators added considerably more energy to the flow at a rate of 160 watts where the exit diameter was 25.4 mm. Several options are potentially available to raise the strength of dielectric barrier discharges. First, the potential difference could be raised between the DBD electrodes. Enloe et al. have estimated that the induced velocity increases with $V^{3.5}$ [11], but very high voltage DBD actuators with an ion wind speed over 6–8 m/s still have not been demonstrated. Increasing the voltage ultimately leads to greater instability and possible signal interference if actuators are eventually placed on aircraft. Conceivably, altering the barrier material may lead to a design with higher power input, but doing so may increasingly indicate that high frequency plasma actuators without any barrier material at all are more practical for high-speed flow control. Certainly attempts are being made to limit electrostatic shielding and increase DBD efficiency, but little discussion appears on a concrete methodology behind pursuing this strategy.

Without significant improvements to their overall strength, current DBD actuators are suited only for low Reynolds number aerodynamic control applications. A noticeable increase in work with applying DBD actuators to unmanned air vehicles (UAVs) and even MAVs has occurred in the past few years. One major issue with the development of small aircraft is the design of low Reynolds number airfoils that produce useful lift. Leading edge actuators have been demonstrated experimentally and computationally to increase the flight envelope of some familiar airfoil designs by modifying lift and drag [58, 128, 129]. DBD control for MAVs is advantageous for airfoils with high sweep and angle of attack where the use of conventional flaps and ailerons is either troublesome or completely ineffective. However, the effectiveness of low Reynolds number DBD active flow control actuators is very much dependent on the airfoil leading edge geometry [129]. These actuators are also limited to the low Reynolds number range because they lose their effectiveness in rarefied atmospheric pressure environments normally encountered by high-speed vehicles. Fortunately, a momentum transfer study by Abe at al. has shown that DBD actuator thrust actually increases for a certain pressure range below atmospheric [130]. Until pressure was reduced to about 60 kPa, the performance was greater than or equal to what was recorded for atmospheric pressure conditions. Afterwards, performance dropped as pressure was reduced further and sparks began to develop which damaged the barrier material. This study indicates the actuators should perform well to a flight ceiling of perhaps five kilometers. The power requirement of these UAVs and MAVs appears again to be only on the order of tens of watts or less. The next logical step in the development of these systems is to determine the mass requirements of the actuator circuit. The scalability of the mass and volume requirements of DBD systems must be determined for potential integration into UAVs and MAVs. Although it is well known that DBDs are lightweight and compact enough to be placed on a thin airfoil, the same has not yet been verified for corresponding on-board high voltage transformer and control circuit elements.

4.3 Conclusions and Future Outlook

Flow control with electric or electromagnetic fields is an exciting topic due to its multidisciplinary nature, the possibility to solve difficult high-speed aerodynamics problems, and the overall design challenges. Also, another long-term factor can be added. It has long been theorized that research into new sources of atomic energy will eventually produce an extremely high power, yet compact generator system. The engine tested during Project Pluto shows that a nuclear reactor with 1960's technology was close to being capable of supporting a Lorentz force accelerator with thermal ionization. However, the radiation makes their implementation into a flight vehicle unacceptable. When a major breakthrough eventually happens, these new on-board generators will make all forms of MHD flow control realizable. Lorentz force engines may even someday replace conventional turbojet and ramjet engines. Until that time, an inquiry must be made as to what EFC and EMFC technologies can be supported with on-board power generators with today's technology. Thermal ionization for bulk flows does not appear achievable, leaving the non-thermal WIG sources as the best prospects for creating an appreciable amount of conductivity. Also, the flow speed range in which electromagnetic, glow discharge, and dielectric barrier discharge systems are applicable does not appear to be clearly defined. Electromagnetic actuators are optimal for very high speeds where the flow downstream of the leading shock becomes ionized by itself and the thermal effect of using only plasma is likely to be negligible. This leaves a sizeable subsonic and supersonic gap where none of these concepts have been found to be relatively superior yet.

EMFC actuators can be characterized in more detail with a better use of dimensionless parameters. For MHD accelerators, reaching $I_M \approx 1$ is achievable. For control surfaces, reaching $I_M \approx 1$ requires extremely low pressures and unrealistic magnetic fields. However, reaching that value is not necessary for boundary layer EMFC. The parameter defined as I_{EM} may be more appropriate, not just because it results in a higher value but because it includes the electric field and more accurately depicts the contours of the Lorentz force. The use of one dimensionless number over the other is based on the MHD loading parameter which indicates if one Lorentz force term out of EB and uB^2 is dominant.

Dielectric barrier discharges, because of their geometric simplicity and compact size, seem ideal for high-speed flow control. For years, their applications have been growing and DBDs can be found in most households and offices in plasma display panels. The concept of utilizing DBDs for aerodynamic control has existed for a little more than 10 years. Although this concept is under active research, it appears as though DBDs are limited to affecting freestream flow speeds of less than 30 m/s despite many optimization efforts to improve their strength. Limited control has been seen for speeds over 100 m/s when, for instance, the actuators are located directly where separation begins to occur over an airfoil. Therefore, current DBD actuators do not appear to be robust enough for all but very low speed flight applications. The systems may be integrated into UAVs and other small vehicles to improve the airfoil flight envelope, but it is unclear if there will be a distinct advantage using this particular control concept due to the weight of on-board electrical circuits. The power requirement itself is low enough for small vehicles, but the supporting high voltage pulse equipment may lead to scaling problems. A tradeoff study should be considered for this issue.

While DBDs have generally been researched with atmospheric pressure and low speeds, glow discharge phenomena have operated in low pressure, high-speed environments. As was discussed, the effect of glow discharges is generally thermal, which changes the local Mach number and can affect drag and the shock wave geometry. Although glow discharges have demonstrated several capabilities during subscale ground tests, some of their trends may be troublesome for high-speed flight. For instance, the glow discharge thermal effect will likely be reduced for higher speeds which produce higher aerodynamic heating. However, the rapid actuation ability is desirable and has been experimentally demonstrated to produce a significant change in surface pressure. More emphasis should be placed on surface actuators and inlet systems in an effort to advance from blunt body testing which does not appear to have led to any engineering applications. Counterflow plasma jets do not appear to be practical with thermal ionization. Another area where plasma will make a major impact in aerodynamics is the use of actuators to assist ignition and combustion. Reference [131] provides a thorough experimental review of that field.

It appears that EMFC actuators have considerable potential for further research into high-speed flow control. EMFC systems have one major disadvantage when compared to DBD and glow discharge control in that a separate ionization system is needed to generate conductivity for the Lorentz force to take effect for typical high-speed aerodynamic conditions. However, new methods of creating non-thermal conductivity by high-frequency pulsed discharges, electron beams, microwaves, radiation, and various combinations are promising. Increased research into improving the conductivity seen with these systems and operating with higher pressures is recommended. Also, proof-of-concept testing of these systems will lead to further understanding of their effectiveness for control surface implementation. Magnet selection is another critical issue. Inexpensive NdFeB magnets can be placed into thin control surfaces, but they may need considerable active cooling in hot aerodynamic environments. It is unknown if the field strength of these magnets will be high enough at this time. Electromagnets and superconducting magnets provide much higher surface fields than NdFeB magnets, but they carry a large weight penalty and must additionally be powered. Although NdFeB magnets have been discussed and tested to some extent in recent publications, more research should be conducted with them contained in compact control surface actuators. If NdFeB magnets prove to be powerful enough and can be cooled, the EMFC control should be more effective than control only with plasma. If not, plasma control with the rapid actuation effect becomes more advantageous.

Perhaps the best prospects for on-board EMFC with current technology are for improved control of high-speed missiles, which would benefit from surfaces that can actuate rapidly with reduced heating and drag when compared to mechanical actuators. A futuristic depiction is shown in Fig. 4.4. Power requirements will be raised, but improvements in on-board generators like state-of-the-art MEMS microturbines may be able to provide the same power input for 5 percent of the weight of current batteries [59]. With actuators creating a body force to control the direction of the missile, perhaps fins may even become unnecessary. Control may be initiated from many locations around the missile to maneuver it when segmented electrodes are placed around the diameter as shown. Magnets may be placed under the surface between the electrodes if EMFC is proven more effective than control only with plasma discharges.

As the fields stand now, active flow control with electromagnetic, glow discharge, and dielectric barrier discharge actuators are at different phases of development. Elec-

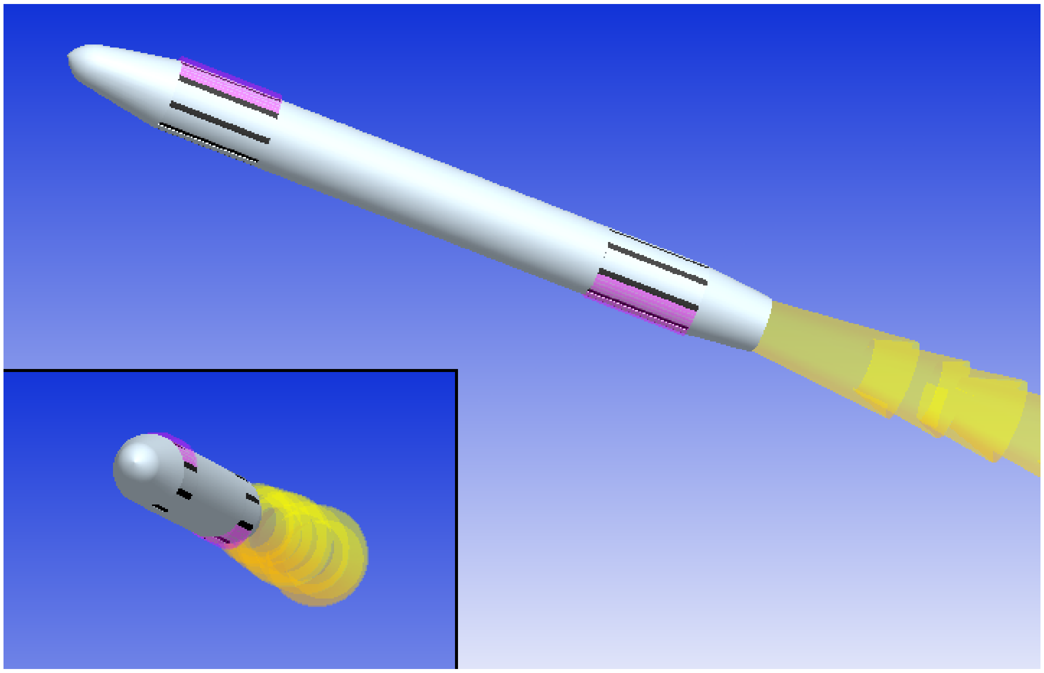

Figure 4.4. Example of a future high-speed missile with EMFC actuators that could potentially replace conventional control surfaces. Magnets may be embedded beneath and between the electrodes (colored black) and diffuse plasma (colored purple) is observed when the controls are actuated.

tromagnetic flow control is the least developed, with much to be studied about its performance in simplified flow environments like channels, wedges, and flat plates. Flow control with glow discharges has been studied for decades with simple flow environments, but more detailed and improved concepts appear to be trending away from being applied to blunt bodies to being used for aerodynamic control surfaces. Control with DBDs is the most advanced of the three with detailed experimental analysis of both the physical aspects and integration into potential flight systems. All have major design hurdles to overcome before they can be labeled flight-ready technology, where perhaps the largest hurdle is the integration of the power supply and additional electric circuit components into a vehicle. However, technical needs coupled with demonstrations of the potential that exists with EMFC and EFC systems make the prospects for further research in this field promising.

CHAPTER 5

LOW SPEED EMFC FACILITY DESIGN

5.1 Overview and Experimental Objectives

The discussion in the previous three chapters contends that experimental EMFC is still in an initial development phase where basic physics and interaction in simple environments are not yet well understood. Several factors were considered as critical towards the progress of testing these systems for future use in aerodynamic control. A facility was developed in an attempt to provide a solution to some of these issues by studying basic EMFC interaction. The main objective of this facility is to demonstrate that appreciable control can be obtained with a compact actuator where all of the components are placed on or embedded directly beneath a flat surface with minimum power consumption. Because of that particular objective, NdFeB magnets have been identified as an integral component of this EMFC actuator study. They are integrated into the actuator with electrodes similar to the geometry shown in the example from Chapter 2.

This study was conducted in a low-speed ($u_\infty \leq 50$ m/s) environment for a proof-of-concept demonstration of utilizing a compact EMFC actuator for boundary-layer control. Once the details of the concept are established, future work will be carried out in a supersonic flow environment which makes use of major components of the same test model. Although most of the promise for electromagnetic flow control lies in the regime of high-speed flight, it may be possible to gain an understanding of the characteristics of these systems at low speeds. However, the difficulty of creating low temperature plasma or a weakly ionized gas with an appreciable bulk conductivity should not be understated and may be a significant problem. The sought after characteristics include structure and magnitude of the Lorentz force, validation of dimensionless parameters that characterize actuator performance, and optimization of the force versus power consumption. The boundary layer survey was conducted by means of a particle image velocimetry (PIV) system, and a comparison must be made between boundary layers with no EMFC, an accelerating body force, and a retarding body force to determine if the Lorentz force has an appreciable effect.

The electrode potential of the EMFC actuator (a few hundred volts or less) is not high enough to ionize air at atmospheric pressure, creating the need for an additional system to generate conductive flow. Previous research has shown that a high-voltage system is effective for ionization, so it was selected as a potential method for this facility. Achieving a flow conductivity of a few ℧/m has been demonstrated only at low pressures ($p < 50$ torr) in the other facilities. In order to maintain a high level of flow conductivity at atmospheric pressure, a conductive particle seeder was designed to introduce another source of conductivity upstream of the EMFC actuator. For this facility, achieving a uniform conductivity with either method or some combination of both is acceptable for gathering the desired experimental results.

Consequently, the electromagnetic boundary-layer flow control facility can be divided into three main components: the conductive particle injector, the ionization plate, and the Lorentz force actuator plate. Three options were available for generating a Lorentz force with this facility. First, low ionization energy seed particles could be injected into the flow, ionized, and then passed over the Lorentz force actuator surface. Second, the particles may already be conductive, and they can simply be passed over the Lorentz force actuator for some control effect. If the first two options proved to be unsuccessful, a glow discharge could be created over the Lorentz force actuator. However, this third option was only capable of introducing small amounts

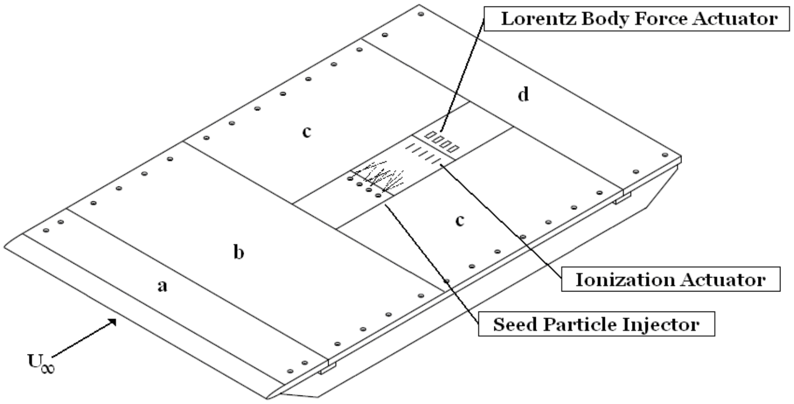

Figure 5.1. EMFC low-speed wind tunnel flat plate assembly.

of energy into the flow and glow discharges can be difficult to maintain in the presence of magnetic fields. These components are respectively labeled in Fig. 5.1 and shown as part of the low-speed wind tunnel assembly. In the figure, the conductive particle injector is shown to be injecting dry alkali salt particles. Each of the three component plates in Fig. 5.1 measured 15.25 cm × 20.3 cm. The elliptical leading edge of the flat plate, labeled as *a*, has a fineness ratio of 0.3 as typically found for low-speed boundary layer investigations [132]–[134]. The EMFC system components are located between the two filler plates each labeled *c*. A trailing edge plate *d* completes the assembly. The flat plate system has been assembled in the UT Arlington closed circuit, low-speed wind tunnel with a three-view optical test section. The test section itself measures 61 cm high, 91 cm wide and 190 cm streamwise. The tunnel has a continuously variable speed capability from zero to approximately 50 m/s. At its maximum operating speed, the tunnel is capable of obtaining a unit Reynolds number of 3 million/m.

Using Fig. 5.1 as a reference, the PIV system cameras were located outside of the tunnel near to the side of the plate labeled *c*. A single camera may be used for two-dimensional mapping, or two cameras can be combined for planar stereoscopic mapping. The frame rate was 5 Hz, which allows for the mean velocity field data to be obtained. An Nd:YAG laser was mounted over the wind tunnel, and a cylindrical lens formed a laser sheet parallel to the flow. The sheet can cover the streamwise distance of all of the plates, although the area of interest for the cameras during a particular experiment was often much smaller.

5.2 Conductive Particle Seeding

As was discussed earlier, conductive particles were seeded into plasma jets in order to raise bulk flow conductivity for a given value of power consumption. Even if a low-temperature ionization system was built similar to what has been demonstrated in the literature [40, 49], it is not known if it will work as well at atmospheric pressure to place σ in the desirable range of 0.1–1.0 ℧/m. With a high MHD loading parameter, σ may have to be higher than that range for the electromagnetic body force to be recognized beyond Joule heating. If the control force is recognizable, then a difference will be noticed between applied accelerating and retarding forces with respect to the freestream flow.

Two methods of conductive particle seeding were considered for this study. First was the injection of low ionization energy dry particles such as potassium or cesium carbonate which will be ionized by a high-voltage field before passing over the Lorentz force actuator. Second is the injection of particles that are already conductive. These can be in the form of powdered metals or a fine spray of an aqueous salt solution.

5.2.1 Dry Particle Selection

The term *ionization energy* is the amount of energy required to remove an electron from a particular atom or molecule. Depending on the properties of the atom or molecule, the ionization energy can vary significantly. Table 5.1 lists the ionization energies of several elements used during previous electromagnetic flow control and MHD propulsion studies.

Table 5.1. First electron ionization energies of several elements

Element	**Ionization energy, eV**
Oxygen	13.62
Nitrogen	14.53
Helium	24.59
Potassium	4.34
Cesium	3.89
Sodium	5.14

As can be seen from the table, alkali metals such as sodium, potassium, and cesium have energies much lower than monatomic oxygen and nitrogen. It can be noted that the ionization energy of diatomic oxygen is less than what is shown in the table for monatomic oxygen. However, combining potassium and cesium into carbonate molecules yields ionization energies lower than what is found in air. Thus, in studies many decades ago, these common carbonates had been seeded into high-temperature gas flows to enhance conductivity. Building on those facts, it was assumed that injecting potassium or cesium carbonate particles onto a control surface where a glow discharge may form will enhance the discharge and allow for more energy addition into the flow.

The other significant parameter regarding low-temperature seed particle injection is the size of the particles themselves. Electric charges are not stored within particles, but on their surfaces. Therefore, it is reasonable to hypothesize that the ability to ionize and pass energy through seed particles will correlate with their overall size. The carbonates discussed below can be produced in the size of microparticles fairly easily, but previous magnetohydrodynamic studies have shown that flow settling can still be detrimental with microparticles [78]. Due to that problem, nanoparticle-sized carbonates are desirable for this study.

5.2.2 Seeding System

A dry particle seeding system was designed and built for this study. This system needed to be able to steadily inject nanoparticle-sized seed material into the wind tunnel flow without significantly disturbing the boundary layer. The system built addresses these issues by using a sheet of porous metal. On one side of the sheet, seed particles are contained in a high pressure environment up to 100 psig. The size of the holes in the porous metal then allowed for small particles to pass through in a uniform dispersion before they were injected into the air flow. The size of the particles injected can be varied by using different porous material grades. Figure 5.2 shows this seeding system and some of its components. The components next to the label *a* are part of the high pressure system leading into the seeder. Dry seed was placed into the system through the port labeled *d*. The particles fell inside the system to the section labeled *b*, where they were then passed through the porous material. After passing through the material, they collected in a chamber labeled *c* and rose up through the tube labeled *e* toward the injection plate. The entire system stands about 1.5 feet high, and the inner diameter of the exit tube is 0.375 inches.

The injection plate was constructed to uniformly disperse the seed particles across a width of about 10 cm which represented the width of the ionization and Lorentz force plate active electric components. This plate is depicted in Fig. 5.3. In this arrangement, the particles reached the plate through the tube labeled *a* from the

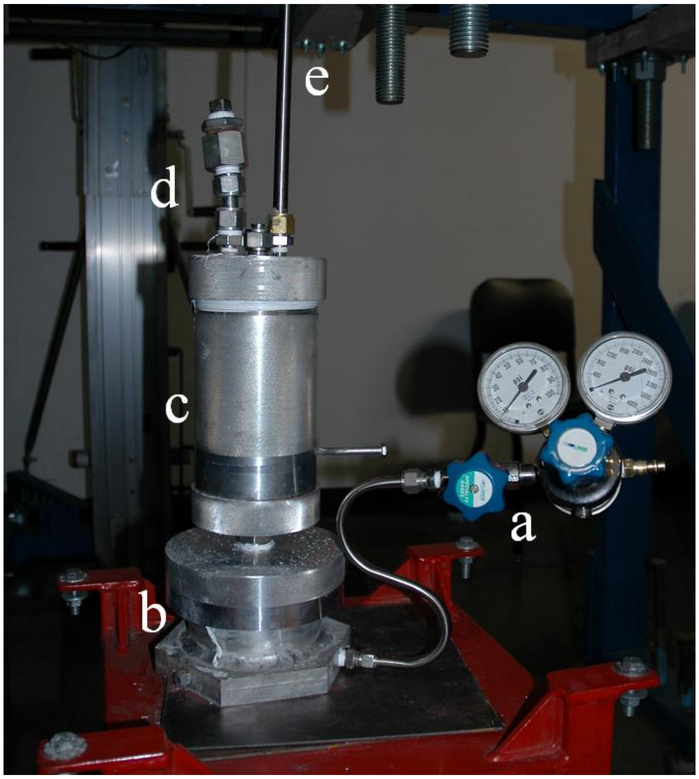

Figure 5.2. Dry particle seed injection system.

seeder system. The tube was cut into the base material labeled *b*. The component labeled *d* was a screw that was inserted into the base material. A hole was cut in its center to connect to the main tube, and holes placed radically around the head of the screw allowed for seed to be dispersed into a holding chamber, which is shown as a dark region between the base material and the flat plate material labeled as *c*. Three of these screws were placed next to each other perpendicularly to the flow. Finally, the particles were injected into the air flow through about 30 oval slots labeled *e* and cut into the flat plate at an angle of 15 degrees with respect to the surface so as not to adversely affect the boundary layer. The inner diameter of tube *a* is 0.1875 inches, and the inner diameter of each of the slots is about 0.125 inches.

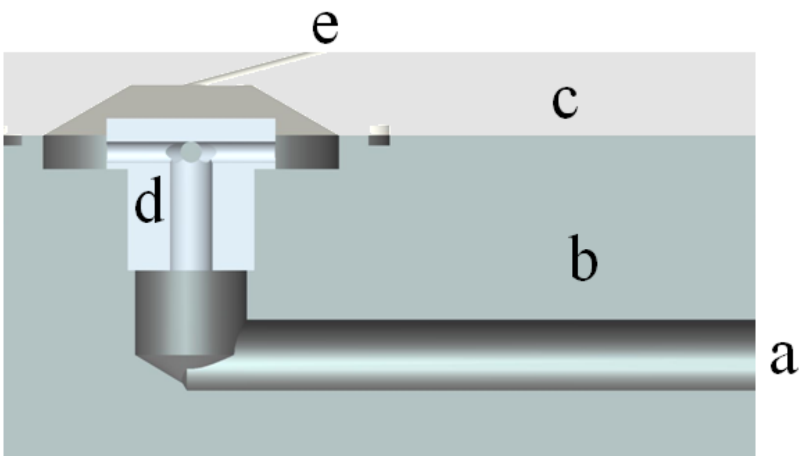

Figure 5.3. Dry particle seed injection plate.

5.3 Ionization System

An effective ionization plate must be capable of interacting with the ionized particles that it creates without the complications of uncontrolled arcing. The method of ionization for this study is to pass the uniformly dispersed seed particles though a high voltage DC electric field, known as field ionization. For this case, a strong electric field forcibly extracts an electron from an atom. By charge exchange ionization, electrons are exchanged with another atom through the outer valence shells. The dimensions of the electrodes are dictated by the minimum separation distance required to prevent arcing [89]. Thin electrodes also tend to produce more of a corona discharge effect due to the concentration of charge on sharp surfaces. Using these principles, an ionization actuation plate was constructed with five electrodes (two positive, three ground) using approximately a one inch spacing between each. A 20 kVDC Glassman power supply is used to generate the electric field. For the maximum voltage, the electrode spacing is close to the minimum requirement to prevent arcing (roughly 1 mm of separation per kV for air under normal conditions). Since the seeded air has an elevated electrical conductivity, arcing is prone to occur. However, it is hypothesized that the air flow will somewhat reduce the tendency of arcing between the electrodes. Simple experiments conducted thus far using the ionization plate showed that an arc can be effectively "blown out" by a low-speed flow. Therefore, it is plausible that DC ionization of seeded air using a glow discharge can still take place without arcing although there may be a limited range of operation between conditions that suppress arcing while generating an appreciable amount of ionized particles.

Recent research involving ionization with high-voltage fields or even magnetrons [135] has shown that pulsed electrical discharges may be superior to a DC discharge. Unlike DC discharges, the pulsed discharges do not permit charge to build up on the surfaces of the electrodes which is a precursor to arcing. Depending on the success of the present DC field ionization attempts, the Glassman power supply presumably could be linked to a high voltage semiconductor switch allowing for pulsed operation up to several hundred kHz.

Recombination of the ionized particles between the ionization and Lorentz force plates (roughly a 3 cm gap using the current fabricated geometry) may pose a problem for this EMFC concept. According to Jahn [89], recombination rates depend on many properties including the chemical species involved, temperature, and density. Ionized gas formed by high temperature dissociation demonstrates rapid recombination [136]. However, low temperature seeded ionization should see a lower recombination rate for two reasons. First, the lower temperature means that the intermolecular collisions between particles will be slower. Second, the heavy radicals of the ionized seed material will travel much slower relative to the free electrons after high-voltage excitation. Very little literature appears to have been published on low temperature recombination of gases, especially in the presence of particle seeding. It is possible that nonequilibrium reactions formed between injected seed materials and air constituents during ionization may play a significant role in the recombination rate. Plasma spraying, as part of the thermal spraying industry, successfully seeds a plasma jet before it is accelerated past the anode and cathode region out to coat a surface. However, this spraying begins with a high temperature arc similar to a plasma torch. Cold plasma spraying, perhaps the most promising example to bolster our recombination presumptions, has been previously demonstrated [137, 138]. If the recombination effects prove too difficult to overcome in the gap between the two plates, the power supplies may be able to be merged into one plate with two separate pulsed power supplies and a circuit involving high-power, high-voltage diodes.

The hypothesized operation of the ionization plate can be summarized as follows. Once the low ionization energy particles are introduced upstream, the ionization plate first breaks them into ions and heavy radicals. Since this process occurs at a low temperature, recombination of the particles will be relatively slow when compared to thermal ionization. The particles are then convected downstream, where their charge allows for energy addition by the Lorentz body force actuator. The conductivity of powdered metals seeded into the flow means they need only to pass over the Lorentz body force actuator.

5.4 Compact Lorentz Force Actuator

5.4.1 Conceptual Design

In order to create an accelerating or retarding Lorentz force, magnets and electrodes must be alternated across the width of the flat plate perpendicular to the flow direction. This arrangement results in each electrode pair crossing over one embedded magnet face, with the magnetic poles interchanged across the width. Grounded electrodes are placed at each end of the actuator to maintain a uniform force direction. Additionally, this placement may also prevent arcing to a tunnel wall or some other

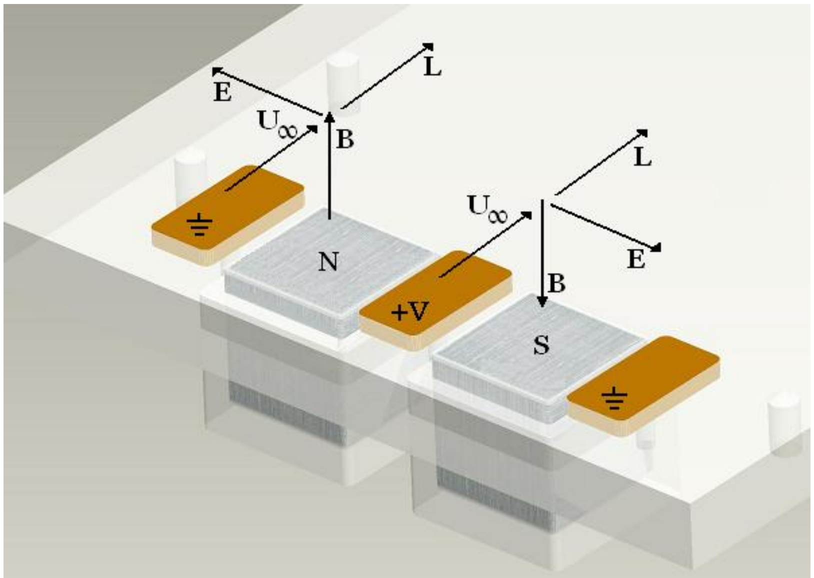

Figure 5.4. Schematic of a Lorentz force generator plate depicting the electromagnetic arrangement and force field interaction. The flat plate material is translucent to show embedded magnets.

component. Figure 5.4 shows a schematic of the actuator design with a single electrode that delivers power, including an idealization of the electric and magnetic field directions. Here, the magnetic and electric fields are oriented in orthogonal directions above the actuator depending on the polarity of the magnet, with the fields crossing each other to produce the Lorentz body force in a single direction acting parallel with the flow. As shown in Fig. 5.4, the magnets are embedded a few mm below the plate material since exposing the magnets would produce arcing between them and the electrodes. Without the magnets embedded in the surface, the constricted arc would never deliver energy to the flow in the boundary layer. Several generator plates have been fabricated in this fashion, all with a width of about 10 cm to allow for testing in the UT Arlington low-speed and supersonic wind tunnels.

As was discussed in the review, previous work in EMFC has used electromagnets. When compared with rare-earth magnets, electromagnets have considerable advantages for aerodynamic ground-testing applications, namely, a much stronger B field for better control results. However, rare-earth magnets generate a higher B field with respect to their overall weight and do not require a dedicated power supply. Since the goal of this facility is to demonstrate the feasibility of the aforementioned three-component configuration and reduce power consumption, rare-earth magnets were selected. Small, widely available NdFeB magnets can reach a surface field of roughly 0.5 T, while those that fit into the size constraints of the Lorentz force actuators used for this study range from 0.4 to 0.6 T.

In a low-speed testing environment, it was decided for practical purposes that a power requirement of no larger than 1 kW should be used for these actuators, which were arbitrarily decided to active surface area of roughly 25 cm^2. In fact a power requirement of a few hundred watts or less would be ideal. Copper electrodes and an acetyl-copolymer flat plate material were selected for the low-speed study since they are easy to machine and can handle the Joule heating from power consumption of this magnitude. For a high-speed environment, the flat plate material will likely have to be a machineable ceramic like boron nitride.

5.4.2 Optimization

During the beginning of this study, it was understood that the applied voltage for the Lorentz force actuator should be on the order of several hundred volts or less. Using Ohm's law, with estimates of electrode separation distance (about 2 cm) and boundary layer flow conductivity, the power input to the flow can easily exceed tens of kilowatts. Two benchtop power supplies previously used for other projects were considered for this study. One has a maximum voltage and power setting of 150 VDC and 450 W, while the other is limited to 70 VDC and 1260 W. These supplies were initially viewed as compatible with the low-speed experimental power requirements.

Another high-power supply was created for future high-speed experimentation as described in Appendix A.

As far as optimization is concerned, a concrete strategy has not been determined in previous literature. The fact that the MHD loading parameter should be minimized is understood, but the electrode voltage range is set to 600 VDC or less between all three power supplies. A strategy developed for optimization was centered on varying the width of the electrodes while keeping all other properties constant. This strategy would allow one to see how the Lorentz force uniformity could be positively affected by the actuator geometry. A computational magnetohydrodynamics program was used to provide a rough estimate of the actuator magnetic field strength, electric current and Lorentz body force for a two-dimensional array of magnets and electrodes assuming a perfect gas with a uniform conductivity profile. The inputs to the program are freestream velocity, flow conductivity, the actuator geometry, and the surface values of the electrode voltage and magnetic fields. The computational process begins with a turbulent approximation of the boundary layer velocity profile over the flat plate, where z is the height above the plate [36].

$$u_{BL} = u_{\infty}\left[1 - e^{\left(-\frac{4.6052z}{\delta}\right)}\right] \tag{5.1}$$

Figure 5.5 shows a schematic of the computational domain imposed over a magnetic field component B_Z calculated by the program. In the figure, M, E, and G stand for the spanwise widths of the magnets, electrodes, and gap distances, respectively. To understand how the electrode width affects the Lorentz force uniformity, seven widths between 0.318–2 cm were used in the program. The widths of the magnets and gaps were fixed at 2.54 and 0.16 cm, respectively. The magnetic field component B_Z was set to 0.5 T with alternating polarity as can be seen in Fig. 5.5. A potential difference of 100 V was applied to the central electrode and the boundary layer thickness δ was

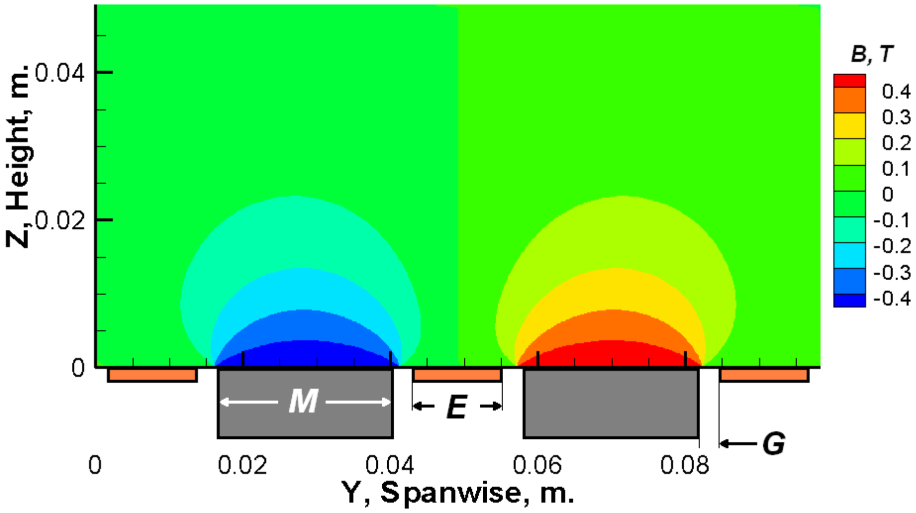

Figure 5.5. Schematic of the computational MHD code used for the EMFC actuator optimization.

set to 1 cm. Figure 5.6 contrasts the actuator uniformity produced by these electrode widths. The axes in the figure are normalized to display the Lorentz force contours, which have been taken at $z = 0.5$ cm, representing a height of half of the boundary layer. Since varying the electrode widths in turn varies the total width of the actuator, each width was normalized to 1 so as to better view the parametric results. The center of the actuator remains at a spanwise value of 0.5, but the locations where the magnets and electrodes are contained varies in this figure. For thin electrodes, the Lorentz force is greatest over the central electrode and drops significantly over the embedded magnets. Widening the electrodes definitely results in a more uniform Lorentz force, although it still varies significantly along the spanwise arrangement. Electric charge accumulates at both edges of the central electrode, and as the width is increased the reduction in charge in the middle of the central electrode is apparent as the Lorentz force begins to drop in that region. Since it was desirable to create an appreciable Lorentz force over the entire actuator, very thin electrodes were removed from consideration. Wider electrodes also would reduce E over the actuator which

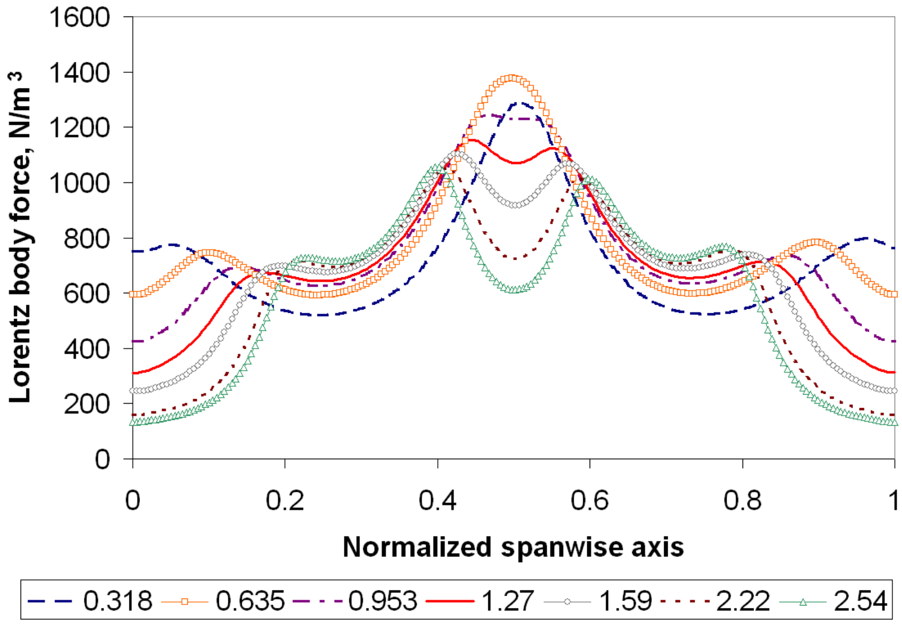

Figure 5.6. Normalized Lorentz force versus normalized actuator spanwise width for various electrode widths between 0.318–2 cm.

helps to reduce the MHD loading parameter. However, wider electrodes also mean that the Lorentz force magnitude is reduced. Power consumption can be extracted from the simulations by averaging the current field over the central electrode and multiplying the result by the 100 V potential.

Figure 5.7 shows the average Lorentz body force versus electrode width at a height of 0.5 cm over the actuator surface. The average body force was calculated from the values of the 200 grid points positioned at $z = 0.5$ cm. Note that the body force at this height is not representative of the body force produced by the entire actuator, and the height is used arbitrarily only to establish trends based on the electrode width. From the graph, it appears that the average body force reaches a maximum while using electrodes with a width of 1 cm, which is roughly half of the width of the embedded magnets. The data in Fig. 5.8 shows that power consumption rises as the width of the electrodes is increased, understandably so because the active area of the

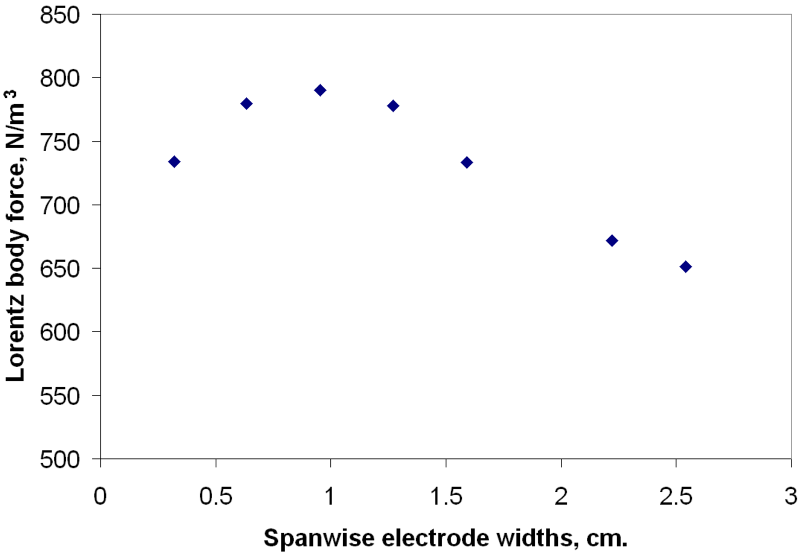

Figure 5.7. Lorentz body force versus electrode width at a height of 0.5 cm over the actuator surface.

actuator is thereby increased. Figure 5.9 contains a ratio of these two values, and it appears that the Lorentz body force/power ratio increases as the electrode widths are decreased, which is a good trend. However, this computational model does not account for Joule heating and the results contradict the known effects of the MHD loading parameter (where efficiency will decrease as E increases). Accounting for both of these optimization results, it was decided that the spanwise electrode widths should be approximately half of the widths of the embedded magnets. This choice results in the body force of greatest magnitude. It appears this practice will result in a middling level of efficiency.

5.4.3 Characterization and Magnetic Field Mapping

The actuator for the remainder of this study consisted of a 5-electrode, 4-magnet arrangement as shown in the review section. A summary of the geometry is shown

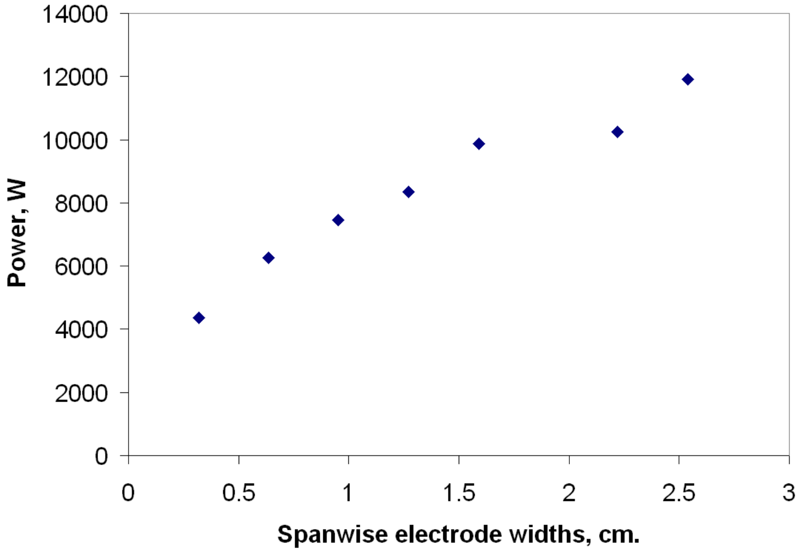

Figure 5.8. Power consumption versus electrode width at a height of 0.5 cm over the actuator surface.

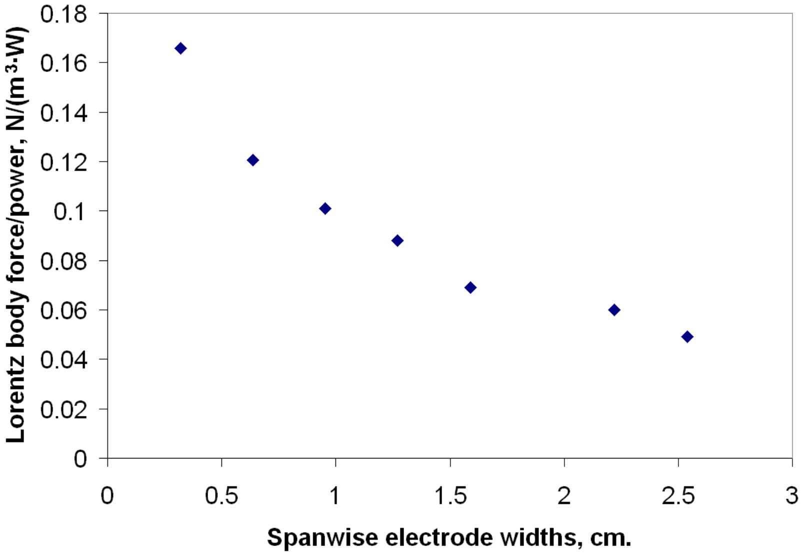

Figure 5.9. Lorentz force/power consumption ratio versus electrode width at a height of 0.5 cm over the actuator surface.

in Table 5.2. A computer-generated image of the actuator is shown in Fig. 2.1 in Chapter 2.

Table 5.2. Five electrode, 4-magnet EMFC actuator geometry summary

Component	**Dimensions**
NdFeB magnets ($x \times y \times z$, cm)	$1.27 \times 1.27 \times 2.54$
Electrode surfaces ($x \times y \times z$, cm)	$1.27 \times 0.51 \times 0.32$
Active control surface area ($x \times y$, cm)	1.27×9.04
Electrode edge rounds (radius, cm)	0.08
Spanwise component gaps (cm)	0.16
Embedded magnet depth (mm)	≈ 1

A detailed analysis of the magnetic field B was performed at varying heights from the surface of the actuator. Unlike the results from the computational MHD program shown in Fig. 5.5, the magnetic field over the faces of the magnets is not constant. The field was measured using a Bell 5180 Hall Effect gauss meter connected to a transverse-style probe. Measurements were recorded using an automated traverse table with data imported into LabVIEW$^{\text{TM}}$. The structure of the magnetic field accurately reveals the magnitude of the Lorentz force over the actuator surface. While the B field can be uniform for ring-shaped electromagnets or superconducting magnets, it changes considerably for this actuator. Data were recorded up to a height of $z = 1.27$ cm. The transverse probe only measured one component of the magnetic field during a pass, so the total B field was constructed from the components B_X and B_Z measured at the same location. Figures 5.10 and 5.11 show the B_X and B_Z components measured at a height of 0.254 cm from the surface, respectively.

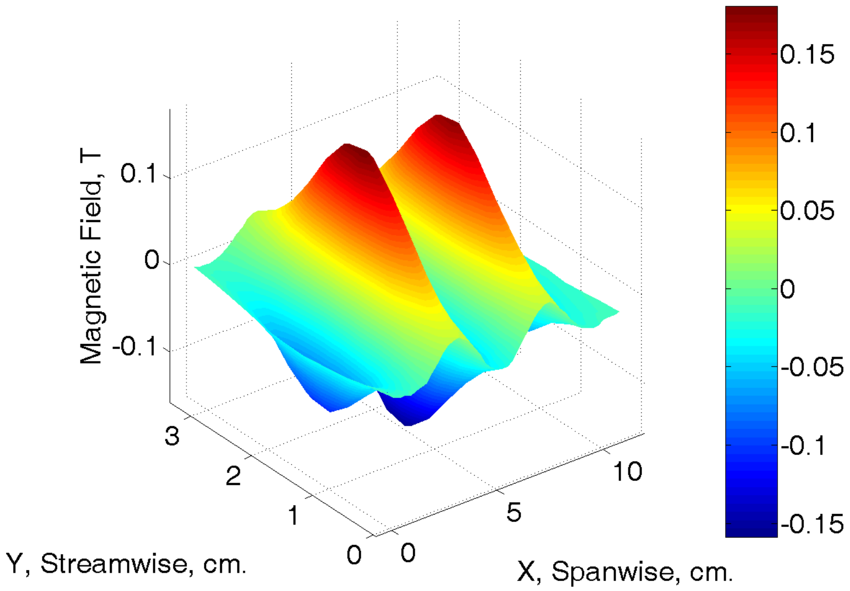

Figure 5.10. Magnetic field component B_X over the EMFC actuator at $z = 0.254$ cm.

Figures 5.12 through 5.16 show how the magnetic field decreases as a function of height from the surface of the actuator. To display the magnetic field directly on the surface of the actuator (see Fig. 2.2), the magnetic field present on the surface was extrapolated with an exponential fit of the data from the other heights since the geometry of the probe did not allow for a measurement directly at the surface.

5.4.4 Scaling Parameters

Several scaling parameters were approximated with the computational MHD program prior to experimentation with the actuator in this study. Results with the MHD code before this section approximated the magnetic field as uniform at the surface of the actuator over the embedded magnets. As the actual magnetic field mapping results showed, this approximation is far from accurate. In order to accu-

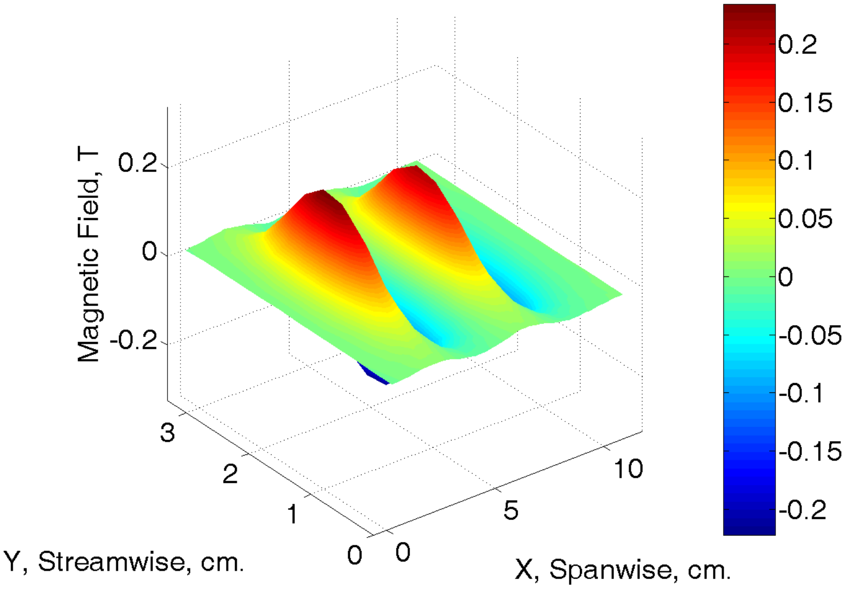

Figure 5.11. Magnetic field component B_Z over the EMFC actuator at $z = 0.254$ cm.

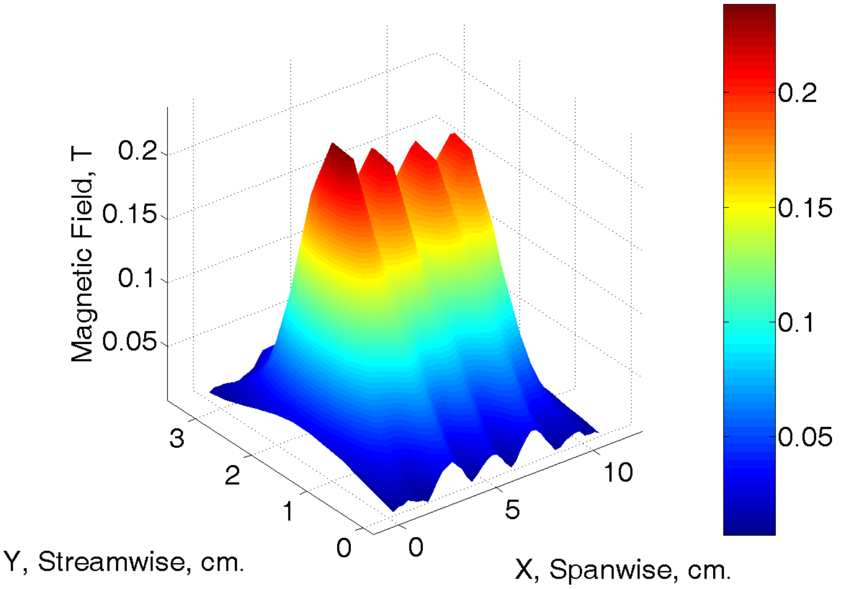

Figure 5.12. Total magnetic field over the EMFC actuator at $z = 0.254$ cm.

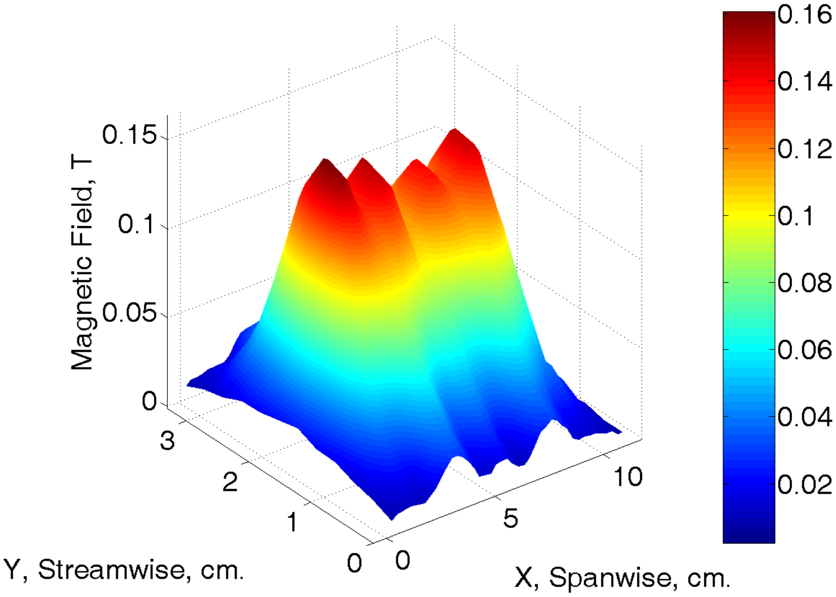

Figure 5.13. Total magnetic field over the EMFC actuator at $z = 0.508$ cm.

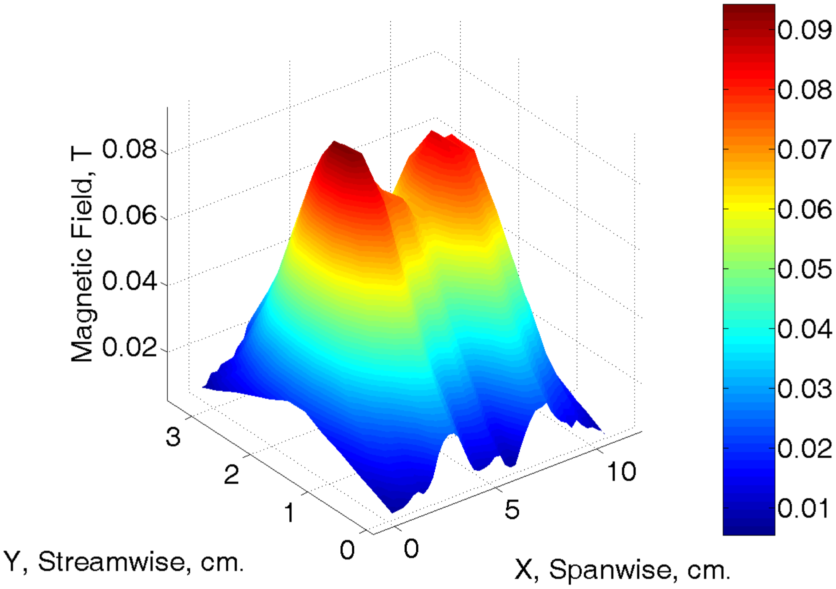

Figure 5.14. Total magnetic field over the EMFC actuator at $z = 0.762$ cm.

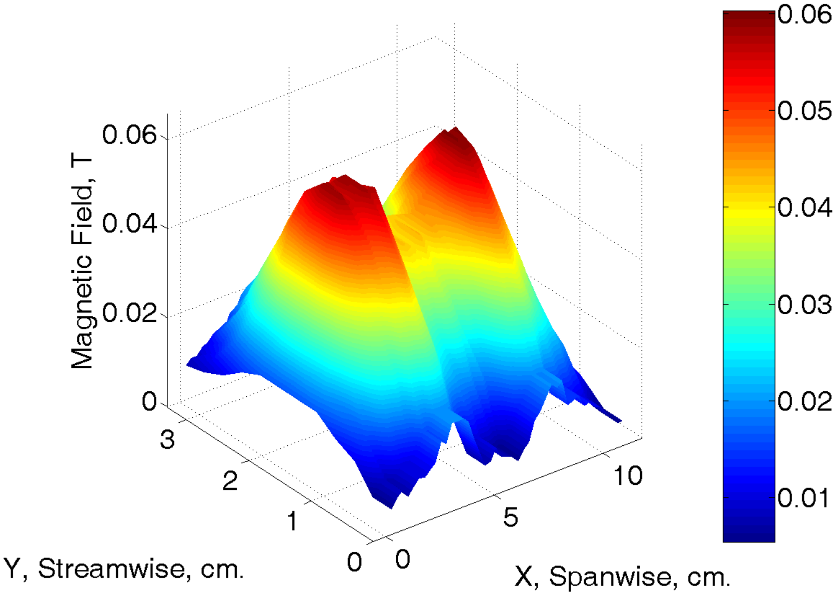

Figure 5.15. Total magnetic field over the EMFC actuator at z = 1.016 cm.

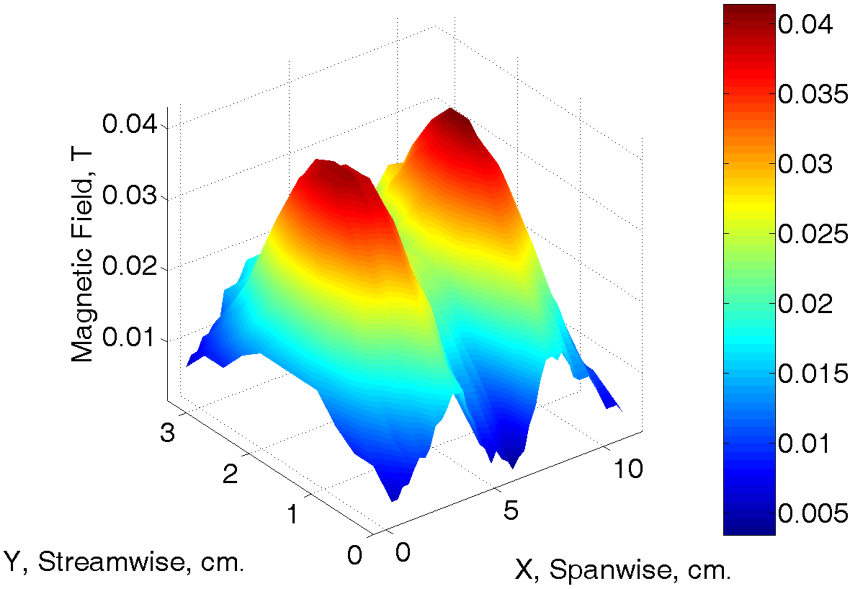

Figure 5.16. Total magnetic field over the EMFC actuator at z = 1.27 cm.

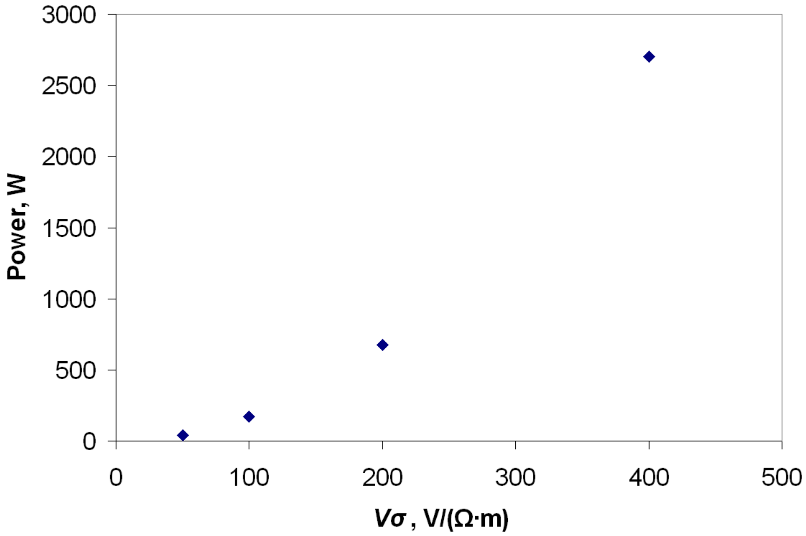

Figure 5.17. Power consumption versus actuator potential difference multiplied by conductivity.

rately depict the scaling parameters of this actuator, the magnetic field components B_X and B_Z were imported into the code as boundary conditions.

The four graphs that appear next in this section were constructed using a boundary layer thickness of 1 cm. Although the computations for these parameters were idealized for a physical environment where many loss factors are present in actuality, the results should estimate performance trends. Since these parameters all vary with freestream speed and electrode potential difference, the axes have been collapsed to account for variations in the terms. The trend lines were accurately established using only a few data points from the computations since the relationships were all straightforward. Figure 5.17 shows the actuator power requirement versus the potential difference of the electrodes multiplied by the flow conductivity present in the boundary layer. The result of the figure is that power scales with V^2 as expected.

Figure 5.18 shows the average MHD loading parameter within the boundary layer charted as a function of the potential difference across the actuator divided by

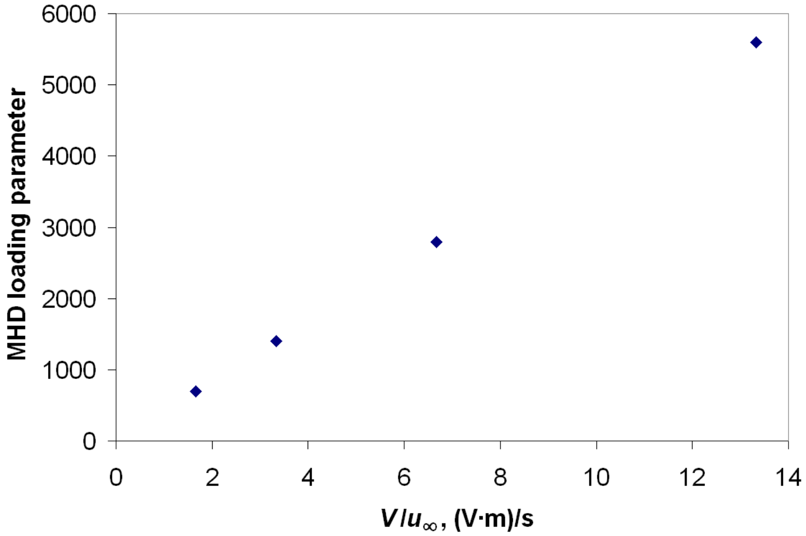

Figure 5.18. MHD loading parameter versus actuator potential difference divided by freestream flow speed.

the freestream flow speed. Unfortunately, the numerical results of this chart are a bit troublesome. As was stated earlier, a high MHD loading parameter means that the effect from Joule heating will be much greater than the effect from the Lorentz body force. A 100 V potential difference combined with a freestream speed of 30 m/s still results in a loading parameter of over 1000, which may be too high to separate any small Lorentz force effect from Joule heating.

Figure 5.19 shows I_{EM} charted as a function of $V\sigma/u_\infty^2$. Finally, Fig. 5.20 charts the Lorentz body force versus actuator potential difference multiplied by conductivity. Note that the relationship is linear since E is much larger than uB in the boundary layer and E scales directly with applied voltage. Consequently, the scaling parameter I_{EM} appears to be the most appropriate choice for this actuator. Once uB is larger than E, the relationship will scale more with u^2 and I_M becomes the better choice. However, the results of this chart and the use of I_{EM} still appear to hold even for freestream speeds near to the hypersonic range.

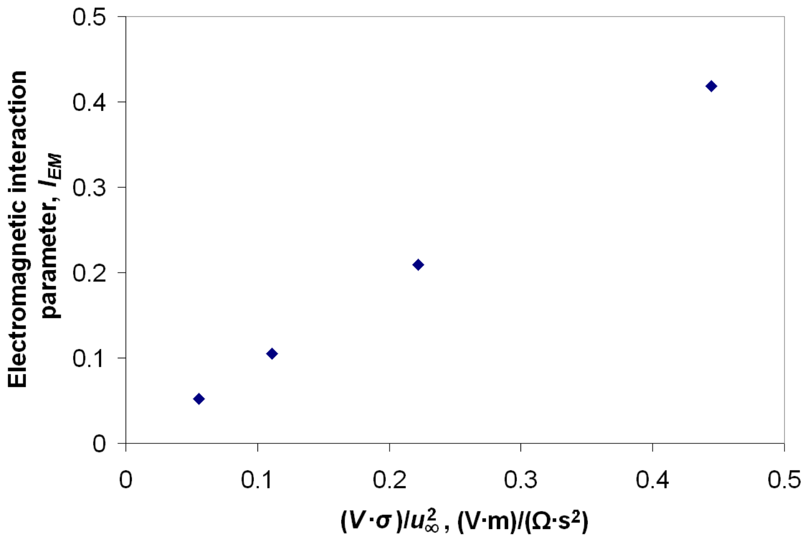

Figure 5.19. Electromagnetic interaction parameter versus $V\sigma/u_\infty^2$.

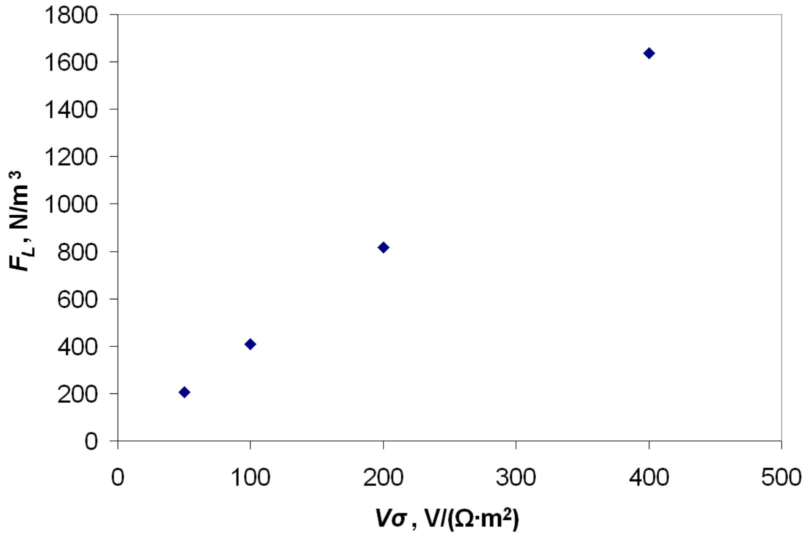

Figure 5.20. Lorentz body force versus actuator potential difference multiplied by conductivity.

CHAPTER 6

BENCH TESTING OF EMFC SYSTEMS

6.1 Ionization System Performance

The ionization actuator plate was bench tested using a Glassman DC power supply with an output range of 0–20 kV and a maximum current draw of 15 mA. Voltage-dependent current measurements were taken, with results shown in Fig. 6.1. Similar current-voltage trends have been established in previous research [89, 139]. Beginning at a potential difference of about 16 kV, the corona discharge is visible in a relatively dark room. As Fig. 6.2 shows, most of the visible discharge is located only very close to the electrodes. At a 20 kV potential difference, a uniform corona discharge is intermittently visible across the electrodes. However, this uniform discharge proved difficult to capture with the imaging equipment available. In addition to the static tests, a flow parallel to the surface was established using a pressurized air jet. Visually, the air flow tends to extinguish the corona discharge, which is verified by the fact that the power supply current decreases at the same time as the flow is established.

Experiments with an air flow over the plate while introducing seed materials were also attempted. First, a three molar solution of NaCl and water was introduced across the ionization plate using a spray nozzle. This solution caused the ionization plate to arc violently, as can be expected. Although the intense glow may visually appear to be uniform while the salt water seed is introduced, the power supply indicates that rapid fluctuations in voltage and current occur. Interestingly, reducing the ionization plate voltage to a range within a few hundred volts resulted in no current

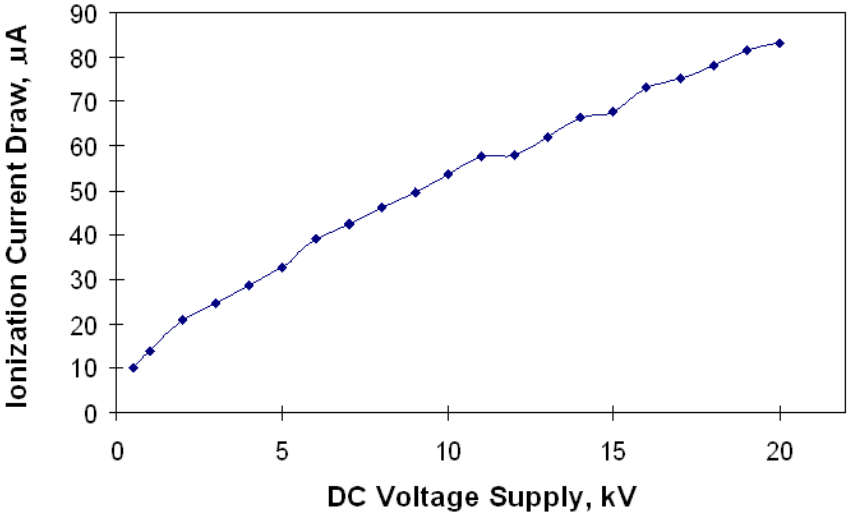

Figure 6.1. Glow discharge current versus potential difference of the ionization plate without air flow.

draw from the DC power supply, which means that the spray would not result in actuation of the Lorentz force plate.

Introducing potassium carbonate particles through the spray nozzle was also attempted. Despite using a potential difference of up to 20 kV on the ionization plate, the particles did not result in a more powerful glow discharge. This result was rather disappointing as it was originally assumed that, since potassium (and potassium carbonate) has a lower ionization energy than the components of air, their presence would enhance the static glow discharge. Reasoning for why it appears this assumption was incorrect is contained in the final conclusions. From the results of the salt water spray, it became apparent that a need existed for a merged design where a high voltage, low duty-cycle pulse would create an ionized path between electrodes whereby energy addition from a low voltage, high power DC supply would be facilitated.

Figure 6.2. Ionization plate setup and corona discharge at a potential difference of 20 kV.

6.2 Salt Water EMFC

The Lorentz force plate was bench tested using a three molar aqueous salt solution spread across its surface (15 % NaCl by weight). Blue dye was added for additional visualization of the mixture as shown in Fig. 6.3. The power supply was limited in this case to 120 VDC coupled with an 11.6 Ω load resistor. The result upon activation of the power supply was an instantaneous movement forward by most of the liquid layer.

If air was flowing from right to left in the figure, the result of this electromagnetic configuration would be a retarding force. Note that the upstream ionization electrodes are shown in the figure and were removed from their ground so as to not interfere with the propagation of the mixture. The voltage was applied only to the center electrode with the two others serving as ground to so the Lorentz force current would result in a body force acting in only one direction. The width between the ground electrodes in the figure is about 4 inches. Figures 6.4 and 6.5 show the voltage, current and power measurements across the electrodes as a function of time. The power supply was activated for a short time since the mixture boils quickly due to Joule heating. Figure 6.4 shows that the current spikes to 1.5 amps before falling to a more steady value of roughly 0.7 amps, where it can be deduced that most of the conductive layer moves off the plate shortly after the power supply is turned on. The geometry of the layer as it moves forward was expected to follow the Lorentz force contours of the computational results, but it appears that viscous effects of the water and hydrophobic nature of the plate material caused the layer to build up more towards the middle of the electrode gaps.

Using the geometry and the information from the three figures related to the plate actuation, it is possible to approximate the average conductivity, Lorentz force, and acceleration for the mixture when the power supply was activated. Using the simple equation $V = IR$, the resistance across each gap between the electrodes is approximated as 140 Ω. The conductance is the inverse of the resistance value, and dividing it by the length of the electrode gap yields $\sigma \approx 0.25\mho/\mathrm{m}$. The value is less than the conductivity of sea water, indicating that only a small amount of salt was used in our mixture. Higher salt concentrations were used in identical experiments which yielded current spikes up to 6 amps. Since σ scales linearly with the current draw of the Lorentz force generator, the 6 A value indicates that σ reached about 1 $\mho$/m for that case. Although the Lorentz force is very nonlinear as shown by the computational result, an order of magnitude approximation begins by defining a control volume over the electrode gap with a height equal to the height of the conducting layer placed on the plate. As was shown earlier for another actuator, an F. W. Bell 5180 Hall effect gauss meter was used to measure the three-dimensional magnetic field present over the configuration of Fig. 6.3. Averaging the magnetic field over a control volume height of 3 mm yields $B \approx 0.3$T. The electric field strength can be roughly averaged using the computational code results for E in the middle of the electrode gap, producing $E \approx 2000$ V/m. Since there was no flow velocity in this case, $F_L \approx \sigma E B = 150$ N/m^3. Multiplying the body force by the control volume yields an approximate Lorentz force of 1–2 mN. Neglecting surface tension and friction forces and solving for acceleration results in an instantaneous velocity of about 0.5 m/s

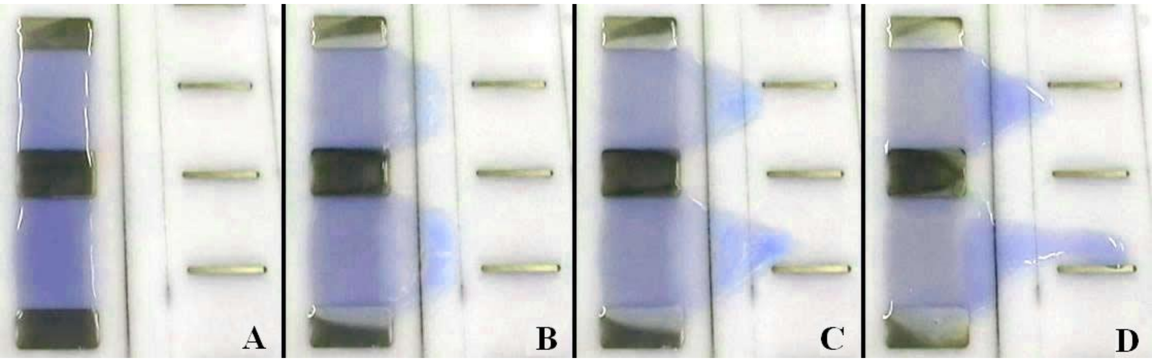

Figure 6.3. Frame-by-frame pictures of the Lorentz force generator plate actuation using a salt water mixture and dye for visualization.

when the power supply is activated. This value should rise considerably when using air instead of water because of the differences in mass. The tradeoff in that case is the difficulty in transferring energy of that magnitude into the air in the same time scale.

One interesting phenomena observed during the testing of the Lorentz force generator plate is the presence of vortex dipoles within the conductive salt water. While activating the electrodes with only distilled water and a small amount of food dye, they may be visualized. Apparently, the dye used interacts slightly with the electromagnetic fields, but not enough to generate a Lorentz force capable of displacing the fluid off of the electrodes. No appreciable current from the power supply was detected. The dye rotated inside the water and resulted in the image shown in Fig. 6.6. Although these dipoles have a strong effect in the aqueous salt and food dye solutions, they are expected to have a less significant impact on experiments with an air environment [140].

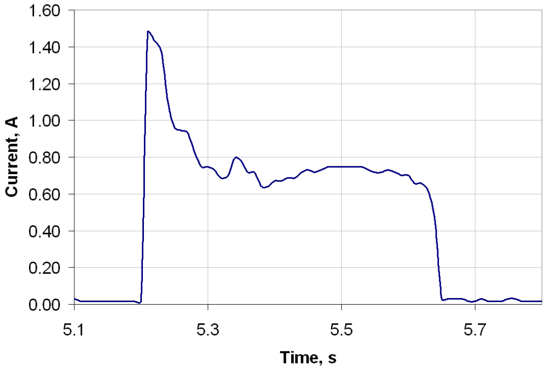

Figure 6.4. Current versus time during the actuation of the Lorentz force generator plate.

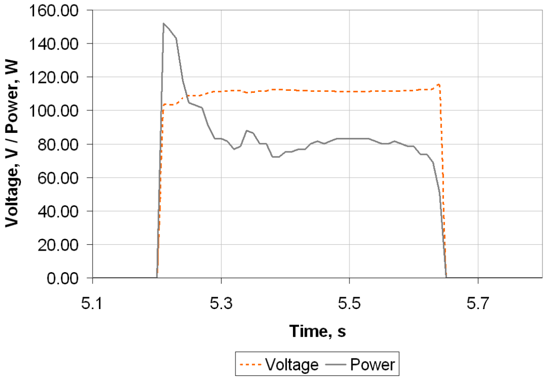

Figure 6.5. Voltage and power versus time during the Lorentz force actuation.

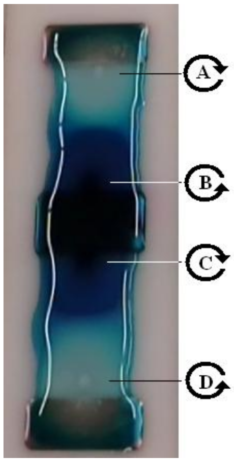

Figure 6.6. Visualization of four vortex dipoles.

CHAPTER 7

LOW SPEED WIND TUNNEL TESTING

This chapter discusses various attempts at creating an electromagnetic flow control force with alkali salt particle seeding, aqueous salt spray seeding, conductive particle seeding, and the establishment of a glow discharge over the EMFC actuator plate. The seeding efforts were altogether unsuccessful for reasons that will be elaborated upon. The glow discharge established over the actuator managed to slightly affect the boundary layer profile. Determining if the boundary layer was affected solely because of the plasma or by the Lorentz force is key to the data analysis in this chapter.

7.1 Flat Plate Boundary Layer PIV Survery

The low-speed wind tunnel was refurbished to provide improved flow quality and reliable operation for the tests. The three main EMFC components were assembled into a flat plate, and a PIV area of interest was established just downstream of the EMFC actuator. As discussed earlier, the laser beam sheet was focused onto the flat plate parallel to the flow. However, reflections from the laser beam off the flat plate interfered with the PIV imaging. This problem was mitigated by placing a Lexan insert directly behind the EMFC actuator. This window, shown in Fig. 7.1, allows for the laser sheet to pass through the flat plate without reflections, allowing for boundary layer velocity data to be collected beginning as close as 0.5 mm from the flat plate surface.

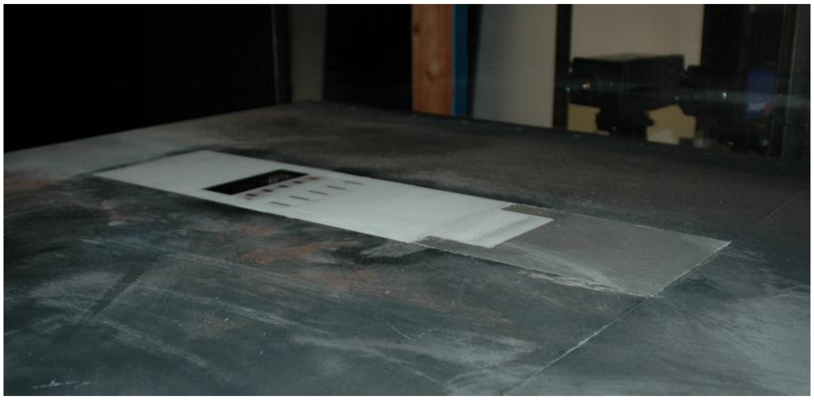

Figure 7.1. The EMFC actuator and its window shown with the ionization and seeder plates. Note that this picture was taken after alkali salt seed particles had already discolored the surface of the main flat plate.

The PIV window itself measured 4.5 cm streamwise by 11 cm spanwise. Depending where the window was placed relative to the flat plate, the Reynolds number in the vicinity of the window may reach up to 3.2 million based on the maximum achievable flow speed and a 1.07 m distance to the leading edge of the plate. It is desirable to know the freestream speeds in which the boundary layer was laminar, transitional or turbulent. This study considered one laminar condition and a number of turbulent ones.

Figure 7.2 shows the profile of a laminar boundary layer captured using the PIV system. The PIV grid spaces were sized at 16×16 pixels, and 2000 images were taken. About 10 boundary layer profiles from the PIV data grid were furthermore averaged, so each point in the profile is an average of 20,000 measurements. The freestream flow speed in this case was 3 m/s, which was created by setting the variable frequency wind tunnel motor to a 5 Hz run condition. Figure 7.3 shows the boundary layer graphed in the form of y/δ versus u_{BL}/u_{∞}. Graphed along with the experimental data is a typical laminar curve profile produced by Barlow et al. [141].

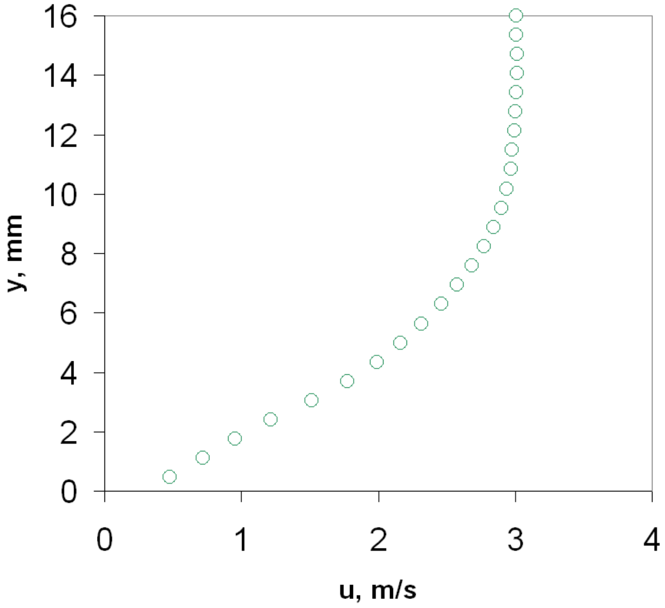

Figure 7.2. Laminar boundary layer profile measured across the PIV window for a freestream flow speed of 3 m/s and a Reynolds number of 190,000.

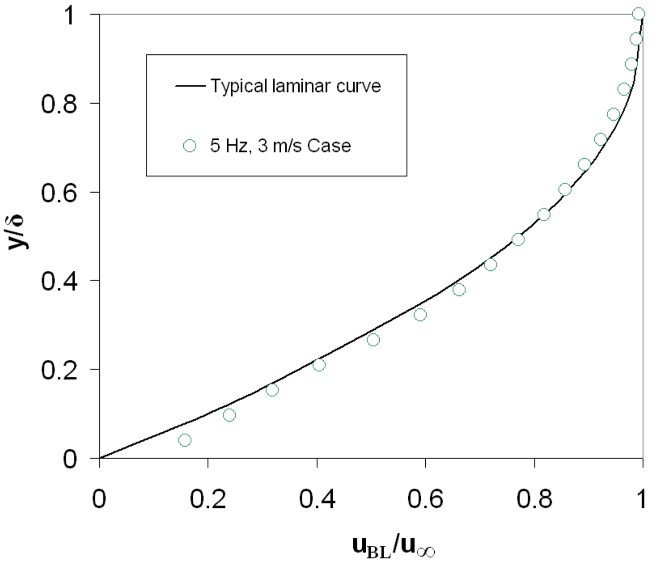

Figure 7.3. Laminar boundary layer profile of Fig. 7.2 graphed as y/δ versus u_{BL}/u_∞.

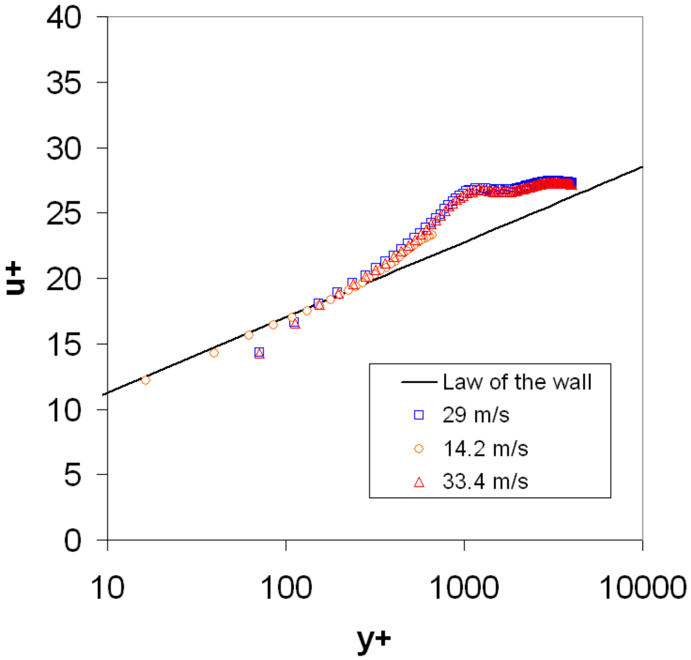

Figure 7.4. Three turbulent boundary layer profiles plotted with the law-of-the-wall profile.

When the wind tunnel controller was set to a frequency of 20 Hz or greater, the result is a turbulent boundary layer. The 20 Hz frequency corresponds to a freestream flow speed of about 14 m/s and a Reynolds number of 900,000. Freestream flow speeds in the 5–10 m/s range did not fit the laminar profile in Fig. 7.2 or the law-of-the-wall profile. The following three boundary layers were measured with the same PIV parameters outlined for the laminar boundary layer, and they are plotted in wall coordinates in Fig. 7.4. The plots are created by matching u^+ with the law-of-the-wall line between $35 < y^+ < 350$ using a least-squares fit [142]. The friction coefficient c_f was varied in the least-squares fit routine until convergence was reached. This represents a variation of the classical Clauser plot method [143].

As seen in Fig. 7.4, a boundary layer with a freestream flow speed of 14.2 m/s matched well with the law-of-the-wall profile down to $y^+ = 16$. Two other freestream speeds of 29 and 33.4 m/s also matched the law-of-the-wall profile and exhibited a moderate wake profile. Fitting points to the law-of-the-wall profile became difficult when y^+ is below 100 for these cases. Perhaps more precise calibration and testing at these speeds will improve the achievable y^+ range. The end result was that both laminar and turbulent boundary layers could be developed over the flat plate for the speed range of the tunnel. The laminar and turbulent boundary layer profiles were of good enough quality for low-speed EMFC studies.

7.2 Survey of Seeding Systems

Although the turbulent boundary-layer profiles exhibited normal behavior, the flow from the seeding system is another factor that may disturb the profile. The dry seeder was disconnected, and the PIV seeder was connected to the seeder plate in order to spray an olive oil aerosol into the flow which was considered to be the more accurate seeding technique. The seeder plate jet velocity is variable depending on the pressure supplied to both seeder systems. In each case, it was determined that the maximum supply pressure to both systems resulted in a jet flow velocity of about 1 m/s. The next three figures show the effect of the maximum jet velocity flow on the boundary-layer profiles.

Figure 7.5 shows the jet affecting four freestream velocities between 6 and 25.6 m/s. The boundary-layer profile for the 6 m/s can be considered transitional and the jet can be seen as a disturbance in the profile especially below $y/\delta = 0.4$. The jet had less of an effect on the other boundary layers, which followed a turbulent profile but had an increased wake profile. The three turbulent boundary layers are plotted with the law-of-the-wall equation in Fig. 7.6. There, the jet caused the profiles to rise slightly above the law-of-the-wall line below $y^+ < 200$. Finally, Fig. 7.7 shows two boundary-layer profiles for about the same freestream flow speed with and without

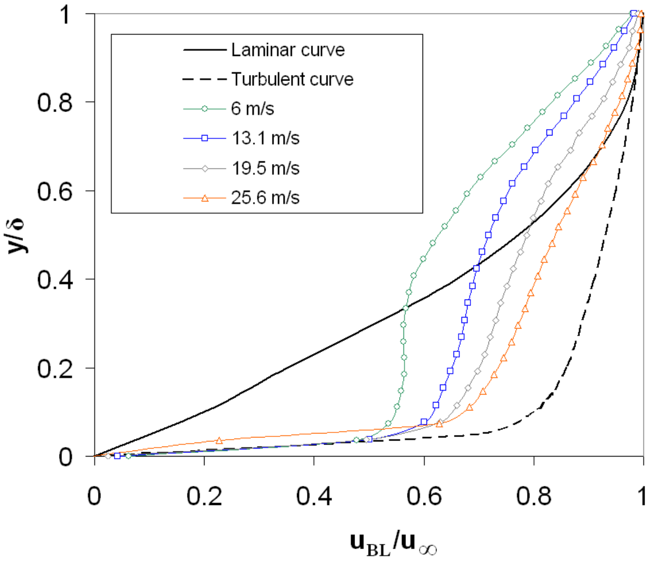

Figure 7.5. Four boundary layer profiles with different freestream speeds affected by the seeder plate jet.

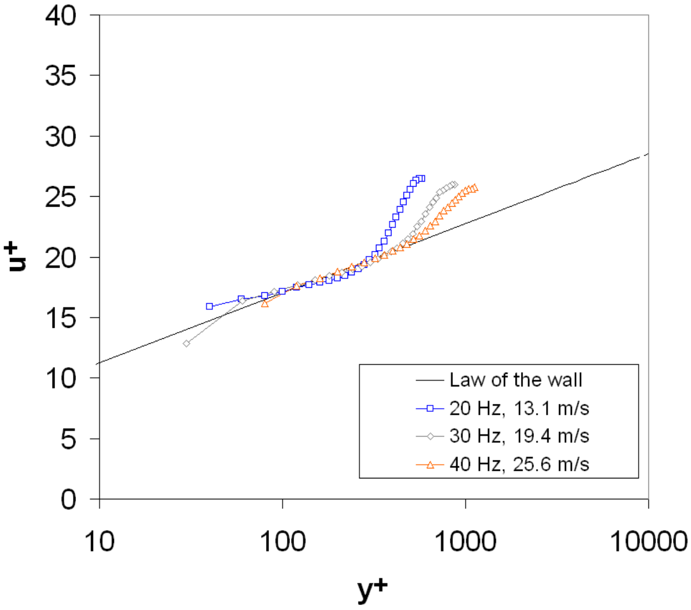

Figure 7.6. Law-of-the-wall profiles of three turbulent boundary layers of different freestream speeds affected by the seeder plate jet.

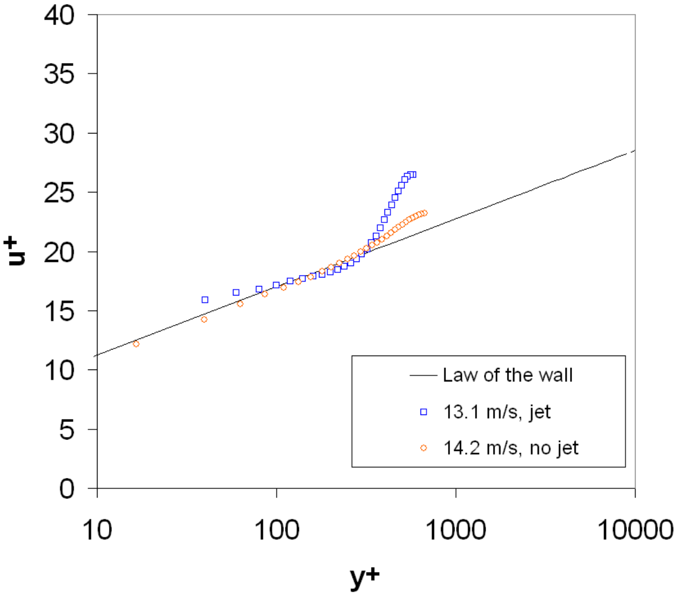

Figure 7.7. Law-of-the-wall profiles compared for similar freestream speed turbulent boundary layers. One case occurs with the seeder plate jet and one occurs without it.

the jet. Again, they are similar except for the slight rise when y^+ is low and the wake profile was larger with the jet. From these results, it appears that the dry particle seeder can be run with its maximum operating pressure when the freestream flow speed was above 15 m/s.

Another PIV survey was performed to investigate if dry particles could be seeded fine enough to generate accurate flowfield data. Figure 7.8 compares pictures taken with the typical olive oil aerosol from the PIV seeder and the dry seed (potassium carbonate in this case). The dry seed particles, although ground to a size of approximately 10–100 μm, are clearly much larger than the olive oil particles. The potassium carbonate particles began to clump together quickly after they were ground because the material is hygroscopic. For the 16 × 16 pixel PIV grid spaces, accurate results could be collected with the dry seed. However, the rate of seed expended was high, and only a few hundred images could be taken at once. Since resolved flow field data

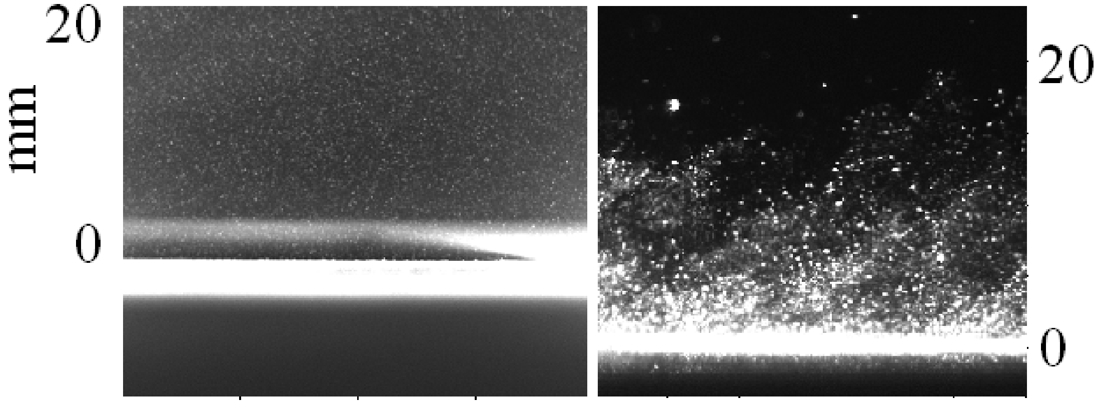

Figure 7.8. Comparative photographs of the PIV seed (left) and potassium carbonate dry seed (right) dispersions over the PIV window.

sets needed at least 1000 images, the olive oil mist and dry seed may need to be introduced to the air flow simultaneously. This situation is not desirable since olive oil acts as an insulator and may affect the EMFC experiments.

7.3 Attempts at EMFC while Ionizing Seed Particles

Dry potassium carbonate particles with sizes in the range of 10–100 μm were injected over the flat plate both while the wind tunnel was running and when no freestream flow was present. In both cases where the ionization plate potential difference was increased to 20 kV, no ionization of the seed particles occurred. With no flow, the seed particles continued to settle over the surface of the ionization plate electrodes and still no current was drawn from the power supply. When an atmospheric pressure glow discharge was established over the ionization plate, the injection of the seed did not appear to disturb the discharge again, even when seed covered the electrodes. A very small drop in current may be detected if the electrodes were completely covered. Figure 7.9 shows an example of a glow discharge with times listed when the injection occurred and when a significant portion of seed had covered the

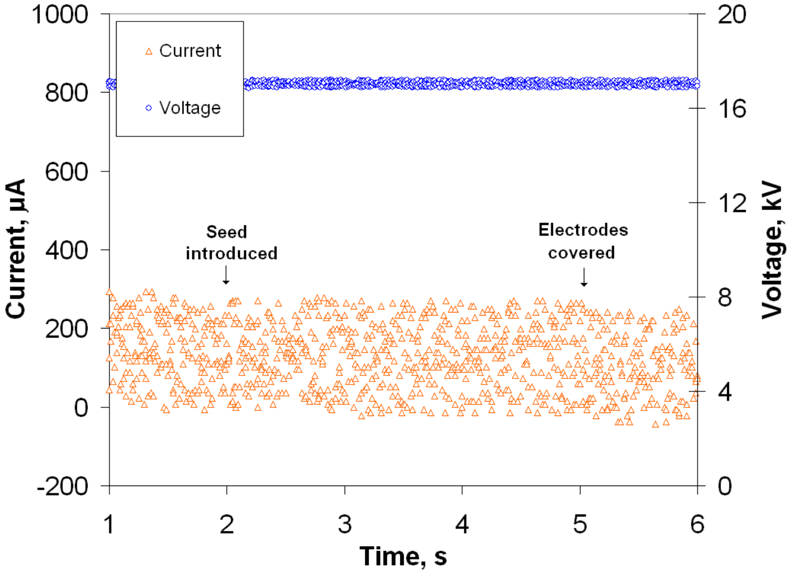

Figure 7.9. Potassium carbonate seed particles are injected over the ionization plate with an established glow discharge but no not significantly affect the discharge.

electrodes (which occurs quickly with no freestream flow). The figure clearly shows no change to the glow discharge power consumption by the seed, which acted as neutral particles.

An explanation as to why no ionization occurred with the seed is needed since the original hypothesis stated that potassium carbonate particles would be more susceptible to ionization when compared with air. Certainly, they have been known to produce a higher level of ionization in a thermal jet when compared to air. A comparison must be made between molecular and particle sizes. The size of the diatomic oxygen and nitrogen molecules is on the order of picometers. This means that the potassium carbonate particles produced for this study are up to one million times larger than the air molecules. It appears that the energy requirement to ionize these large particles is greater than the energy to ionize the air particles, despite the fact that the ionization energy of a single potassium carbonate molecule might be lower than that of diatomic oxygen. With the high pressure present, enough air molecules are available over the ionization plate to maintain the glow discharge even as the potassium carbonate builds up.

One may ask why injecting potassium seed is feasible in the thermal jet studies where the seeded particles were presumably just as large as those used in this study. The answer to that question is the energy from the thermal jets must have been high enough to vaporize the potassium carbonate and any other dry seed used. Once the temperature of the jet is greater than the enthalpy of vaporization of a particular molecule, the particle sizes with respect to the air are similar and the low ionization energy then can be utilized to increase conductivity (which allows for more energy addition into the flow).

7.3.1 Conductive Particle Substitution

Since the potassium carbonate seed particles and ionization plate produced no useful results, an attempt was then made to seed the airflow with conductive particles in the form of powdered metals. Powdered metals like iron which are attracted to the magnets are of no use. To prove the point, powdered iron was seeded into the airflow in a bench test, and, as expected, all of it was found stuck to the actuator surface over the faces of the magnets afterwards. Powdered aluminum, which is weakly paramagnetic which will not stick to the surface of the actuator if injected, is readily available in particle sizes of a few μm or less. However, powdered aluminum is available in this size range mostly as an additive to solid rocket propellant and professional fireworks manufacturing. When aluminum particles are very small, they become much easier to combust. For this study, it was conceivable that aluminum seed particles could combust when subjected to energy addition by an electric field, so they were ruled out as a candidate conductive seed. Copper powder is weakly diamagnetic and definitely will not stick to the actuator surface. It is also less volatile than aluminum.

Copper powder with a 150 mesh size (approximately 0.003–0.004 in. in particle diameter) was introduced into the wind tunnel flow by means of the dry particle seeder system. A potential difference of 150 V was applied across the EMFC actuator, but no current was drawn from the power supply as the particles passed over. Apparently, this voltage was too low to be able to form a conductive bridge between the electrodes with the copper powder. To learn what the minimum required voltage was, the 20 kVDC power supply was connected to the EMFC actuator and the experiment was run again. Interestingly, seeding the copper powder with the seeder set at its maximum flow rate did not result in any actuation other than the glow discharge present at a voltage of 15–20 kVDC. Visually, it appeared that the particles were not seeded in a large enough quantity into the airflow with the seeder system. In a test with no airflow, placing a large amount of particles over the actuator will cause a short circuit, and a smaller quantity will result in arcing similar to the figure for the aqueous salt injection presented in the next section.

It is presumable that smaller metallic particles may yield better results. Since the particles used were not even near to producing the desired results, the prospects of using nanoparticles appear the most promising. Many salts and metals can now be purchased in the nanometer size range. However, one practical issue stands in the way of using nanoparticles. The cost is very high. To record PIV data with 1000 or more pictures, several minutes of run time is needed which will use a large amount of particles. Nanoparticles were not considered during the time of this study primarily for this reason, although there remains the possibility that they could yield some experimental results. The atmospheric pressure environment may also be troublesome with the particles. With a turbulent boundary layer flow uniformity is difficult to maintain, and the copper particles may be more susceptible than other seed materials to forming highly conductive paths for arc discharges.

7.4 Attempts at EMFC with an Aqueous Salt Spray

Since EMFC experiments in a salt water environment do not encounter problems with energy addition to the flow, it was thought that a salt/water spray could be used as the conductive flow source for this study. A device that emits a fine water spray was purchased, and a solution of potassium carbonate and water was sprayed into the airflow. As Figure 7.10 shows, the result over the ionization plate is uncontrolled arcing. The current reaches its 15 mA limit several times when the circuit is fully shorted. The variability in voltage is not acceptable. Eventually the water settles onto the actuator surface, creating arcs that can damage the actuators. Another practical issue that is difficult to mitigate with aqueous salt spray injection into the wind tunnel is the fact that the salt builds up quickly on the Lexan walls. This buildup results in blurry PIV images and possibly permanent corrosion to the walls. An aqueous salt spray mixture also does not draw current from the EMFC actuator when a potential difference of a few hundred volts or less until the actuator is completely covered. In addition to experiments with the spray device, the same salt/water mixture was dispersed using the PIV aerosol seeder. Again, no current draw was seen from the EMFC actuator when these aerosol droplets, with particle sizes of about 1 μm, where dispersed over it.

7.5 Glow Discharge EMFC Actuator

The last set of experiments with this study involved the establishment of a glow discharge over the EMFC actuator surface. Although the energy addition to the flow

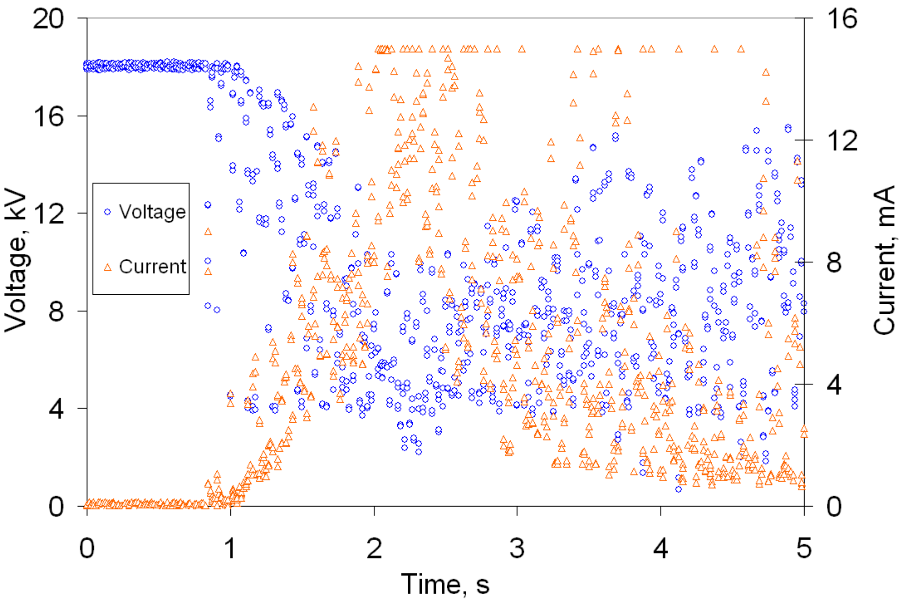

Figure 7.10. Results of spraying a salt/water solution onto the ionization plate with an initial potential difference of 18 kV.

was limited, this appeared to have some effect on the boundary layer. Uniformity was difficult to maintain for the glow discharge at atmospheric pressure and the actuator often arced when the potential exceeded 17 kV. In order to determine if the control effect was a result of plasma heating, Lorentz force, or some combination both, the polarity of the actuator was flipped with respect to the freestream flow direction to distinguish between any accelerating or retarding Lorentz force that may occur.

7.5.1 Accelerating Force Results

Although PIV data were taken at three different flow speeds, data with consistent glow discharge power consumption proved difficult to obtain. For consistency in this section, data will presented that was collected with a freestream speed of about 14 m/s. All PIV measurements were taken over the center of one of the positive electrodes, which is shown as the electrode second from the left in Fig. 2.1.

First, the potential difference of the actuator was parametrically varied to explore the effects on the boundary-layer profile. To ensure replication of the wind tunnel conditions before reaching the EMFC actuator, the experiments were conducted in succession during one wind tunnel run. Voltage and current measurements were taken at 15, 17, and 20 kV. The 15 kV case resulted in the most uniform glow discharge, while the 17 and 20 kV cases exhibited periodic arcing. Figure 7.11 shows a sampling of each current and voltage measurement for the three potential differences. The measurements were made during the period of PIV measurements for each case to ensure the energy addition to the flow at that time was fairly stable. Consequently, the time range of 15–30 seconds used for the graph is nominal. The sampling rate was set at a low value of 50 Hz as only the mean values of voltage, current, and power needed to be collected. Basically, the graph shows that all of the voltage and current levels were fairly steady, and the points that laid between the main voltage and current signals were signs that the measurements was taken during an arc. Each point represents a separate discrete voltage or current measurement. The 20 kV measurements account for most of these points. The 15 kV measurements had very few deviating points and the glow discharge current was very low compared to the other two currents. The average power consumption of the 15, 17, and 20 kV cases were measured as 0.40, 1.36, and 10.05 W, respectively.

Although the power consumption varied significantly between the three potential difference cases, the mean boundary-layer profile did not. According to the results of Fig. 7.12, the 20 kV case caused the smallest change to the mean velocity profile. The practical reasoning behind this situation is that the arcs that developed during the PIV data acquisition accounted for most of the average power consumption but they were concentrated over small volumes and did not affect the boundary layer. In these cases, the boundary layer thickness is approximately 15–16 mm between all of

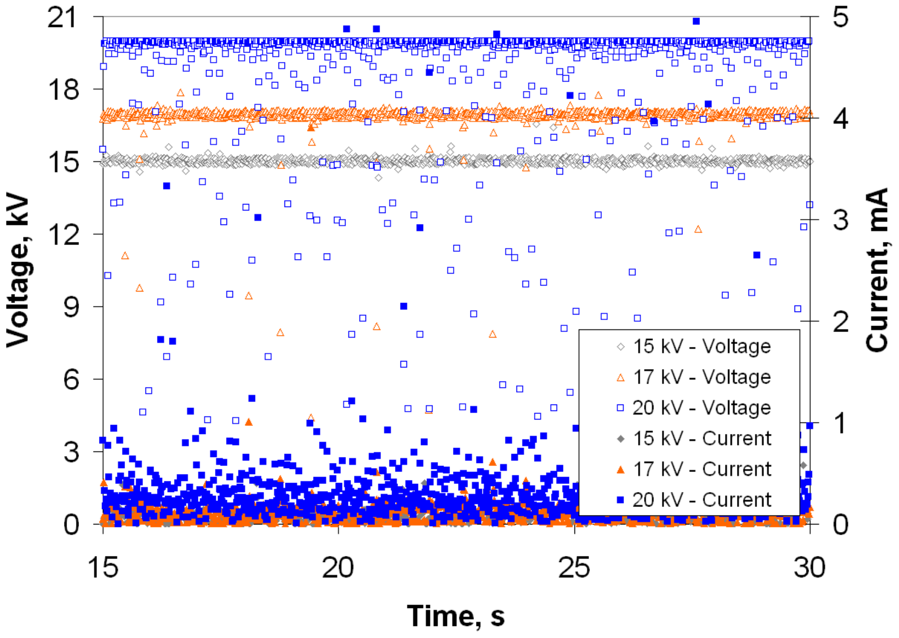

Figure 7.11. Voltage and current measurements taken during the PIV image collection for three different EMFC glow discharge potential differences.

the cases. Figure 7.13 shows the boundary layers plotted in coordinates to match the law-of-the-wall profile. The friction coefficient c_f converged upon a value of 0.00385 using a least-squares fit of the original profile to the law-of-the-wall profile. That friction coefficient was subsequently used for the rest of the profile calculations.

Although it appears that the actuator has some effect on the boundary-layer profile, the difference is minimal. The PIV data were further analyzed to see if any effect was clearly visible in the turbulent kinetic energy or Reynolds stress profiles. The next two figures chart these statistics within the boundary layer. The profiles were assembled from 15 data columns in each PIV picture, making each point in these plots an average of 15,000 data points. In the Reynolds stress plots, little difference is seen between the 15 kV and normal profiles, but the 17 and 20 kV potential difference profiles definitely increase the absolute magnitude of the Reynolds stress

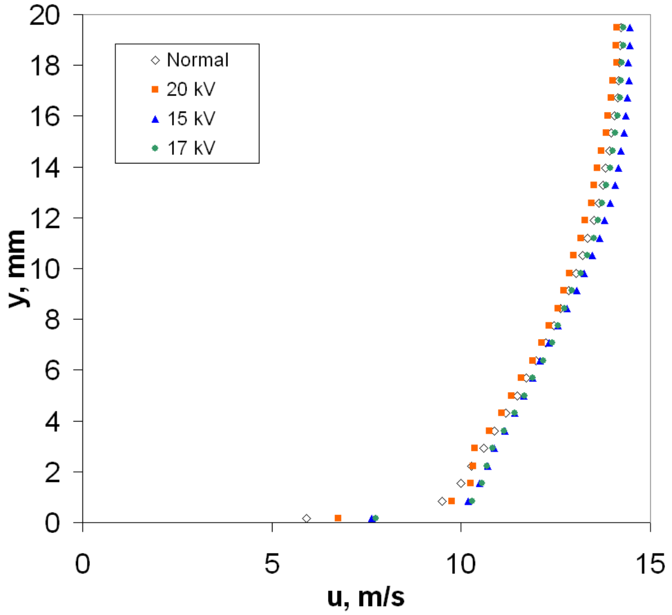

Figure 7.12. Boundary layer profiles for the 15, 17, and 20 kV EMFC cases as compared to the original profile.

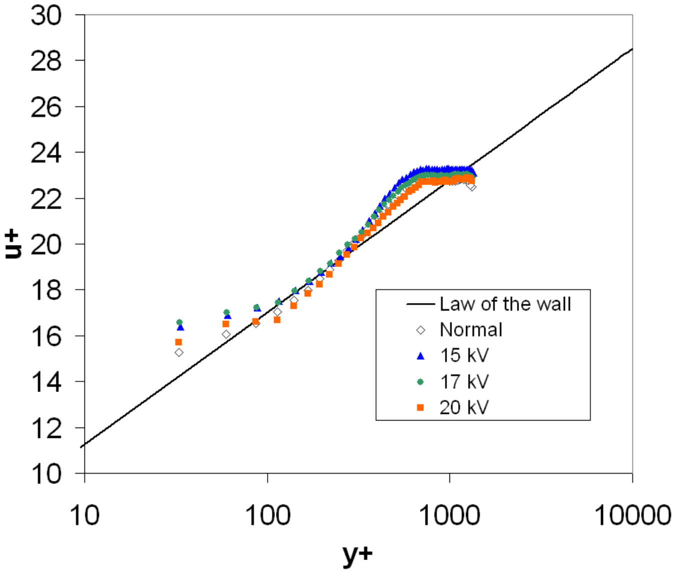

Figure 7.13. Boundary layer profiles for the 15, 17, and 20 kV EMFC cases as compared to the original profile and the law-of-the-wall profile.

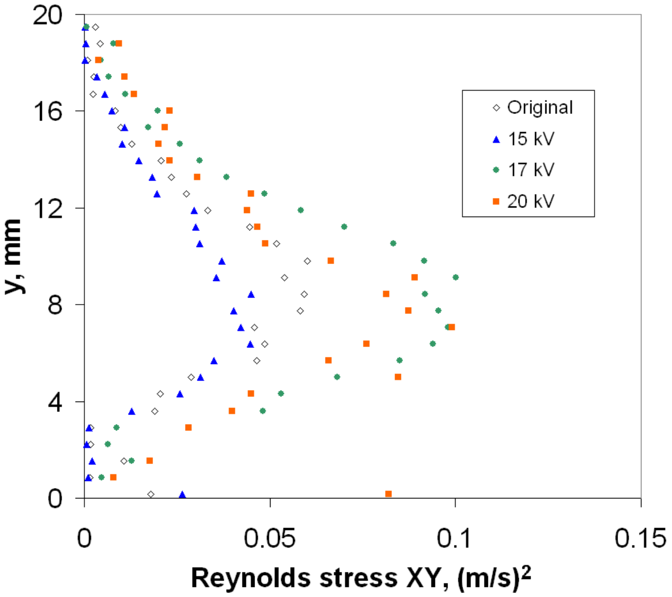

Figure 7.14. Reynolds stress profiles for the 15, 17, and 20 kV EMFC cases as compared to the original profile.

around $y/\delta \approx 0.5$. The 20 kV and 17 kV profiles are similar to each other again despite the large difference in energy addition to the airflow. This result is likely due to the arcing. In the turbulent kinetic energy plots, the 15 kV case still resulted in values of slightly lower magnitude than the original profile, but the turbulent kinetic energy in the 20 kV case was much larger than that seen for the 17 kV case.

7.5.2 Retarding Force Results

Continuing on, a similar set of experiments was run with the actuator flipped so any electromagnetic force would act in the opposite direction. An original boundary-layer profile was measured again along with glow discharges with potential differences of 15 and 20 kV. Between the accelerating and retarding force experiments, the actuator developed an internal carbon trace between two of the electrodes and an embedded magnet which resulted in a short circuit. Although appropriate repairs were made,

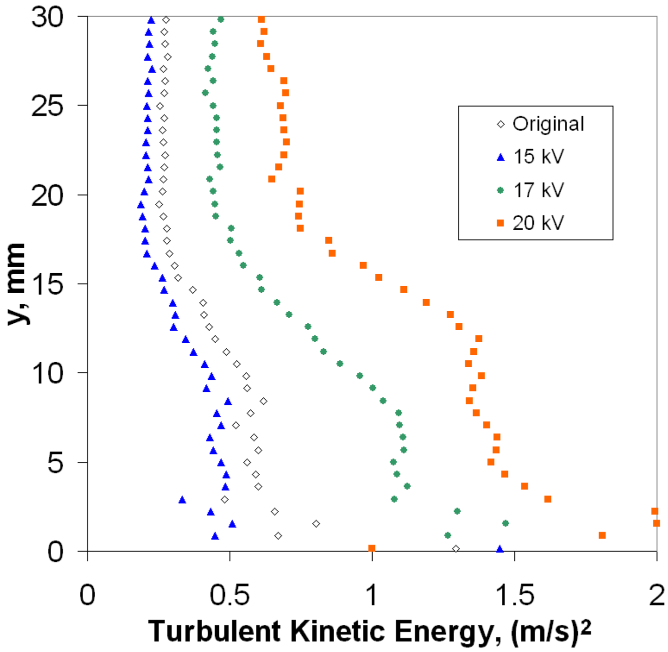

Figure 7.15. Turbulent kinetic energy profiles for the 15, 17, and 20 kV EMFC cases as compared to the original profile.

the power consumption of the glow discharges was slightly different for these cases. The average power of the 15 kV case was about 0.2 watts and was difficult to measure. The average power of the 20 kV case was increased to 16 W. These results certainly revealed some of the difficulty in replicating atmospheric glow discharge experiments. Figures 7.16 and 7.17 contain the boundary layer profiles in normal and law-of-the-wall coordinates. Little, if any, difference is seen between the presumed accelerating and retarding Lorentz force boundary layer profiles.

The final two figures in this section show the Reynolds stress and turbulent kinetic energy profiles for these cases. Since the original profiles have some variance but should be identical for the accelerating and retarding Lorentz force cases, the error in the turbulent kinetic energy and Reynolds stress plots was numerically estimated to be about ± 10 %. It was hoped that a retarding Lorentz force would be noticed in

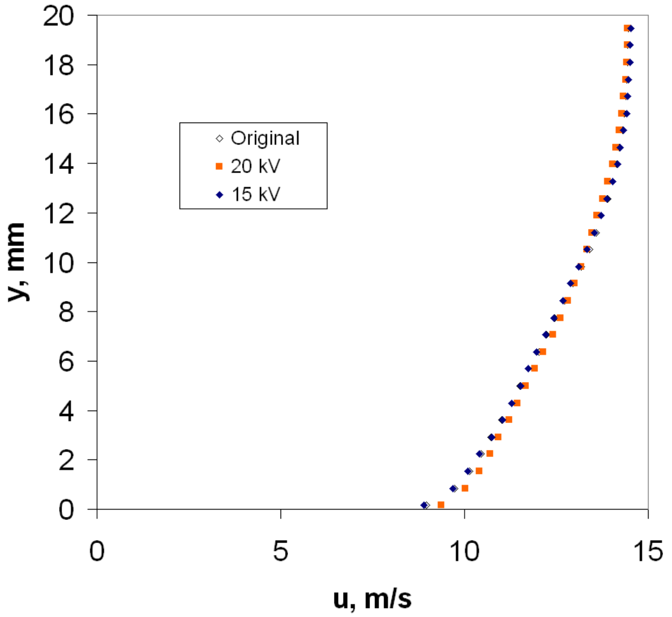

Figure 7.16. Boundary layer profiles for the 15 and 20 kV EMFC cases as compared to the original profile for the retarding Lorentz force direction experiments.

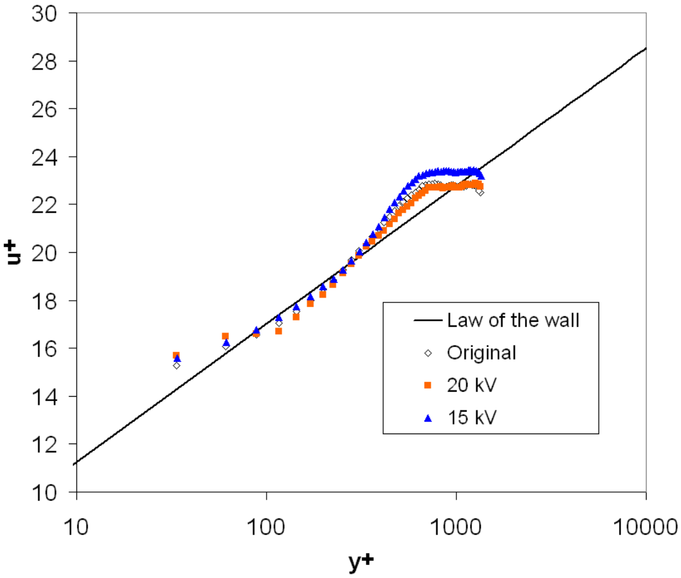

Figure 7.17. Boundary layer profiles for the 15 and 20 kV EMFC cases as compared to the original profile and the law-of-the-wall profile for the retarding Lorentz force direction experiments.

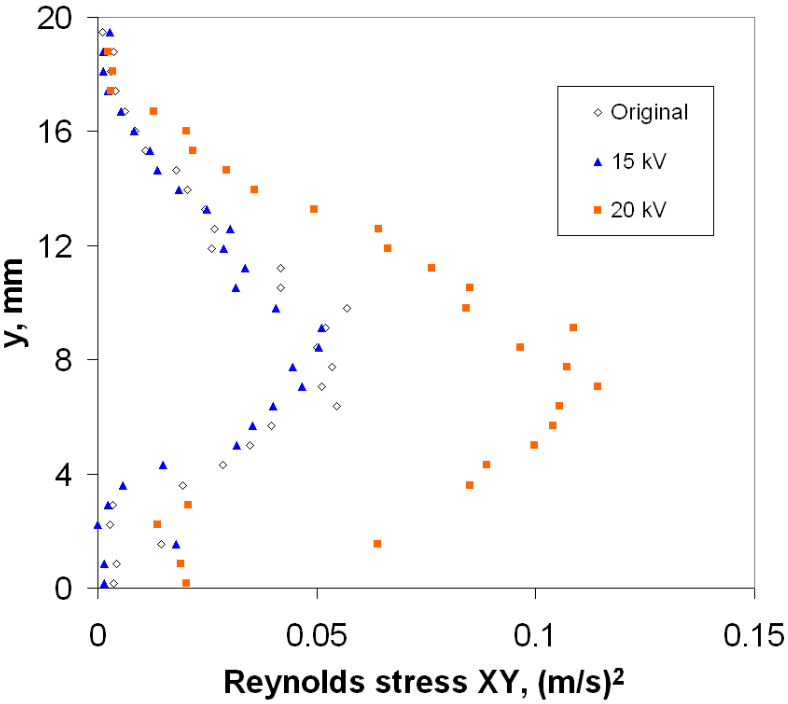

Figure 7.18. Reynolds stress profiles for the 15 and 20 kV EMFC cases as compared to the original profile for the retarding Lorentz force direction experiments.

these profiles, whereby the magnitudes of the Reynolds stress and turbulent kinetic energy would trend in opposite directions as the potential difference applied to the actuator was increased. In the 20 kV case for this data, the turbulent kinetic energy and Reynolds stresses are noticeable increased, probably because of the larger power input (16 W to 10 W). However, this increase trends similarly to the acceleration Lorentz force direction cases, so an assumption that the Lorentz force has been detected cannot be made.

7.5.3 Comparison of Results

A comparison of the accelerating and retarding Lorentz force direction data shows that indeed no Lorentz force is detectable. The lack of a force is primarily due to a lack of energy deposition because conductivity is very low and a lack of a stronger

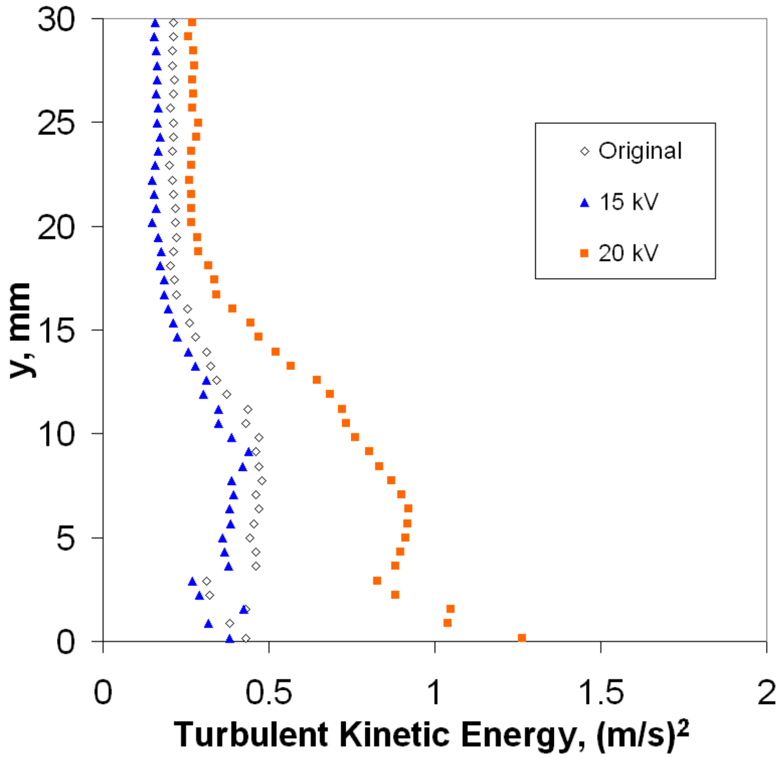

Figure 7.19. Turbulent kinetic energy profiles for the 15 and 20 kV EMFC cases as compared to the original profile for the retarding Lorentz force direction experiments.

magnet. Previous studies outlined in the review show that the presence of a magnet can both disturb the uniform nature of a glow discharge and affect the plasma control effect. Those studies were benefited by using more powerful electromagnets and lower static test section pressure. Any changes in the boundary layer profile, Reynolds stress, or turbulent kinetic energy appear to be due to Joule heating (particularly from the periodic arc discharges in the 20 kV data).

Figure 7.20 compares the 20 kV accelerating and retarding cases along with their original boundary layer profiles using law-of-the-wall coordinates. The profiles are strikingly similar, indicating good agreement between the original boundary layers which both converged around the law-of-the-wall equation using $c_f = 0.00385$. The

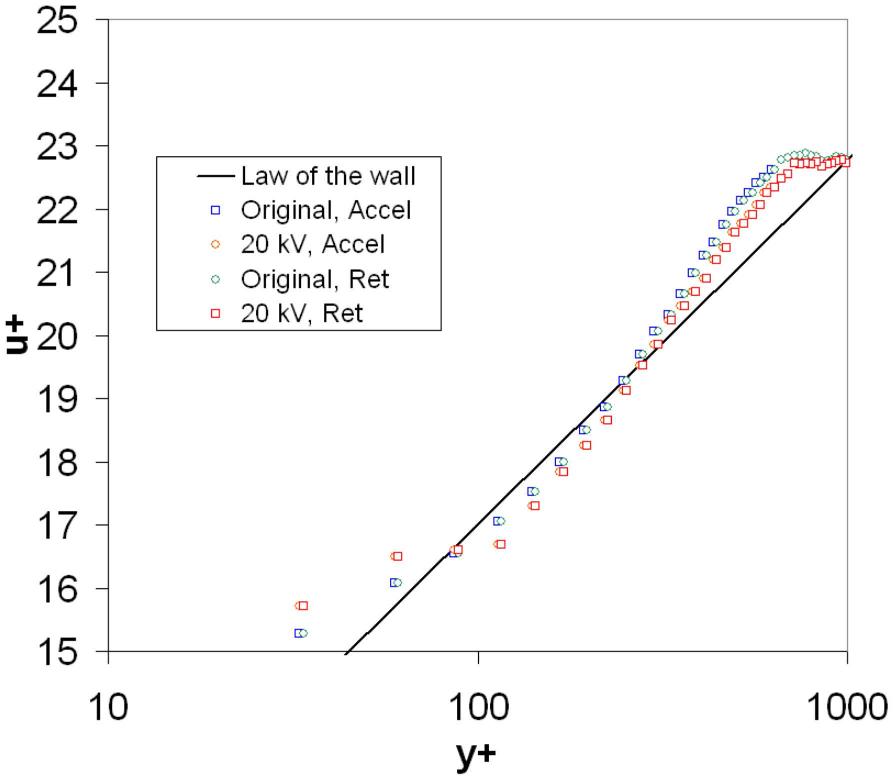

Figure 7.20. Law-of-the-wall comparison between 20 kV accelerating and retarding Lorentz force cases.

changes to the profiles caused by the 20 kV cases indicate no dependency on the direction of the Lorentz force.

CHAPTER 8

CONCLUSIONS

Great interest lies in the ability to create highly conductive, stable plasma in an atmospheric pressure environment. In addition to many industrial applications, highly conductive, low temperature plasma is needed for EMFC actuators in order to increase the energy addition into the airflow. Ground testing of EMFC actuators particularly for boundary-layer control is not a simple experimental procedure. The few successful facilities presented in the review portion of this thesis are small scale, make use of electromagnetic pieces of equipment that likely cannot be placed onto a flight vehicle, use very low static pressure to raise the electromagnetic interaction parameters, and offer limited data on the changes to the boundary layer itself.

In the experimental portion of this thesis, a low-speed EMFC facility was constructed to test different methods of injecting seed particles in the airflow whereby they would be ionized before passing over a Lorentz force actuator. These efforts, in addition to using conductive metal powder and aqueous salt sprays, did not yield any appreciable results that can be used for on-board vehicle control. Several recommendations are therefore given in the next section on how to improve particle seeding and which applications it appears feasible for.

Another goal of this study was to demonstrate that compact EMFC actuators can be used in place of those utilizing electromagnets or superconducting magnets. Although little experimental information is available to clearly establish if the concept is feasible, it appears that a large level of energy can be placed into the airflow as shown by the computational MHD program for bulk conductivity on the order of 1

℧/m. Several recommendations for future research in this field are laid out in the final two sections.

8.1 Feasibility of Particle Seeding

To begin this section, the feasibility of having separate ionization and EMFC plate components must be addressed. Even when the ionization plate was actuated with an aqueous salt spray, the EMFC actuator did not receive any charged particles and no current was drawn from its power supply. Especially at low freestream speeds, ionized heavy radicals or a glow discharge is not going to convect downstream. Even if the convection were to occur, it would result in a conductive bridge between both sets of electrodes which would likely have adverse effects. Diodes could mitigate most of the interaction issues, but experimental measurements of voltage and current would probably be more difficult on the grounded side of a circuit. Floating the grounds of each supply can prevent some of these problems, but the presence of a conductive path between the ionization and Lorentz force electrodes would still prevent energy deposition from the lower voltage Lorentz force actuator electrodes.

The solution to this problem is to combine each of the actuators into one set of electrodes using a circuit shown in Fig. 8.1. In this circuit, a high voltage power supply capable of creating ionization over the plate would be attached to the same electrodes as another low voltage supply. The low voltage supply can facilitate energy addition into the flow so long as a conductive working fluid remains on the surface of the actuator. The high voltage power supply can operate with a low duty-cycle square wave allowing for energy addition to take place during most of the operating time. The frequency of the square wave is then dictated by the decay rate of the plasma in that it is sufficiently high enough to counteract that decay. Some of these principles have already been proven in [39, 40], and the difference for this compact

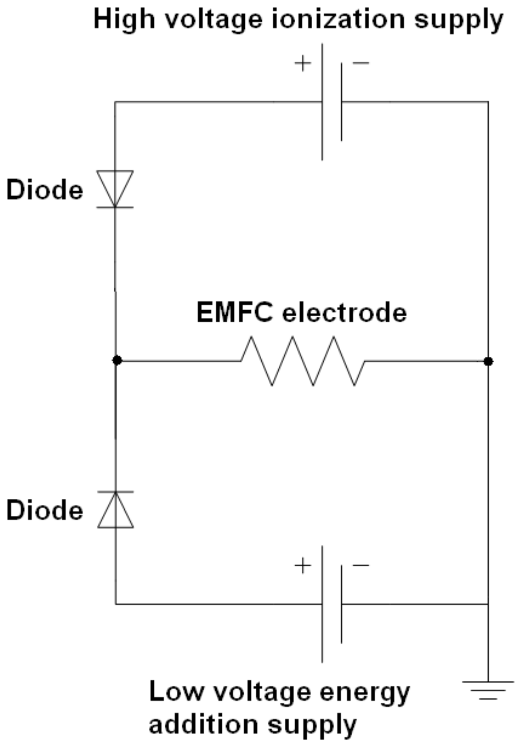

Figure 8.1. Circuit diagram for a combined ionization/Lorentz force flat plate EMFC actuator.

EMFC actuator with respect to those studies is the electrodes are shared by the power supplies, the ionization voltage must be a square wave, and diodes must be built into the circuit.

Although the above system should be much improved for compact, flat plate EMFC actuators, a power supply like the 20 kVDC Glassman system which has a maximum current draw of 15 mA is still not sufficient for ionizing dry seed particles. Ionization of potassium carbonate and other alkali salts appears to only be effective in high temperature environments because the energy of the flow effectively vaporizes the seed. Although the seed particles used visually appear to be no larger than dust, they were in some cases over one million times larger than the component molecules of air. It seems that, despite the fact that potassium carbonate may have an ionization energy value lower than that of diatomic oxygen, the energy required to ionize these vastly larger particles is simply not present in an ambient temperature glow discharge. Consequently, the high voltage component of the circuit in Fig. 8.1 must also provide high current with the high voltage during the low duty-cycle pulse, possibly by means of a capacitor or more elaborate circuit components.

Drawing conclusions on the feasibility of different seeding attempts, it appears that the injection of alkali salts is not practical for low temperature or low speed applications. The seed particles are simply too large for a low power glow discharge to break down. The alkali salt seed particles may be useful for increasing boundary layer conductivity if high voltage, high current ionization pulses contain enough energy to vaporize the seed. The high voltage ionization system shown in [39, 40] might be capable of breaking down these particles, but no data thus far can serve as a proof-of-concept.

Although EMFC via the Lorentz force is easily demonstrated in salt water channels, spraying an aqueous solution over the surface of an EMFC actuator is rather impractical. The solution tends to build on the surface even with air flow, and the salt can build up on the optical walls of the tunnels. This problem is exacerbated when considering the wind tunnel used for this study employs a closed circuit. Perhaps experiments in a supersonic blowdown wind tunnel environment will eliminate the salt buildup on the surface. That fact that the PIV seeder, which can convert the potassium carbonate and water mixture into an aerosol spray of ≈ 1 μm particles, was not able to actuate the EMFC plate with a potential difference of a few hundred volts was disappointing.

Seeding the airflow with metal powder probably should have been more extensively investigated for this study. Although many powdered metals do not meet the requirements for EMFC, those that do could be purchased in nanoparticle form and the experiments could be run again. However, the seed distribution must be very uniform at atmospheric pressure or else the only results may be arcing. As was already stated, the cost of these particles is also a factor as a large amount of seed is consumed during the wind tunnels tests.

8.2 Feasibility of a Compact Actuator

Discussing the prospects of compact EMFC actuators employing NdFeB magnets and electrodes in the manner of this study is an interesting topic. It can be argued that compact actuators with NdFeB magnets need to be feasible for control surface aerodynamics applications since EMFC with electromagnets and superconducting magnets result in systems that have too much mass to be placed within a flight vehicle. If the concept is not feasible, then potential electromagnetic control surfaces will be inferior when compared to plasma control surfaces.

Concerning low-speed EMFC testing, it appears that glow discharges and particularly dielectric barrier discharges are suitable for control over EMFC actuators. Even if the seed particle ionization attempts had been successful, the high value of the MHD loading parameter as shown in Fig. 5.18 means that most of the energy addition would result in Joule heating and not Lorentz force acceleration or retardation. Recalling that the physical meaning of the MHD loading parameter is a ratio of the power per unit volume to the directed kinetic energy from the actuator, values over 100 indicate very low efficiency. Typical MHD loading parameters that have been able to distinguish between Joule heating and the Lorentz force are usually less than 100, and a 100 V electrode potential difference using the actuator in this study with a freestream speed of 14 m/s yields an averaged boundary layer value of about 3000. Practical EMFC actuator testing simply is meant for environments with higher speeds and lower pressure/density (I_{EM}), which is actually a good trend considering that the rapid actuation offered by such actuators is most needed for high speed, high altitude aerodynamic control. For a nominal potential difference of 100 V, the EMFC actuator in this study requires a freestream of at least Mach 1.5 before a Lorentz force will probably be distinguishable from Joule heating.

If further tests are to be conducted as part of this research effort, it is recommended that they take place in an environment of supersonic flow with a Mach number of preferably 3–4 to maximize efficiency and so the test section static pressure can be reduced to about 0.3 atm. The energy addition into the supersonic flow will have to be in the range of 1–20 kW, creating a need to switch the materials to a ceramic base (possibly boron nitride) and electrodes machined from stainless steel or tungsten. The NdFeB magnets will probably also need a high pressure water cooling system. It is additionally recommended that replica actuators are built that do not contain embedded magnets. In other studies with electromagnets, the field can be reduced to 0 T to see the effects of using only plasma, but that was not possible with these actuators. To facilitate energy transfer, the magnets and electrodes should be scaled to a smaller size and placed closer to one another. Consequently, the potential difference of the electrodes may then be lowered which will also improve efficiency. With low duty-cycle ionization by increasingly improved high voltage circuit technology that can vaporize low ionization energy seed particles, it is conceivable that the Lorentz force actuator potential difference can be lowered such that an efficient EMFC control surface can be constructed.

APPENDIX A

LORENTZ FORCE POWER SUPPLY DESIGN

The design of the Lorentz force power supply was based upon several factors. First, from the optimization of the actuator, it was determined that the electrode potential would have to be several hundred volts. In order to perform parametric studies of the actuator, the potenial would also have to be variable. Most likely, the power consumption of a feasible actuator at low speeds should only be a few hundred watts. However, in order to complete supersonic tests at similar values of I_{EM}, up to ten kilowatts of power would be needed for every electrode with an applied potential. An array of B. B. Battery HR9-12 high-rate motorcycle batteries was chosen, resulting in a cost effective power supply. The maximum electrode potential was set at 600 V since it is the limit for general purpose wire. The high rate batteries contain tabs that connect to gauge 10 wire. Therefore, 150 batteries were purchased and assembled into fifteen 120 V modular units with the intention of using up to five over three separate electrodes. They were assembled with interchangeable connector plates for use in series or charging in parallel. The current was limited to 20 A by a circuit breaker. Additionally, high power load resistors were purchased and may be placed in different configurations to further limit the current draw. Potentials of 120, 240, 360, 480, and 600 V may be applied to the electrodes. The maximum output of this system was 36 kW.

For safety, operation of the power supply was controlled using LabVIEW. To control such power with a computer, an analog control voltage signal was first passed to a set of three voltage comparators labeled C1, C2, and C3 in Fig. A.1. The three comparators corresponded to the three electrodes that can be used for the Lorentz force acutator. The comparator reference voltages were set in numerical order so an increasing control voltage signal sent from LabVIEW will activate the electrodes one by one. Reference voltages were established by using a dedicated 24 VDC power supply connected to three potentiometers (P1 = 1 V, P2 = 4 V, and P3 = 7 V).

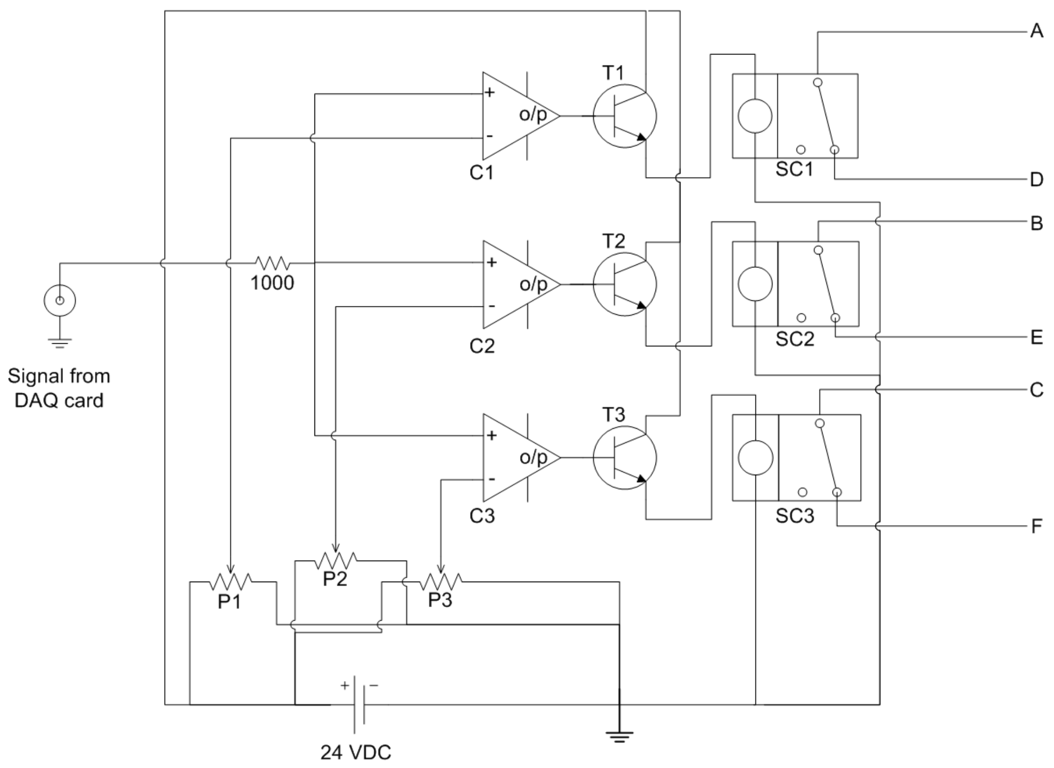

Figure A.1. Analog control circuit design of the Lorentz force actuator power supply.

For example, if the LabVIEW control voltage was set to 5 V, two electrodes will be activated. After the comparators, low power Darlington transistors (T1, T2, and T3) were used to activate 24 VDC SPDT relays (SC1, SC2, and SC3), which in turn activated 24 VAC SPST contactors (C1, C2, and C3 in Fig. A.2) in line with the main power supply for each electrode. The 24 VAC SPST contactors selected were typically used for air conditioning systems and can manage 12 kW each. They required a separate power supply, constructed using a 120 VAC power outlet and an autotransformer. Using a Hall effect current sensor that transferred 0–20 A into a 0–10 V analog signal, the LabVIEW control program also acted as a circuit breaker by deactivating the relays if the current passed a user-specified maximum value.

Figure A.3 depicts one of the 120 V modular battery supplies used for the actuator circuit. The photgraph shows a dissasembled module with parallel (left)

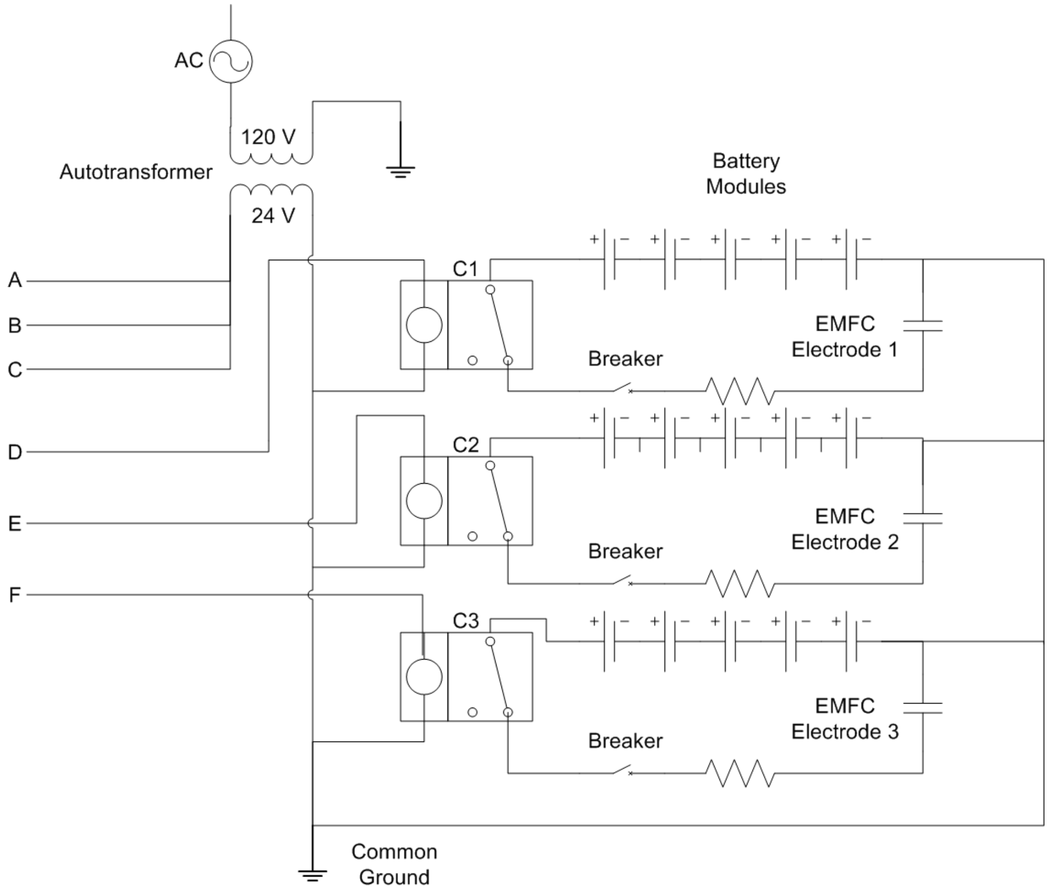

Figure A.2. Power electronics circuit design of the Lorentz force actuator power supply.

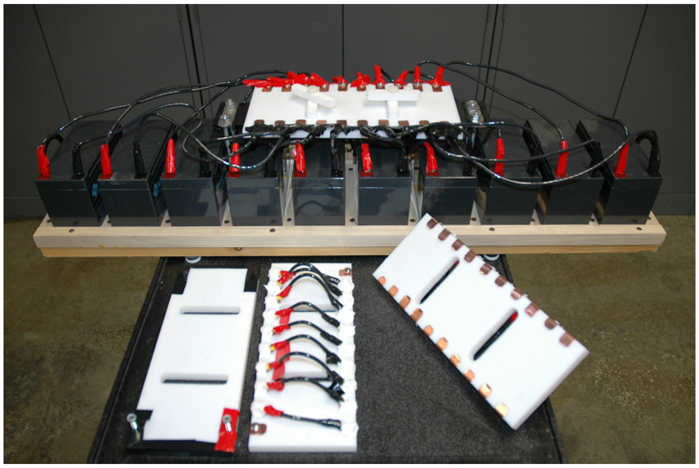

Figure A.3. Photograph of a 120 V modular battery supply.

and series (center and right) interchangeable connector plates placed in front of it. Corresponding copper electrodes are pressed onto each other as two teflon tabs on the main plate are tightened. All of the modules and the LabVIEW interface circuit have been placed onto a mobile cart. The entire fifteen module assembly consists of approximately four thousand individual components.

REFERENCES

[1] M. Nishihara, J. W. Rich, W. R. Lempert, and I. V. Adamovich, "Low-temperature M = 3 flow deceleration by Lorentz force," 2006, paper AIAA 2006-1004.

[2] J.-P. Thibault and L. Rossi, "Electromagnetic flow control: Characteristic numbers and flow regimes of a wall-normal actuator," *Journal of Physics D: Applied Physics*, vol. 36, no. 20, pp. 2559–2568, 2003.

[3] J. R. Roth, H. Sin, R. C. M. Madhan, and S. P. Wilkinson, "Flow re-attachment and acceleration by paraelectric and peristaltic electrohydrodynamic (EHD) effects," 2003, paper AIAA 2003-0531.

[4] J. Menart, J. Shang, C. Atzbach, S. Magoteaux, M. Slagel, and B. Bilheimer, "Total drag and lift measurements in a Mach 5 flow affected by a plasma discharge and a magnetic field," 2005, paper AIAA 2005-0947.

[5] J. Liu and M. Walmer, "Designing with high performance rare earth permanent magnets," in *Proceedings of the 18th International Workshop on High Performance Magnets and Their Applications*, 2004, pp. 630–636.

[6] A. J. Williams, R. Walls, B. E. Davies, J. Marchese, and I. R. Harris, "A study of thermal demagnetisation behaviour of Nd-Fe-B sintered magnets by a magnetic field mapping system," *Journal of Magnetism and Magnetic Materials*, vol. 242-245, pp. 1378–1380, 2002.

[7] J. S. Shang, P. G. Huang, H. Yan, S. T. Surzhikov, and D. V. Gaitonde, "Hypersonic flow control utilizing electromagnetic-aerodynamic interaction," 2008, paper AIAA 2008-2606.

[8] M. Nishihara, J. W. Rich, W. R. Lempert, and I. V. Adamovich, "MHD flow control and power generation in low-temperature supersonic flows," 2006, paper AIAA 2006-3076.

[9] H. Lowry, C. Stepanek, L. Crosswy, P. Sherrouse, M. Smith, L. Price, W. Ruyten, and J. Felderman, "Shock structure of a spherical projectile in weakly ionized air," 1999, paper AIAA 1999-0600.

[10] J. R. Roth, R. C. M. Madhan, M. Yadav, J. Rahel, and S. P. Wilkinson, "Flow field measurements of paraelectric, parastaltic, and combined plasma actuators based on the one atmosphere uniform glow discharge plasma (OAUGDP$^{\text{TM}}$)," 2004, paper AIAA 2004-0845.

[11] C. L. Enloe, T. E. McLaughlin, R. D. VanDyken, K. D. Kachner, E. J. Jumper, T. C. Corke, M. Post, and O. Haddad, "Mechanisms and responses of a single dielectric barrier plasma actuator: Geometric effects," *AIAA Journal*, vol. 42, no. 3, pp. 595–604, 2004.

[12] G. W. Sutton and A. Sherman, *Engineering magnetohydrodynamics.* New York, NY: McGraw-Hill, 1965.

[13] R. L. Resler and W. R. Sears, "The prospects for magneto-aerodynamics," *Journal of the Aeronautical Sciences*, vol. 25, no. 4, pp. 235–245,258, 1958.

[14] L. E. Rittenhouse, J. C. Pigott, J. M. Whoric, and D. R. Wilson, "Theoretical and experimental results with a linear magnetohydrodynamic accelerator operated in Hall current neutralized mode," Arnold Air Force Station, TN, Tech. Rep. AEDC-TR-67-150, Nov. 1967.

[15] R. J. Rosa, "Part one: Shock wave spectroscopy. Part two: Engineering magneto-hydrodynamics," Ph.D. Dissertation, Cornell University, Ithica, NY, 1956.

[16] R. M. Patrick, “Magneto-hydrodynamics of compressible fluids,” Ph.D. Dissertation, Cornell University, Ithica, NY, 1956.

[17] G. A. Simmons and G. L. Nelson, “Overview of the NASA MARIAH project and summary of technical results,” 1998, paper AIAA 1998-2752.

[18] E. P. Gurijanov and P. T. Harsha, “AJAX: New directions in hypersonic technology,” 1996, paper AIAA 1996-4609.

[19] A. L. Kuranov and E. G. Sheikin, “Magnetohydrodynamic control on hypersonic aircraft under “AJAX” concept,” *Journal of Spacecraft Rockets*, vol. 40, no. 2, pp. 174–182, 2003.

[20] S. O. Macheret, M. N. Schneider, R. B. Miles, and R. J. Lipinski, “Electron-beam-generated plasmas in hypersonic magnetohydrodynamic channels,” *AIAA Journal*, vol. 39, no. 6, pp. 1127–1138, 2001.

[21] G. E. Caledonia, J. C. Person, and D. Hastings, “Ionization phenomena about the space shuttle,” Physical Sciences, Inc., MA, Tech. Rep. AFGL-TR-86-0045, Jan. 1986.

[22] A. C. Holt, “Electromagnetic braking for Mars spacecraft,” 1986, paper AIAA 1986-1588.

[23] T. Tanifuji, A. Matsuda, K. Wasai, H. Otsu, H. Yamasaki, D. Konigorski, and T. Abe, “Expansion tube experiment of applied magnetic field effect on reentry plasma,” 2008, paper AIAA 2008-1113.

[24] P. Palm, R. Meyer, E. Ploenjes, A. Bezant, I. V. Adamovich, J. W. Rich, and S. Gogineni, “MHD effect on a supersonic weakly ionized flow,” 2002, paper AIAA 2002-2246.

[25] S. O. Macheret, M. N. Schneider, and R. B. Miles, “Modeling of plasma generation in repetitive ultra-short DC, microwave, and laser pulses,” 2001, paper AIAA 2001-2940.

[26] J. S. Shang, “Recent research in magneto-aerodynamics,” *Progress in Aerospace Sciences*, vol. 37, no. 1, pp. 1–20, 2001.

[27] C. Bruno, P. A. Czysz, and S. N. B. Murthy, “Electro-magnetic interaction in a hypersonic propulsion system,” 1997, paper AIAA 1997-3389.

[28] C. Park, U. B. Mehta, and D. W. Bogdanoff, “Magnetohydrodynamics energy bypass scramjet performance with real gas effects,” *Journal of Propulsion and Power*, vol. 17, no. 5, pp. 1049–1057, 2001.

[29] J. R. Roth, “Aerodynamic flow acceleration using paraelectric and paristaltic electrohydrodynamic effects of a one atmosphere uniform glow discharge plasma,” *Physics of Plasmas*, vol. 10, no. 5, pp. 2117–2126, 2003.

[30] R. F. Harrington, *Introduction to electromagnetic engineering.* New York, NY: McGraw-Hill, 1958.

[31] W. B. Ericson and A. Maciulaitis, “Investigation of magnetogasdynamic flight control,” *Journal of Spacecraft and Rockets*, vol. 1, no. 3, pp. 283–289, 1964.

[32] W. M. Elsasser, “Dimensional relations in magnetohydrodynamics,” *Physical Review*, vol. 95, no. 1, pp. 1–5, 1954.

[33] R. Meyer, M. Nishihara, A. Hicks, N. Chintala, M. Cundy, W. R. Lempert, I. V. Adamovich, and S. Gogineni, “Measurements of flow conductivity and density fluctuations in supersonic nonequilibrium magnetohydrodynamic flows,” *AIAA Journal*, vol. 43, no. 9, pp. 1923–1929, 2005.

[34] C. Henoch and J. Stace, “Experimental investigation of a salt water turbulent boundary layer modified by an applied streamwise magnetohydrodynamic body force,” *Physics of Fluids*, vol. 7, no. 6, pp. 1371–1383, 1995.

[35] S. O. Macheret, M. N. Shneider, and R. B. Miles, “Magnetohydrodynamic and electrohydrodynamic control of hypersonic flows of weakly ionized plasmas,” *AIAA Journal*, vol. 42, no. 7, pp. 1378–1387, 2004.

[36] R. Munipalli, *Code to compute magnetic field components in a 2D domain with a periodic array of magnets*, Hypercomp, Inc., Westlake Village, CA, 2007.

[37] Z. N. Celinski and F. W. Fischer, “Effect of electrode size in MHD generators with segmented electrodes,” *AIAA Journal*, vol. 4, no. 3, pp. 421–428, 1966.

[38] D. D’Ambrosio and D. Giordano, “Electromagnetic fluid dynamics for aerospace applications. Part I: Classification and critical review of physical models,” 2004, paper AIAA 2004-2165.

[39] M. Nishihara, N. Jiang, J. W. Rich, W. R. Lempert, I. V. Adamovich, and S. Gogineni, “Low-temperature supersonic boundary layer control using repetitively pulsed magnetohydrodynamic forcing,” *Physics of Fluids*, vol. 17, no. 10, p. DOI: 10.1063/1.2084227, 2005.

[40] M. Nishihara, J. W. Rich, W. R. Lempert, I. V. Adamovich, and S. Gogineni, “Low-temperature M = 3 flow deceleration by Lorentz force,” *Physics of Fluids*, vol. 18, no. 8, p. DOI: 10.1063/1.2265011, 2006.

[41] P. Palm, R. Meyer, A. Bezant, I. V. Adamovich, J. W. Rich, and S. Gogineni, “Feasibility study of MHD control of cold supersonic plasma flows,” 2002, paper AIAA 2002-0636.

[42] R. L. Kimmel, S. Gogineni, I. V. Adamovich, J. W. J. W. Rich, and X. Zhong, “Update on MHD control of supersonic/hypersonic boundary-layer transition,” 2003, paper AIAA 2003-6924.

[43] R. Meyer, B. McEldowney, N. Chintala, I. V., and Adamovich, “Measurements of electrical parameters of a supersonic nonequilibrium MHD channel,” 2003, paper AIAA 2003-4279.

[44] M. Nishihara, R. Meyer, M. Cundy, W. R. Lempert, and I. V. Adamovich, “Development and operation of a supersonic nonequilibrium MHD channel,” 2004, paper AIAA 2004-2441.

[45] M. Nishihara, N. Jiang, W. R. Lempert, I. V. Adamovich, and S. Gogineni, "MHD supersonic boundary layer control using pulsed discharge ionization," 2005, paper AIAA 2005-1341.

[46] M. Nishihara, J. Bruzzese, I. V. Adamovich, K. Udagawa, and D. Gaitonde, "Experimental and computational studies of low-temperature M = 4 flow deceleration by Lorentz force," 2007, paper AIAA 2007-4595.

[47] S. H. Zaidi, T. Smith, S. O. Macheret, and R. B. Miles, "Snowplow surface discharge in magnetic field for high speed boundary layer control," 2006, paper AIAA 2006-1006.

[48] C. S. Kalra, S. H. Zaidi, and R. B. Miles, "Shockwave induced turbulent boundary layer separation control with plasma actuators," 2008, paper AIAA 2008-1092.

[49] J. S. Shang, R. Kimmel, J. Hayes, C. Tyler, and J. Menart, "Hypersonic experimental facility for magnetoaerodynamic interactions," *Journal of Spacecraft and Rockets*, vol. 42, no. 5, pp. 780–789, 2005.

[50] J. S. Shang, J. R. Hayes, J. H. Miller, and J. A. Menart, "Magneto-aerodynamic interactions in weakly ionized hypersonic flow," 2002, paper AIAA 2002-0349.

[51] R. L. Kimmel, J. R. Hayes, J. A. Menart, and J. S. Shang, "Effect of magnetic fields on surface plasma discharges at Mach 5," *Journal of Spacecraft and Rockets*, vol. 43, no. 6, pp. 1340–1346, 2006.

[52] O. M. Phillips, "The prospects for magnetohydrodynamic ship propulsion," *Journal of Ship Research*, vol. 6, pp. 43–51, 1962.

[53] S. Way, "Electromagnetic propulsion for cargo submarines," *Journal of Hydronautics*, vol. 2, no. 2, pp. 49–57, 1968.

[54] S. Takezawa, H. Tamama, K. Sugawawa, H. Sakai, C. Matsuyama, H. Morita, H. Suzuki, Y., and Ueyama, "Operation of the thruster for superconducting

electromagnetohydrodynamic propulsion ship Yamato 1," *Bulletin of the Marine Engineering Society of Japan*, vol. 23, no. 1, pp. 46–55, 1995.

[55] D. W. Cott, V. W. Daniel, R. A. Carrington, and J. S. Herring, "MHD propulsion for submarines," MSE, Inc., MT, Tech. Rep. 2DOE-MHD-D140, Oct. 1988.

[56] T. C. Corke and M. L. Post, "Overview of plasma flow control: Concepts, optimization, and applications," 2005, paper AIAA 2005-0563.

[57] C. L. Enloe, T. E. McLaughlin, R. D. VanDyken, K. D. Kachner, E. J. Jumper, and T. C. Corke, "Mechanisms and responses of a single dielectric barrier plasma actuator: Plasma morphology," *AIAA Journal*, vol. 42, no. 3, pp. 589–594, 2004.

[58] B. Jayaraman, Y. Lian, and W. Shyy, "Low-reynolds number flow control using dielectric barrier discharge actuators," 2007, paper AIAA 2007-3974.

[59] E. L. Fleeman, *Tactical missile design, 2nd ed.* Reston, VA: AIAA Education Series, 2006.

[60] K.-H. Muller, G. Krabbes, J. Fink, S. Gruß, A. Kirchner, G. Fuchs, and L. Schultz, "New permanent magnets," *Journal of Magnetism and Magnetic Materials*, vol. 226-230, no. 2, pp. 1370–1376, 2001.

[61] *Standard Specifications for Permanent Magnet Materials*, Magnetic Materials Producers Association Std. MMPA 0100-00, 2000.

[62] G. C. Hadjipanayis, J. Liu, A. Gabay, and M. Marinescu, "Current status of rare-earth permanent magnet research in USA," *Journal of Iron and Steel Research, International*, vol. 13, pp. 12–22, 2006.

[63] J. F. Liu and M. H. Walmer, "Thermal stability and performance data for SmCo 2:17 high-temperature magnets on ppm focusing structures," *IEEE Transactions on Electronic Devices*, vol. 52, no. 5, pp. 899–902, 2005.

[64] J. Liu, P. Vora, P. Dent, M. Walmer, C. Chen, J. Talnagi, S. Wu, and M. Harmer, "Thermal stability and radiation resistance of Sm-Co based per-

manent magnets," in *Proceedings of the Space Nuclear Conference 2007*, 2007, paper 2036.

[65] J. Liu, P. Vora, and M. Walmer, "Overview of recent progress in Sm-Co based magnets," *Journal of Iron and Steel Research, International*, vol. 13, pp. 319–323, 2006.

[66] G. W. Garrison, "Electrical conductivity of a seeded nitrogen plasma," *AIAA Journal*, vol. 6, no. 7, pp. 1264–1270, 1968.

[67] R. G. Jahn, *Physics of electric propulsion*. New York, NY: McGraw-Hill, 1968.

[68] G. M. Giannini, "The plasma jet and its application," Office of Scientific Research, Tech. Rep. 57-520, 1957.

[69] A. R. Kantrowitz, "Introducing magnetohydrodynamics," *Astronautics*, vol. 3, no. 10, pp. 18–20, 74–77, 1958.

[70] L. S. Frost, "Conductivity of seeded atmospheric pressure plasmas," *Journal of Applied Physics*, vol. 32, no. 10, pp. 2029–2036, 1961.

[71] D. J. BenDaniel and C. M. Bishop, "Nonequilibrium ionization in a high-pressure cesium-helium transient discharge," *Physics of Fluids*, vol. 6, no. 2, pp. 300–306, 1963.

[72] E. E. Zukoski, T. A. Cool, and E. G. Gibson, "Experiments concerning nonequilibrium conductivity in a seeded plasma," *AIAA Journal*, vol. 2, no. 8, pp. 1410–1417, 1964.

[73] T. A. Cool and E. E. Zukoski, "Recombination, ionization, and nonequilibrium electrical conductivity in seeded plasmas," *Physics of Fluids*, vol. 9, no. 4, pp. 780–796, 1966.

[74] G. Brederlow and R. T. Hodgson, "Electrical conductivity in seeded noble gas plasmas in crossed electric and magnetic fields," *AIAA Journal*, vol. 6, no. 7, pp. 1277–1284, 1968.

[75] T. K. Chu and C. F. Gottschlich, “Temperature measurement of an alkali metal-seeded plasma in an electric field,” *AIAA Journal*, vol. 6, no. 1, pp. 114–119, 1968.

[76] S. Schweitzer, “Tensor electrical conductivity of atmospheric cesium-seeded argon,” *AIAA Journal*, vol. 5, no. 5, pp. 844–847, 1967.

[77] J. R. Viegas and C. H. Kruger, “Effect of multispecies ionization on electrical conductivity calculations,” *AIAA Journal*, vol. 6, no. 6, pp. 1193–1195, 1968.

[78] F. K. Lu, H. C. Liu, and D. R. Wilson, “Electrical conductivity channel for a shock tube,” *Measurement Science and Technology*, vol. 16, no. 9, pp. 1730–1740, 2005.

[79] B. C. Hacker, “Whoever heard of nuclear-powered ramjets? Project Pluto at Livermore and the Nevada test site, 1957-64,” *Journal of the International Committee for the History of Technology*, vol. 1, pp. 85–98, 1995.

[80] R. Nowak, S. Kranc, R. W. Porter, M. C. Tuen, and A. B. Cambel, “Magnetogasdynamic re-entry phenomena,” *Journal of Spacecraft and Rockets*, vol. 4, no. 11, pp. 1538–1542, 1967.

[81] G. A. Simmons, G. L. Nelson, and C. A. Ossello, “Electron attachment in seeded air for hypervelocity MHD accelerator propulsion wind tunnel applications,” 1998, paper AIAA 1998-3133.

[82] D. G. Elliot, “Magnetohydrodynamic power systems,” *Journal of Spacecraft and Rockets*, vol. 4, no. 7, pp. 842–846, 1967.

[83] H. K. Messerle, *Magnetohydrodynamic Electrical Power Generation.* New York, NY: John Wiley and Sons, 1995.

[84] W. R. Mickelsen, “Auxiliary and primary electric propulsion, present and future,” *Journal of Spacecraft and Rockets*, vol. 4, no. 11, pp. 1409–1423, 1967.

[85] R. A. Becker, “Thermionic space power systems review,” *Journal of Spacecraft and Rockets*, vol. 4, no. 7, pp. 847–851, 1967.

[86] C. S. Kalra, S. H. Zaidi, B. Alderman, and R. B. Miles, “Non-thermal control of shock-wave induced boundary layer separation using magneto-hydrodynamics,” 2007, paper AIAA 2007-4138.

[87] C. S. Kalra, S. H. Zaidi, B. Alderman, R. B. Miles, and Y. V. Murty, “Magnetically driven surface discharges for shock-wave induced boundary-layer separation control,” 2007, paper AIAA 2007-0222.

[88] J. A. Menart and J. S. Shang, “Investigation of effects caused by a pulsed discharge and a magnetic field in a Mach 5 flow,” 2005, paper AIAA 2005-4783.

[89] A. von Engel, *Ionized gases.* London: Oxford University Press, 1955.

[90] A. Fridman, A. Chirokov, and A. Gutsol, “Non-thermal atmospheric pressure discharges,” *Journal of Physics D: Applied Physics*, vol. 38, no. 2, pp. R1–R24, 2005.

[91] J. D. Cobine, *Gaseous Conductors: theory and engineering applications.* New York, NY: Dover, 1958.

[92] P. Bletzinger, B. N. Ganguly, D. V. Wie, and A. Garscadden, “Plasmas in high speed aerodynamics,” *Journal of Physics D: Applied Physics*, vol. 38, no. 4, pp. R33–R57, 2005.

[93] R. W. Ziemer, “Experimental investigation in magneto-aerodynamics,” *ARS Journal*, vol. 19, pp. 642–647, 1959.

[94] A. I. Klimov, A. N. Koblov, G. I. Mishin, Y. L. Serov, and I. P. Yavor, “Shock wave propagation in a glow discharge,” *Soviet Technical Physics Letters*, vol. 8, no. 4, pp. 192–194, 1982.

[95] V. A. Gorshkov, A. I. Klimov, G. I. Mishin, A. B. Fedotov, and I. P. Yavor, “Behavior of electron density in weakly ionized nonequilibrium plasma with a

propagating shock wave," *Soviet Technical Physics Letters*, vol. 57, pp. 1138–1141, 1987.

[96] A. I. Klimov, G. I. Mishin, A. B. Fedotov, and V. A. Shakhovatov, "Shock wave propagation in a nonstationary glow discharge," *Soviet Technical Physics Letters*, vol. 15, pp. 800–802, 1989.

[97] J. Poggie, "DC glow discharge: A computational study for flow control applications," 2005, paper AIAA 2005-5303.

[98] J. Shin, V. Narayanaswamy, L. L. Raja, and N. T. Clemens, "Characterization of a direct-current glow discharge plasma actuator in low-pressure supersonic flow," *AIAA Journal*, vol. 45, no. 7, pp. 1596–1605, 2007.

[99] J. Menart, S. Henderson, C. Atzbach, J. Shang, R. Kimmel, and J. Hayes, "Study of surface and volumetric heating effects in a Mach 5 flow," 2004, paper AIAA 2004-2262.

[100] S. Merriman, E. Ploenjes, P. Palm, and I. V. Adamovich, "Shock wave control by nonequilibrium plasmas in cold supersonic gas flows," *AIAA Journal*, vol. 39, no. 8, pp. 1547–1552, 2001.

[101] P. Gnemmi, R. Charon, J. P. Duperoux, and A. George, "Feasibility study for steering a supersonic projectile by a plasma actuator," *AIAA Journal*, vol. 46, no. 6, pp. 1308–1317, 2008.

[102] S. O. Macheret, M. N. Shneider, and R. B. Miles, "Scramjet inlet control by off-body energy addition: a virtual cowl," 2003, paper AIAA 2003-0032.

[103] M. N. Shneider and S. O. Macheret, "Modeling of plasma virtual shape control of ram/scramjet inlet and isolator," *Journal of Propulsion and Power*, vol. 22, no. 2, pp. 447–454, 2006.

[104] B. McAndrew, J. Kline, J. Fox, D. Sullivan, and R. Miles, "Supersonic vehicle control by microwave driven plasma discharges," 2002, paper AIAA 2002-0354.

[105] G. I. Mishin, “Experimental investigation of the flight of a sphere in weakly ionized air,” 1997, paper AIAA 1997-2298.

[106] Y. C. Ganiev, V. P. Gordeev, A. V. Krasilnikov, V. I. Lagutin, V. N. Otmennikov, and A. V. Panasenko, “Aerodynamic drag reduction by plasma and hot-gas injection,” *Journal of Thermophysics and Heat Transfer*, vol. 14, no. 1, pp. 10–17, 2000.

[107] V. M. Batenin, V. A. Bityurin, A. N. Bocharov, V. G. Brovkin, A. I. Klimov, Y. F. Kolesnichenko, and S. B. Leonov, “EM advanced flow/flight control,” 2001, paper AIAA 2001-0489.

[108] C. F. Suchomel, D. V. Wie, and D. Risha, “Perspectives on cataloging plasma technologies applied to aeronautical sciences,” 2003, paper AIAA 2003-3852.

[109] V. M. Fomin, A. A. Maslov, N. D. Malmuth, V. P. Fomichev, A. P. Shashkin, T. A. Korotaeva, A. N. Shiplyuk, and G. A. Pozdnyakov, “Influence of a counterflow plasma jet on supersonic blunt-body pressures,” *AIAA Journal*, vol. 40, no. 6, pp. 1170–1177, 2002.

[110] U. Kogelschatz, B. Eliasson, and W. Egli, “From ozone generators to flat television screens: History and future potential of dielectric-barrier discharges,” *Pure and Applied Chemistry*, vol. 71, no. 10, pp. 1819–1828, 1999.

[111] S. Okazaki, M. Kogoma, M. Uehara, and Y. Kimura, “Appearance of stable glow discharge in air, argon, oxygen, and nitrogen at atmospheric pressure using a 50 Hz source,” *Journal of Physics D: Applied Physics*, vol. 26, no. 5, pp. 889–892, 1993.

[112] J. R. Roth, D. M. Sherman, and S. P. Wilkinson, “Boundary layer flow control with a one atmosphere uniform glow discharge surface plasma,” 1998, paper AIAA 1998-0328.

[113] F. Massines, A. Rabehi, P. Decomps, R. B. Gadri, P. Ségur, and C. Mayoux, “Experimental and theoretical study of a glow discharge at atmospheric pressure controlled by dielectric barrier,” *Journal of Applied Physics*, vol. 83, no. 6, pp. 2950–2957, 1998.

[114] E. Moreau, “Airflow control by non-thermal plasma actuators,” *Journal of Physics D: Applied Physics*, vol. 40, no. 3, pp. 605–636, 2007.

[115] T. C. Corke, M. L. Post, and D. M. Orlov, “SDBD plasma enhanced aerodynamics: Concepts, optimization and applications,” *Progress in Aerospace Sciences*, vol. 43, no. 7, pp. 193–217, 2007.

[116] B. Jayaraman and W. Shyy, “Modeling of dielectric barrier discharge-induced fluid dynamics and heat transfer,” *Progress in Aerospace Sciences*, vol. 44, no. 3, pp. 139–191, 2008.

[117] J. R. Roth and X. Dai, “Optimization of the aerodynamic plasma actuator as an electrohydrodynamic (EHD) electrical device,” 2006, paper AIAA 2006-1203.

[118] A. Santhanakrishnan and J. D. Jacob, “Flow control with plasma synthetic jet actuators,” *Journal of Physics D: Applied Physics*, vol. 40, no. 3, pp. 637–651, 2007.

[119] N. Benard, J. P. Bonnet, G. Touchard, and E. Moreau, “Flow control by dielectric barrier discharge actuators: Jet mixing enhancement,” *AIAA Journal*, vol. 46, no. 9, pp. 2293–2305, 2008.

[120] D. F. Opaits, D. V. Roupassov, S. M. Starikovskaia, A. Y. Starikovskii, I. N. Zavialov, and S. G. Saddoughi, “Plasma control of boundary layer using low-temperature non-equilibrium plasma of gas discharge,” 2005, paper AIAA 2005-1180.

[121] D. V. Roupassov, I. N. Zavyalov, and A. Y. Starikovskii, “Boundary layer separation plasma control using low-temperature non-equilibrium plasma of gas discharge,” 2006, paper AIAA 2006-0373.

[122] A. A. Sidorenko, A. D. Budovsky, A. V. Pushkarev, and A. A. Maslov, “Flight testing of a DBD plasma separation control system,” 2008, paper AIAA 2008-0373.

[123] T. C. Corke, D. A. Cavalieri, and E. Matlis, “Boundary-layer instability on sharp cone at Mach 3.5 with controlled input,” *AIAA Journal*, vol. 40, no. 5, pp. 1015–1018, 2001.

[124] C. L. Enloe, T. E. McLaughlin, R. D. VanDyken, K. D. Kachner, E. J. Jumper, and T. C. Corke, “Mechanisms and responses of a single dielectric barrier plasma,” 2003, paper AIAA 2003-1021.

[125] J. Huang, T. C. Corke, and F. O. Thomas, “Plasma actuators for separation control of low-pressure turbine blades,” *AIAA Journal*, vol. 44, no. 1, pp. 51–57, 2006.

[126] ——, “Unsteady plasma actuators for separation control of low-pressure turbine blades,” *AIAA Journal*, vol. 44, no. 7, pp. 1477–1487, 2006.

[127] M. Samimy, J. H. Kim, J. Kastner, I. Adamovich, and Y. Utkin, “Active control of high-speed and high-Reynolds-number jets using plasma actuators,” *Journal of Fluid Mechanics*, vol. 578, pp. 305–330, 2007.

[128] M. P. Patel, T. T. Ng, S. Vasudevan, T. C. Corke, and C. He, “Plasma actuators for hingeless aerodynamic control of an unmanned air vehicle,” *Journal of Aircraft*, vol. 44, no. 4, pp. 1264–1274, 2007.

[129] D. Greenblatt, B. Goksel, I. Rechenberg, C. Y. Schule, D. Romann, and C. O. Paschereit, “Dielectric barrier discharge flow control at very low flight Reynolds numbers,” *AIAA Journal*, vol. 46, no. 6, pp. 1528–1541, 2008.

[130] T. Abe, Y. Takizawa, S. Sato, and N. Kimura, “Experimental study for momentum transfer in a dielectric barrier discharge plasma actuator,” *AIAA Journal*, vol. 46, no. 9, pp. 2248–2256, 2008.

[131] S. M. Starikovskaia, “Plasma assisted ignition and combustion,” *Journal of Physics D: Applied Physics*, vol. 39, no. 16, pp. R265–R299, 2006.

[132] R. Narasimha and S. N. Prasad, “Leading edge shape for flat plate boundary layer studies,” *Experiments in Fluids*, vol. 17, no. 5, pp. 358–360, 1994.

[133] D. A. Compton and J. K. Eaton, “Near-wall measurements in a three-dimensional turbulent boundary layer,” *Journal of Fluid Mechanics*, vol. 350, pp. 189–208, 1997.

[134] M. Kruse and S. Wagner, “Visualization and laser doppler measurements of the development of lambda vortices in laminar-turbulent transition,” *Measurement Science and Technology*, vol. 9, no. 5, pp. 659–669, 1998.

[135] H. Backer and J. W. Bradley, “Observations of the long-term plasma evolution in a pulsed DC magnetron discharge,” *Plasma Sources Science and Technology*, vol. 14, no. 3, pp. 419–431, 2005.

[136] W. G. Vincenti and C. H. Kruger, *Introduction to physical gas dynamics.* New York, NY: Krieger, 1965.

[137] H. Koinuma, H. Ohkubo, T. Hashimoto, K. Inomata, T. Shiraishi, A. Miyanaga, and S. Hayashi, “Development and application of a microbeam plasma generator,” *Applied Physics Letters*, vol. 60, no. 7, pp. 816–817, 1992.

[138] A. Schutze, J. Y. Jeong, S. E. Babayan, J. Park, G. S. Selwyn, and R. F. Hicks, “The atmospheric-pressure plasma jet: a review and comparison to other plasma sources,” *IEEE Transactions on Plasma Science*, vol. 26, no. 6, pp. 1685–1694, 1998.

[139] P. K. Panicker, U. S. Satyanand, F. K. Lu, G. Emanuel, and B. T. Svihel, "Development of a corona discharge apparatus for supersonic flow," 2003, paper AIAA 2003-6925.

[140] Y. D. Afanasyev and V. N. Korabel, "Starting vortex dipoles in a viscous fluid: asymptotic theory, numerical simulations, and laboratory experiments," *Physics of Fluids*, vol. 16, no. 11, pp. 3850–3858, 2004.

[141] J. B. Barlow, W. H. Rae, and A. Pope, *Low-speed wind tunnel testing*, 3rd ed. New York, NY: John Wiley and Sons, 1999.

[142] F. M. White, *Viscous fluid flow.* New York, NY: McGraw-Hill, 1974.

[143] F. Clauser, "Turbulent boundary layers in adverse pressure gradients," *Journal of the Aeronautical Sciences*, vol. 21, no. 1, pp. 91–108, 1954.

BIOGRAPHICAL STATEMENT

Eric M. Braun was born in a suburb of Cleveland, Ohio, in 1983. He received his B.S.E. degree in Aerospace Engineering from Case Western Reserve University in Cleveland in 2006. Mr. Braun chose a graduate school by first drawing a 1000 mile radius circle around the city of Cleveland and excluding all schools within it. With the entire eastern seaboard eliminated and unhappy about the prospects of driving all the way to California, he decided to relocate to Texas. The University of Texas at Arlington was chosen because of the excellent faculty members and research in the field of gas dynamics.